Tracing the evolution and genomic dynamics of mating-type loci in *Cryptococcus* pathogens and closely related species

Marco A. Coelho[1,§,*], Márcia David-Palma[1,§], Seonju Marincowitz[2], Janneke Aylward[2,3], Nam Q. Pham[2], Andrey M. Yurkov[4], Brenda D. Wingfield[2], Michael J. Wingfield[2], Sheng Sun[1], and Joseph Heitman[1*]

[1]Department of Molecular Genetics and Microbiology, Duke University Medical Center, Durham, North Carolina, USA

[2]Department of Biochemistry, Genetics and Microbiology, Forestry and Agricultural Biotechnology Institute (FABI), University of Pretoria, Pretoria, South Africa

[3]Department of Conservation Ecology and Entomology, Stellenbosch University, Stellenbosch, South Africa

[4]Leibniz Institute DSMZ-German Collection of Microorganisms and Cell Cultures, Braunschweig, Germany

[§]These authors contributed equally as first authors.

*Corresponding authors

Emails: marco.dias.coelho@duke.edu and heitm001@duke.edu

Running title: Mating-type loci evolution in *Cryptococcus* and *Kwoniella*

Keywords: Mating-type locus, *MAT* genes, chromosomal rearrangements, human fungal pathogens.

Abstract

Sexual reproduction in basidiomycete fungi is governed by *MAT* loci (*P/R* and *HD*), which exhibit remarkable evolutionary plasticity, characterized by expansions, rearrangements, and gene losses often associated with mating system transitions. The sister genera *Cryptococcus* and *Kwoniella* provide a powerful framework for studying *MAT* loci evolution owing to their diverse reproductive strategies and distinct architectures, spanning bipolar and tetrapolar systems with either linked or unlinked *MAT* loci. Building on recent comparative genomic analyses, we generated additional chromosome-level assemblies, uncovering distinct trajectories shaping *MAT* loci organization. Contrasting with the small-scale expansions and gene acquisitions observed in *Kwoniella*, our analyses revealed independent expansions of the *P/R* locus in tetrapolar *Cryptococcus*, possibly driven by pheromone gene duplications. Notably, these expansions coincided with a pronounced GC-content reduction best explained by reduced GC-biased gene conversion following recombination suppression, rather than relaxed codon usage selection. Diverse modes of *MAT* locus linkage were also identified, including three previously unrecognized transitions: one resulting in a pseudobipolar arrangement and two leading to bipolarity. All three transitions involved translocations. In the pseudobipolar configuration, the *P/R* and *HD* loci remained on the same chromosome but genetically unlinked, whereas the bipolar transitions additionally featured rearrangements that fused the two loci into a nonrecombining region. Mating assays confirmed a sexual cycle in *C. decagattii*, demonstrating its ability to undergo mating and sporulation. Progeny analysis in *K. mangrovensis* revealed substantial ploidy variation and aneuploidy, likely stemming from haploid-diploid mating, yet evidence of recombination and loss of heterozygosity indicates that meiotic exchange occurs despite irregular chromosome segregation. Our findings underscore the importance of continued diversity sampling and provide further evidence for convergent evolution of fused *MAT* loci in basidiomycetes, offering new insights into the genetic and chromosomal changes driving reproductive transitions.

Introduction

Sexual reproduction is a cornerstone of eukaryotic biology, generating genetic variation through recombination and allele segregation, which fuels adaptation in changing environments [1-3]. The Fungal Kingdom is amongst the most ecologically diverse, with species thriving in nearly every environment, acting as decomposers, symbionts, commensals, as well as pathogens of plants, animals, and other fungi [4-6]. This versatility is mirrored in a wide range of dispersal stages and reproductive strategies, from heterothallism, requiring genetically distinct individuals of opposite mating types, to homothallism, which allows self-fertilization by a single individual as well as outcrossing [7, 8].

In heterothallic basidiomycete fungi, sexual compatibility is typically governed by two mating-type (*MAT*) loci. The pheromone/receptor (*P/R*) locus encodes at least one mating pheromone and one G-protein-coupled pheromone receptor, enabling mate recognition and fusion. The *HD* locus encodes two homeodomain transcription factors (HD1/Sxi1 and HD2/Sxi2) that heterodimerize post-mating to control dikaryotic growth and sexual development [9]. Successful mating occurs only between mating partners with different, compatible alleles of both *MAT* loci.

Most basidiomycetes exhibit a tetrapolar breeding system, with *P/R* and *HD* unlinked on separate chromosomes, allowing each meiotic event to generate up to four distinct mating types [10]. Some lineages, however, have evolved a bipolar system, in which sexual compatibility is controlled by a single *MAT* locus. This transition can occur either through loss of function of one locus in mating-type determination, as in *Coprinellus disseminatus* [11] and other mushroom-forming *Agaricomycetes* [12-14], or via physical linkage and subsequent fusion (i.e., genetic linkage) of the *P/R* and *HD* loci. In the latter case, translocations or chromosome fusions bring the two loci together, followed by additional rearrangements that suppress recombination, resulting in a single, fused, nonrecombining *MAT* region that is often expanded, highly rearranged, and

biallelic [15-18]. Some basidiomycetes also exhibit a pseudobipolar configuration, where the two *MAT* loci lie on the same chromosome but remain genetically unlinked because they are sufficiently distant to allow recombination, as seen in skin-commensal/pathogenic *Malassezia* species [19, 20]. Beyond heterothallism, several basidiomycetes reproduce without a partner. This strategy, broadly termed homothallism, encompasses diverse genetic mechanisms, including primary homothallism, where a single individual carries all *MAT* alleles necessary for sexual development [21-24], and unisexual reproduction involving cells of the same mating type [25].

Evidence suggests that tetrapolarity is ancestral in basidiomycetes, with bipolarity via *P/R-HD* fusion arising independently multiple times [15, 16, 18, 26, 27]. This bipolar configuration, often observed in fungal species associated with plants or animals as commensals or pathogens, increases sibling compatibility from 25% (tetrapolar) to 50% (bipolar), thereby facilitating inbreeding [9, 28, 29]. This may benefit species colonizing hosts, where spore dispersal and access to unrelated mating partners may be more limited. Bipolar species with fused *MAT* loci are found across the three basidiomycete subphyla, including smut fungi of grasses [15, 30, 31], anther-smut *Microbotryum* infecting *Caryophyllaceae* [17, 27, 32, 33], and two *Tremellomycetes* lineages: *Trichosporonales* [18] and the human-pathogenic *Cryptococcus* species [16, 34, 35].

An important aspect of fused *MAT* loci is the inclusion of genes beyond the core *HD* and *P/R* determinants, some encoding regulators of post-mating development that influence morphogenesis (e.g., *STE20*, required for polarity maintenance in dikaryotic hyphae [36]) and dispersal (e.g., *SPO14*, likely involved in spore production) [37]. Additionally, recombination suppression often extends beyond the core mating-type genes, encompassing larger regions of the *MAT*-containing chromosome [38]. While this may preserve beneficial allele combinations, it also contributes to genomic degeneration, including gene loss, accumulation of transposable elements (TEs), and extensive rearrangements. These dynamics parallel sex chromosome

evolution in other eukaryotes, highlighting potential convergent evolution in sexual reproduction regulation [34, 39].

The genus *Cryptococcus* includes both human-pathogenic species of critical importance and nonpathogenic saprobes. The pathogenic clade comprises *Cryptococcus neoformans*, *C. deneoformans*, and six species in the *C. gattii* complex [40, 41], with *C. neoformans* ranking first on the World Health Organization's list of critical fungal pathogens [42, 43]. Nonpathogens include *C. wingfieldii*, *C. amylolentus*, *C. floricola*, *C. depauperatus*, and *C. luteus* [23, 44-47], along with newly identified lineages [48, 49], many associated with insects, particularly bark beetles [50]. The sister genus, *Kwoniella*, consists of saprophytes found in diverse environments, including soil, seawater, plant material, and insect frass [46, 48, 49, 51, 52].

Sexual reproduction is well characterized in *Cryptococcus* and has been linked to pathogenicity in medically relevant species [53-55]. A hallmark of the sexual cycle is the yeast-to-hypha transition, which occurs after mating between yeast cells of opposite mating types (**a** and α) or during unisexual reproduction [25]. This morphological switch aids nutrient foraging [56, 57] and enhances survival against environmental stressors and microbial predators, thought to be major selective forces in *Cryptococcus* evolution [53, 58-62]. Hyphae eventually differentiate into basidia, where diploid nuclei undergo meiosis to produce basidiospores that are smaller than yeast cells and more resilient to environmental stresses. These spores facilitate alveolar deposition upon inhalation and subsequent dissemination within the host [63-65]. In contrast, sexual reproduction in *Kwoniella* has been documented only in *K. mangrovensis* and *K. heveanensis* [52, 66, 67]. These species do not form aerial basidia with spore chains, likely making them less efficient at environmental dispersal than *Cryptococcus*.

Recent surveys have uncovered novel *Cryptococcus* and *Kwoniella* species [41, 48, 49, 68, 69], often from single isolates, limiting mating tests and hindering characterization of reproductive strategies and compatibility systems. In such cases, high-quality genome assemblies

offer a powerful alternative, enabling comparative analyses of *MAT* loci to elucidate reproductive systems. While our recent work generated chromosome-level genome assemblies for several *Cryptococcus* and *Kwoniella* species, providing insights into their genomic architecture and evolution [49], this was restricted to single strains per species, precluding in-depth analyses of *MAT* locus variation.

Here, we examine a broader diversity of species and, where possible, strains of opposite mating types within the same species, enabling systematic characterization of *MAT* loci structure, chromosomal organization, and key evolutionary transitions. Our findings reveal tetrapolarity as the ancestral state of both *Cryptococcus* and *Kwoniella*, with *P/R-HD* loci fusion (i.e., genetic linkage) evolving independently three times: (i) in the common ancestor of pathogenic *Cryptococcus* species, (ii) in a recently identified nonpathogenic *Cryptococcus* species, and (iii) in one *Kwoniella* species. We further show that the *P/R* locus itself is highly dynamic, sharing only a core set of four genes across both genera, and has undergone lineage-specific expansions, particularly in *Cryptococcus*, where increased pheromone gene copy number appears to have driven further rearrangements. Experimental crosses also confirmed a previously unobserved sexual cycle in *C. decagattii* and provided the first direct evidence of recombination in *K. mangrovensis*, revealing meiotic exchange in progeny and non-haploid offspring with potential for self-fertility. Collectively, our findings support that fused *MAT* loci have evolved multiple times independently in basidiomycetes, reinforcing the role of convergent evolution in shaping reproductive strategies and ecological adaptation.

Results

Chromosome-level assemblies and updated phylogenetic relationships of *Cryptococcus* and *Kwoniella*

To enable detailed analyses of *MAT* locus structure and evolution, we expanded our previous genomic dataset (29 assemblies; [49]) by incorporating genome sequences for 12 additional *Cryptococcus* and 7 *Kwoniella* strains, including opposite mating types where available. Among the *Cryptococcus* strains, four represent three currently undescribed species (*Cryptococcus* sp. 3, sp. 4, and sp. 5; **Fig 1A**), while the remaining eight are opposite mating types of pathogenic *Cryptococcus* species previously sequenced [49]. For *Kwoniella*, three strains belong to the recently described species *K. ovata*, *K. endophytica*, and *K. fici* [48, 70, 71], while the remaining four strains are different mating types of *K. mangrovensis*, *K. europaea*, *K. botswanensis*, and *K. heveanensis*, as previously determined through PCR and mating tests [52, 66, 67]. All but three genomes were assembled from long-read sequencing data (PacBio or Oxford Nanopore) and polished with short-read (Illumina) data, yielding chromosome-level genome assemblies. The exceptions, *K. europaea* PYCC6162, *K. botswanensis* CBS12717, and *K. heveanensis* BCC8398 were sequenced solely with Illumina, resulting in more fragmented assemblies. Analyzed strains were inferred to be haploid based on genome sizes consistent with those previously documented for haploid strains [49]. In total, the expanded dataset comprises 27 *Cryptococcus* strains (spanning 17 species) and 22 *Kwoniella* strains (spanning 18 species) (**S1 Appendix**).

To establish evolutionary relationships across species and determine the placement of the newly sequenced taxa, we identified 3,086 single-copy orthologous genes shared across *Cryptococcus* and *Kwoniella*, along with three outgroup species (*Tremella mesenterica*, *Saitozyma podzolica*, and *Bullera alba*), and reconstructed phylogenies employing both Maximum Likelihood (ML) and coalescent-based methods. Both approaches produced largely congruent

results, except for the variable placement of *Cryptococcus* clades B and C relative to clade A (**Fig 1A** and **S1 Fig**). This inconsistency, noted in earlier studies [23, 45, 47], remains unresolved with the current dataset. Despite this, phylogenetic placement of the newly identified *Cryptococcus* and *Kwoniella* species was resolved. *Cryptococcus* sp. 3, known from a single strain (CMW60451) isolated from a bark beetle (*Lanurgus* sp.) infesting twigs of the endangered conifer *Widdringtonia cedarbergensis* in the Cederberg Mountains of South Africa, was placed as the closest relative of *C. depauperatus*, albeit on a long branch. *Cryptococcus* sp. 4 [72] and *Cryptococcus* sp. 5 clustered with *Cryptococcus* sp. 6 (OR918) [49, 73], together forming a sister clade to all other known *Cryptococcus*. Among *Kwoniella*, *K. ovata* and *K. endophytica* were identified as sister species closely related to *K. dendrophila*, while *K. fici* grouped with *Kwoniella* sp. 4. The new *Cryptococcus* and *Kwoniella* species will be formally described elsewhere.

Sexual reproduction, breeding systems, and *MAT* gene identification and organization across *Cryptococcus* and *Kwoniella*

Sexual cycles have been described for eight *Cryptococcus* species: seven primarily heterothallic (*C. neoformans*, *C. deneoformans*, *C. gattii*, *C. bacillisporus*, *C. deuterogattii*, *C. amylolentus*, *C. floricola*), and one homothallic (*C. depauperatus*) (**Fig 1A**) [23, 47, 74-78]. In *Kwoniella*, sexual reproduction has been confirmed only in *K. mangrovensis* and *K. heveanensis*, both heterothallic [45, 52, 66]. We sought to identify sexual cycles in species where none had been described, restricting tests to cases where opposite mating types were available. Crosses were performed under conditions known to induce mating in *Cryptococcus* [79] and examined for the presence of hyphal growth or other sexual structures (basidia and basidiospores).

In *C. decagattii*, sexual reproduction was confirmed by crossing strains 7685027 (*MAT*α) and CBS11687 (*MAT***a**), which produced sexual structures (**S2A Fig**). In contrast, crosses between *C. tetragattii* IND107 and CBS11718 did not yield sexual structures (**S2B Fig**). For *Cryptococcus*

198 sp. 3, sister to *C. depauperatus*, we observed key differences: while *C. depauperatus* is
199 homothallic and exhibits continuous hyphal growth [23], *Cryptococcus* sp. 3 grew mostly as yeast
200 and did not produce sexual structures alone, suggesting it is unlikely to be homothallic (**S2C Fig**).
201 Within clade D species, we tested *Cryptococcus* sp. 4, where two strains of opposite mating types
202 are available. Although some hyphal growth was observed, it was inconsistent, and no discernible
203 sexual structures formed even after prolonged incubation (**S2D Fig**). These negative results may
204 reflect low mating efficiency under laboratory conditions, and future genetic approaches such as
205 *CRG1* deletion [141, 142] could help uncover latent sexual potential in these lineages. Given the
206 absence of confirmed sexual reproduction in most of the species tested, we resorted to genomic
207 data to examine *MAT* gene content and organization, inferring breeding systems (heterothallic or
208 homothallic) and classifying *MAT* loci configurations as tetrapolar, pseudobipolar, or bipolar, as
209 summarized in **Fig 1B**.

210 Consistent with previous studies [34, 78], we confirmed that all pathogenic clade A species,
211 including *C. decagattii* and *C. tetragattii*, have a bipolar mating configuration supported by genome
212 assemblies from both mating types. In contrast, most of the nonpathogenic *Cryptococcus* and
213 *Kwoniella* species appeared to be heterothallic and tetrapolar, consistent with the proposed
214 ancestral state of basidiomycetes [9, 80, 81]. Three exceptions were identified: *Cryptococcus* sp.
215 3 (clade C), *K. europaea* (clade E), and *K. fici* (clade H) (**Figs 1B** and **1E**). In *Cryptococcus* sp. 3
216 and *K. fici*, BLAST searches revealed that the key *MAT* genes (*HD* and the pheromone receptor
217 *STE3*) are close together on the same chromosome, consistent with bipolarity (**Fig 1E**). In
218 contrast, *K. europaea* exhibited a pseudobipolar configuration, with *HD* and *STE3* on the same
219 chromosome but separated by ~8.95 Mb (**Fig 1E**). These findings prompted detailed
220 characterization of *MAT* loci across species and reconstruction of the chromosomal changes
221 underlying bipolar configurations.

222

Structure and evolution of *MAT* loci in *Cryptococcus* and *Kwoniella*

Identification and general organization of *MAT* loci

The structure and gene composition of *MAT* loci have been described for several *Cryptococcus* species within clades A, B, and C [16, 23, 34, 35, 47, 78, 82], but in *Kwoniella* analyses have been limited to *K. mangrovensis* and *K. heveanensis*, based solely on fosmid libraries from a single mating type, leaving the precise structure of *MAT* loci unresolved [66, 67]. To expand on these analyses, we combined genome-wide synteny comparisons with gene genealogies to delineate *MAT* loci across both genera. The *HD* locus was defined based on the presence of the *HD1* and *HD2* genes, while the *P/R* locus boundaries were delineated by identifying regions of disrupted synteny between mating types (see Material and Methods).

In tetrapolar *Cryptococcus* and *Kwoniella* species, the *HD* locus is compact, consisting only of the divergently transcribed *HD1*/*SXI1* and *HD2*/*SXI2* genes (**S3 Fig**). As in other basidiomycetes, mating-type differences are mainly confined to the N-terminal regions of the encoded proteins, and this two-gene structure is strongly conserved. This organization persists in *Kwoniella* species, even though the *HD* locus predominantly resides in subtelomeric regions, inherently more prone to rearrangements (**S3J–S3O Fig**). By contrast, the *P/R* locus spans a larger chromosomal region and is more variable across species and between mating types of the same species (**Figs 2** and **S4**). It is significantly expanded in tetrapolar *Cryptococcus* species, averaging 91.7 kb compared to 29.3 kb in *Kwoniella* (**Figs 2, S4 Fig**, and **S2 Appendix**; $P < 0.0001$, Mann–Whitney U test). Within *Cryptococcus*, sizes range from 84.5 kb in *Cryptococcus* sp. 5 (*P/R a2*) to 101.5 kb in *C. floricola* (*P/R a1*), while in *Kwoniella*, they range from 24.3 kb in *K. newhampshirensis* (*P/R a1*) to 34.4 kb in *K. heveanensis* (*P/R a2*) (**S2 Appendix**).

247 **Evolution of the *P/R* locus in *Kwoniella***

248 Gene content analysis of the *Kwoniella P/R* locus revealed 9 genes shared across all
249 species (**Figs 1C** and **2C-D,** and **S3 Appendix**). These include a single pheromone gene (*MF*α
250 or *MF***a**) containing the canonical CAAX motif at its C-terminus, a pheromone receptor (*STE3*α or
251 *STE3***a**), and two additional genes (*STE20* and *STE12*) with established mating-related roles and
252 found within *MAT* in *Cryptococcus* pathogens [34, 83, 84]. Other conserved genes include *DBP10*
253 and *REI1*, both implicated in ribosome biogenesis in *Saccharomyces cerevisiae* [85, 86]; *ATG7*,
254 an autophagy-related gene [87]; a C2 domain-containing protein (*C2prot*), whose ortholog in *S.*
255 *pombe* (Ync13) coordinates exocytosis, endocytosis, and cell-wall integrity during cytokinesis [88];
256 and *NDC80*, encoding a component of the NDC80 kinetochore complex, essential for
257 chromosome segregation and spindle checkpoint activity [89]. In *K. heveanensis* and other clade
258 G species, two additional genes are present within the *P/R* locus: *BPS3*, encoding a protein of
259 unknown function with BTP/PZ and CAP-Gly domains (also present in the *MAT* locus of
260 *Cryptococcus* pathogens), and *UPB6,* a predicted deubiquitinating enzyme associated with the
261 26S proteasome [90]. Of these, *DBP10*, *REI1*, and *NDC80* are predicted to be essential in *S.*
262 *cerevisiae* and in *C. neoformans*, based on previous studies [85, 86, 89, 91, 92].

263 Across *Kwoniella*, the *P/R a2* allele is generally larger than the *a1* (**Figs 2C-D**, **S4 Fig** and
264 **S2 Appendix**), mainly due to the presence of an additional gene of unknown function. This size
265 difference is also accompanied by truncation of *STE12* within the *a2* allele, with fragments flanking
266 *STE3* on both sides in several species (e.g., *K. mangrovensis* and *K. pini*; **Figs 2C** and **S4**).
267 Fragments of the 3' end of *NDC80* and *BSP3* are likewise found at the right edge of the *P/R a2*
268 allele in certain clade E/F and clade G species, respectively, in addition to apparently intact copies
269 (**Figs 2C** and **S4**). These fragments seem to be remnants of structural rearrangements, potentially
270 associated with duplication tracks at inversion breakpoints. Reconstruction of the likely
271 rearrangements leading to the extant *P/R* configuration in *Kwoniella* suggests three distinct

inversions have shaped the locus in clades E/F: one involving *STE3* and *STE12*, truncating *STE12* in the *a2* allele; a second relocating *DBP10* and *REI1* from the edge of the locus to its center; and a third moving *NDC80* from the edge to the middle of the locus (**S5A Fig**). The first two inversions are conserved in clade G, indicating they are ancestral in *Kwoniella*, while clade G additionally underwent rearrangements repositioning *BSP3-NDC80* and *UBP6* to the center of the locus (**S5B Fig**). This suggests that the *P/R a2* allele has experienced more modifications than the *P/R a1* allele.

Additional complexity is seen in *K. ovata* and *K. endophytica*, where the *P/R* locus contains *STE3***a** and *MF**a*** alleles alongside truncated versions of *STE3*α, with *K. ovata* additionally harboring a truncated *MF*α gene (**Fig 3A**). This mosaic configuration likely arose through intra-*P/R* recombination, as synteny analyses showed that the left side of the locus resembles that of *P/R a2* strains, whereas the right side aligns more closely with the *P/R a1* (**Fig 3A**). Gene genealogies further supported this scenario. While deep trans-specific polymorphism has been well-documented for *STE3*, *STE12*, and *MF* genes, reflecting their ancestral integration into the *P/R* locus across *Cryptococcus* and *Kwoniella* [23, 47, 67, 78], shallower patterns were detected for *NDC80*, *BSP3*, *ATG7*, and *UBP6*. Specifically, *NDC80* exhibited trans-specific polymorphism within clades E/F and G (**Fig 3B**), while *ATG7*, *BSP3*, and *UBP6* displayed this pattern only within clade G (**S5C Fig**). Notably, the *NDC80* allele at the right edge of the *P/R* locus in *K. ovata* and *K. endophytica* clustered more closely with *a1* alleles from other species (**Fig 3B**), and a similar pattern was found in *K. dendrophila*, together pointing to a shared evolutionary history shaped by past intra-*P/R* recombination. This recombination event may have initially produced strains with intercompatible pheromone and receptor pairs, potentially enabling self-filamentous growth. However, subsequent loss of *STE3*α and *MF*α alleles appears to have eliminated self-filamentation. Consistently, solo cultures of *K. ovata* and *K. endophytica* on V8 pH 5 media did not form hyphae, indicating that extant species retain only relics of this ancestral recombination event.

Collectively, these findings unveil a dynamic evolutionary history of the *Kwoniella P/R* locus, shaped by structural rearrangements, recombination, and small-scale lineage-specific expansions.

Evolution and expansion of the *P/R* locus in *Cryptococcus*

Compared to *Kwoniella*, the *P/R* locus in tetrapolar *Cryptococcus* species is larger, averaging 95.4 kb in clade B and 86.9 kb in clade D, a difference not statistically significant (P = 0.063, Mann–Whitney U test; **Figs 2** and **S4**; **S2 Appendix**). It also exhibits more complex rearrangements between mating types, which prevent accurate reconstruction of the evolutionary steps leading to the extant configurations (**Figs 2**, **S4B**, and **S4E**). Gene content analysis revealed striking variation between clades B and D (**Fig 1C**). Both share a core set of 7 genes (*MF* with two to four copies, *STE3*, *STE12*, *BSP3*, *MYO2*, *STE20*, and *RPL39*; **S3 Appendix**), but several genes found within the *P/R* locus in clade B species are instead located in the right flanking region of the locus in clade D species (**Figs 2A-B**, **S4B**, and **S4E**), and in *Kwoniella* these genes are similarly positioned just outside the locus (**Figs 2C-D**, **S4H**, **S4K**, and **S4N**). Despite only 7 genes being shared between clades B and D, the *P/R* locus is similar in size because clade D species harbor up to 15 distinct genes that are absent from the locus in other *Cryptococcus* or *Kwoniella* clades (**Figs 1C**, **2B**, and **S4E**). Extending these comparisons across all tetrapolar species of both genera further revealed that only four genes (*MF*, *STE3*, *STE20*, and *STE12*) are conserved within the *P/R* locus, likely reflecting the ancestral state (**Figs 1C-D**, **S3 Appendix**).

Another notable distinction of the *P/R* locus in *Cryptococcus* is the presence of multiple pheromone genes per mating type [34, 47]. Unlike *Kwoniella*, which retains a single pheromone gene per mating type, all heterothallic *Cryptococcus* species carry multiple copies, up to four per mating type. These genes are often arranged in divergent orientations (**Figs 2A-B**, **S4B**, and **S4E**), a configuration that may act as inverted repeats. Such an arrangement can facilitate inversion-

loop formation during recombination, potentially contributing to structural instability and the expansion of the *P/R* locus boundaries in *Cryptococcus*. Together, these findings support a small ancestral *P/R* locus that expanded independently in descendant lineages by entrapping distinct gene sets through lineage-specific rearrangements.

A final striking observation was the consistently lower GC content of the *P/R* locus compared to genome-wide averages (**Figs 2**, **S4A** and **S4D**; **S4 Appendix**). In *C. amylolentus* CBS6039 (clade B), the *P/R* locus has 51.24% GC versus 53.36% genome-wide (*t*-test: $t = 96.28$, $P < 0.0001$; permutation test: $P = 0.0303$), with Z-scores ranging from –3.04 to –5.00 across clade B strains. This trend is even more pronounced in clade D species, where the difference can approach 10%. For example, in *Cryptococcus* sp. DSM108351, the *P/R* locus has 49.17% GC compared to a genome-wide average of 59.24% (*t*-test: $t = 216.92$, $P < 0.0001$; permutation test: $P = 0.0007$), with Z-scores ranging from –7.56 to –6.71 across clade D strains. To test whether the GC depletion primarily reflects a neutral consequence of reduced GC-biased gene conversion (gBGC) [93, 94] in a recombination-suppressed region or also involves relaxed selection on codon usage, we performed four complementary analyses (see **S1 Text** for details). All pointed to reduced gBGC as the main driver: (i) non-coding GC was significantly lower inside *P/R* than in matched same-chromosome windows, especially in clade D; (ii) coding sequences exhibited a marked shift toward AT-ending codons; (iii) codon-bias indices showed that *P/R* codon usage closely matched expectations based on nucleotide composition, unlike background genes; and (iv) codon adaptation index (CAI) differences were not significant after controlling for GC3 and gene length.

Independent origins and evolutionary outcomes of *MAT* locus fusion

Post-fusion structural dynamics of *MAT* in *Cryptococcus* pathogens

The fusion of the *P/R* and *HD* loci into a single nonrecombining *MAT* locus is well established in clade A, which encompasses all human-pathogenic *Cryptococcus* species. We extended *MAT* locus analysis to all recognized species in this clade (**Figs 1**, **4**, **S6**, and **S7**; **S1 Appendix**). For *C. deneoformans*, our dataset included congenic strains JEC21α and JEC20**a**, their progenitor strains NIH12α and NIH433**a**, and an additional *MAT***a** strain (NIH430) (**S6 Fig** and **S1 Appendix**). For *C. neoformans*, we examined multiple strains of both mating types across the four main lineages (VNI, VNII, VNBI, and VNBII), including eight newly sequenced genomes assembled telomere-to-telomere (T2T) (**Fig 4A** and **S1 Appendix**).

Synteny comparisons revealed that the *MAT***a** allele is generally longer than the *MAT*α allele in both *C. neoformans* ($P < 0.0001$, Mann–Whitney U test) and the *C. gattii* species complex ($P = 0.04142$, Mann–Whitney U test; **Fig 4C and S2 Appendix**), with a similar trend in *C. deneoformans*, although limited sampling precluded statistical support. The *MAT***a** allele also exhibits greater structural diversity than *MAT*α, as seen in the *C. gattii* complex (**S7A Fig**) and in *C. neoformans*, where frequent inversions were detected even among *MAT***a** strains of the same VN lineage (e.g., VNI strains Bt130 vs. IUM96-2828, or strain Bt206 compared to other VNBII strains; **Fig 4D**). Inversion breakpoints were often associated with pheromone genes, consistent with the hypothesis that multiple pheromone copies may act as mediators of structural changes. In contrast, *MAT*α is structurally more conserved with only limited inversions involving the pheromone-gene pairs flanking the *PRT1* and *ZNF1* genes (**Figs 4D** and **S7**). Comparison of the entire *MAT* chromosome across *C. neoformans* strains further showed that most of the intraspecific structural variation is confined to the *MAT* locus, with variation outside *MAT* largely restricted to the inherently dynamic centromeric and telomeric regions (**Fig 4B**).

As part of this analysis, we also detected significant structural divergence between the *MAT***a** alleles of *C. neoformans* VNBI (Ftc555-1 and Bt63) and VNI strains (**Fig 4D**). The VNI lineage has been hypothesized to have diverged initially with only the *MAT*α allele, possibly due to a bottleneck associated with a small founding population, and later acquired the *MAT***a** allele via introgression from a VNBI *MAT***a** donor [95]. To date, only five VNI *MAT***a** strains have been identified [95-100], three of which are now represented by high-quality genome assemblies (125.91 and Bt130, sequenced in this study, and IUM96-2828, sequenced previously [101] and annotated here; **Fig 4D**). This structural divergence did not contradict the introgression model but raised questions about how such differences could be reconciled with an introgressed origin.

To revisit this question with improved data, we reanalyzed SNP data leveraging newly generated reference genomes. Genome-wide SNP analysis, with VNBI *MAT***a** strain Ftc555-1 as the reference, revealed markedly lower SNP densities within the *MAT***a** locus in VNI strains compared to VNBII strains (**Figs 5A** and **5B**). Conversely, across the rest of the genome, VNI *MAT***a** strains diverged more strongly from the VNBI reference, while VNBII strains showed lower SNP densities (**Fig 5A** and **5B**). Notably, the typically high SNP density between VNI and VNBI strains was restored immediately downstream of *MAT* and ~5 genes upstream, consistent with recombination hotspots flanking the locus [102] and previously mapped introgression boundaries [95]. Phylogenetic analyses reinforced these patterns: VNBI strains clustered more closely with VNBII strains in trees inferred from genome-wide and chr. 5-specific SNPs (**Figs 5C** and **5D**), whereas *MAT*-specific SNP trees placed VNI and VNBI *MAT***a** strains together, consistent with a more recent shared ancestry for the *MAT***a** allele (**Fig 5E**). Together, these findings refine the VNBI-to-VNI introgression model (**Fig 5F**) and indicate that lineage-specific rearrangements following introgression account for the structural differences observed.

In addition to introgression, other forces also shaped *MAT* architecture in *C. neoformans*. Species-specific gene losses (e.g., *NCP1* and *NCP2*, which are absent in most species) and TE

395 insertions contributed further to allele differentiation (**S7 Fig**). TE activity appears especially
396 important, as the *C. deneoformans MAT* locus contains over five times more TEs than genome
397 averages outside centromeres [16, 34, 103]. In line with this, we identified novel insertions of two
398 distinct KDZ transposons, recently characterized in *C. neoformans* as large mobile elements (~11
399 kb) with terminal inverted repeats (TIRs) and target site duplications (TSDs) [104]. *KDZx* was
400 present in strains 125.91, C45, PMHc1023, and T4, while *KDZ1* was found in strain Ze90-1 (**Fig**
401 **4D)**. Altogether, these findings underscore the dynamic evolution of the *MAT* locus in
402 *Cryptococcus* pathogens, shaped by an interplay of structural rearrangements, gene loss, TE
403 activity, and introgression.

404

405 **Independent fusion of *P/R* and *HD* loci in *Cryptococcus* sp. 3**

406 Our initial screening of *MAT* gene content revealed that the *P/R*- and *HD*-associated genes
407 are adjacent on the same chromosome in *Cryptococcus* sp. 3, indicating a fusion of these two
408 regions (**Fig 1E**). While only a single strain (CMW60451) is available, limiting precise delineation
409 of *MAT* boundaries, the minimum estimated size is ~90 kb based on the distance between the two
410 most distal pheromone genes (**Fig 6C**). If boundaries are extended to include additional genes
411 that are part of the *MAT* locus in pathogenic *Cryptococcus*, the locus could span ~120 kb, from
412 *RPL22* on the left to *STE12* on the right (**Fig 6C**). Under this broader definition, 15 genes are
413 shared between *Cryptococcus* sp. 3 and clade A species (**Figs 1C** and **6C,** and **S3 Appendix**),
414 including four *MF*α pheromone gene copies and three genes typically associated with the *HD*
415 locus (*RPL22*, *CAP1*, and *SPO14*). Additionally, two regions within the *MAT* locus contain TEs:
416 one with a complete KDZ-like transposon and another with only remnants of this element (**Fig**
417 **6C**).

418 Further analysis uncovered an unusual combination of *MAT* alleles. Unlike the bipolar
419 *Cryptococcus* pathogens, where *MAT*α strains carry *HD1* (*SXI1*) linked to *STE3*α and *MAT***a**

strains have *HD2* (*SXI2*) linked to *STE3***a**, *Cryptococcus* sp. 3 retains only *SXI2* linked to *STE3*α. Although this distinct configuration suggested an independent fusion event at the origin of the *MAT* locus in *Cryptococcus* sp. 3, the unresolved phylogenetic placement of clade C relative to clade A left open the possibility that the two clades share a more recent common ancestor. In this scenario, the fusion of the *P/R* and *HD* loci could have occurred in their shared ancestor rather than independently in both lineages.

To test this hypothesis, we analyzed the phylogenetic clustering patterns of genes within the predicted *MAT* region shared with pathogenic *Cryptococcus*. Genes ancestrally present in the *P/R* locus, such as *STE3, STE12,* and *MYO2*, were excluded from the analysis because they exhibit deep trans-specific polymorphism predating the divergence of *Cryptococcus* species [23, 47, 67, 78], making them uninformative. Instead, we focused on four genes (*BSP3, PRT1, SPO14,* and *CAP1*), which are part of *MAT* in pathogenic species and display mating-type-specific clustering within them [34]. The analysis revealed that *Cryptococcus* sp. 3 sequences do not group with either the **a** or α allele-specific clusters from pathogenic species; rather, they are distinct and fall outside these clusters, which is more consistent with an independent fusion event than one inherited from a shared ancestor (**S8 Fig**).

Having established from gene phylogenies that the *MAT* fusion in *Cryptococcus* sp. 3 likely arose independently, we next examined chromosome-scale structural changes underlying the *P/R-HD* linkage by reconstructing synteny blocks with SynChro [105]. *K. shandongensis* was selected as reference because (i) it is tetrapolar, with *P/R* and *HD* loci on separate chromosomes representing the ancestral state (**Figs 1**, **S3N**, and **S4N**); (ii) *Kwoniella* species show significantly fewer interchromosomal rearrangements than *Cryptococcus*, likely due to their simpler, smaller centromeres and lower TE density, as both high TE content and large, complex centromeres promote genomic rearrangements in *Cryptococcus* [49, 106-108]; and (iii) it retains a 14-

chromosome karyotype, which is the predicted ancestral state for both genera [49] (**Figs 6** and **S9A**).

The nuclear genome of *Cryptococcus* sp. 3 comprises 13 chromosomes (**S1 Appendix**), representing a reduction from the ancestral 14-chromosome karyotype. While we hypothesized that this reduction could explain the *P/R-HD* fusion, examination of the lost centromere showed it did not involve the *MAT*-containing chromosome (detailed in **S2 Text** and **S9B Fig**). Thus, physical linkage of the *P/R* and *HD* loci in *Cryptococcus* sp. 3 arose independently of the karyotypic reduction. We therefore compared the *MAT*-containing chromosome of *Cryptococcus* sp. 3 to the *P/R*- and *HD*-bearing chromosomes of *K. shandongensis*. Synteny analysis revealed significant alignment between chr. 11 of *Cryptococcus* sp. 3 and large regions of *K. shandongensis* chrs. 12 and 5, which carry *P/R* and *HD*, respectively (**Fig 7A**). Additionally, a small segment from the *P/R* chromosome is embedded towards the left end of chr. 11 within a region otherwise derived from the *HD* chromosome. These patterns suggest that the physical linkage likely began with a translocation that brought the two loci onto the same chromosome, initially far apart, followed by an inversion relocating the *HD* locus closer to the *P/R* locus, resulting in their fusion (events 1-3 in **Fig 7A**). Notably, the centromere-flanking regions of chr. 11 in *Cryptococcus* sp. 3 show considerable synteny to the *CEN12*-flanking region in the *K. shandongensis P/R* chromosome, indicating a shared evolutionary origin and suggesting that the translocation did not involve centromeric recombination but occurred elsewhere (**Fig 7A**).

Revisiting the model of *P/R–HD* loci linkage in *Cryptococcus* pathogens

Prompted by these findings, we revisited the proposed model for the physical linkage and subsequent fusion of *P/R* and *HD* loci in *Cryptococcus* pathogens. This model, originally devised from comparisons between *C. amylolentus* (tetrapolar; clade B) and *C. neoformans* (bipolar; clade A), posited that the physical linkage was initiated by a chromosomal translocation mediated by

469 ectopic recombination between repetitive elements within centromeric regions of *P/R*- and *HD*-
470 containing chromosomes. This translocation would place the two *MAT* loci on the same
471 chromosome, initially separated by the centromere. Subsequent rearrangements, such as
472 inversions or transpositions, were hypothesized to bring the two loci closer together, ultimately
473 resulting in their fusion and establishing the contiguous *MAT* locus of *Cryptococcus* pathogens
474 [35, 37].

475 To reassess this hypothesis, we compared multiple *Cryptococcus* species spanning the
476 four clades, focusing on synteny and chromosomal architecture. In *C. neoformans*, the *MAT* locus
477 resides on chr. 5. We found that its centromere (*CEN5*) shares conserved synteny on both flanking
478 regions with *CEN12* of *K. shandongensis*, as well as with *CEN11* of *Cryptococcus* sp. 3 (clade C)
479 and *CEN9* of *Cryptococcus* sp. DSM108351 (clade D) (**Fig 6B**). These conserved synteny
480 patterns indicate a shared evolutionary origin for these centromeres and strongly suggest that
481 they were not directly involved in the translocation linking the *P/R* and *HD* loci in *C. neoformans*.
482 In contrast, the *P/R* chromosome (chr. 10) of *C. amylolentus* (clade B) shows centromere-flanking
483 regions that align with two distinct chromosomes, consistent with intercentromeric recombination
484 and pointing to a derived rather than ancestral centromere structure.

485 Comparisons between *C. neoformans* and *K. shandongensis* further suggest a model in
486 which the physical linkage and subsequent fusion of *P/R* and *HD* in *C. neoformans* arose through
487 a mechanism similar to that proposed for *Cryptococcus* sp. 3, involving a chromosomal
488 translocation outside the centromere followed by an inversion bringing the two loci into closer
489 proximity (**Fig 7B**). In *C. neoformans*, however, the inversion seems to have relocated the *P/R*
490 locus towards the *HD* locus near the left chromosomal end (event 3 in **Fig 7B**). These broader
491 analyses refine the earlier model and suggest that the physical linkage of *P/R* and *HD* loci in
492 *Cryptococcus* species likely arose through alternative mechanisms, independent of centromeric
493 recombination.

494

495 **Tetrapolar to bipolar and pseudobipolar transitions in *Kwoniella***

496 We recently reported that karyotype reduction within *Kwoniella* occurred progressively and
497 independently, often with formation of "giant" chromosomes (up to 18 Mb) through repeated
498 fusions [49]. Although such events could potentially lead to *P/R-HD* physical linkage, only two
499 *Kwoniella* species harbor both loci on the same chromosome (**Fig 1B**). In *K. europaea* (clade E),
500 the *HD* and *P/R* loci are located on the same chromosome but remain far apart (~8.95 Mb) (**Figs**
501 **1E** and **S4G**), representing a pseudobipolar configuration. This arrangement likely arose from a
502 lineage-specific rearrangement, in which the progenitor "giant" chr. 1 of clade E species underwent
503 a translocation with chr. 2 [49]. Given their physical distance, the two *MAT* loci are still expected
504 to recombine.

505 In *K. fici*, by contrast, the *HD* locus lies less than 13 kb from the *P/R* gene cluster, both
506 located near the end of chr. 1 (**Fig 8D**). This "giant" chromosome likely arose independently
507 through fusion events, similar to those documented in *Kwoniella* clades E and G [49]. After
508 divergence from clade I (*K. shandongensis/K. newhampshirensis*), the chromosomes
509 corresponding to chrs. 11 and 12 of *K. shandongensis* fused in the descendant lineage, producing
510 the ancestral *P/R* chromosome, which persists as a single chromosome in most *Kwoniella* species
511 (e.g., chr. 2 in *Kwoniella* sp. 4 DSM27419; **Fig 8A**) [49]. In *K. fici*, however, this ancestral fusion
512 product fragmented further: one block now resides at the terminal region of *K. fici* chr. 1, while
513 another segment lies on chr. 4 (**Fig 8C**). Similarly, most of the *K. shandongensis/Kwoniella* sp. 4
514 *HD* chromosome (chr. 5), aligns with the opposite end of *K. fici* chr. 1, while a small portion is on
515 chr. 4, adjacent to the *P/R*-derived block. Only a few key *HD*-associated genes (*SXI1*, *SXI2*, and
516 *RPL22*) are positioned near the *P/R* locus gene cluster at the right end of chr. 1 (**Fig 8D)**. Notably,
517 this derived bipolar arrangement retains both *HD* genes, unlike bipolar *Cryptococcus* species
518 where opposite mating types carry only one. Overall, these observations indicate that complex

translocations united blocks from ancestral *P/R* and *HD* chromosomes, producing the unique fused configuration in *K. fici*.

Analysis of sexual reproduction in *Kwoniella mangrovensis*

Kwoniella mangrovensis (clade G) can reproduce sexually in the lab [52, 66] and has only three chromosomes. To better understand its reproductive biology, we analyzed recombination, ploidy variation, and the potential for self-fertility in the progeny. The two originally sequenced strains, CBS8507 (*P/R a1*, *HD b1*) and CBS8886 (*P/R a2*, *HD b1*), share identical *HD b1* alleles, making them incompatible for mating (**Fig 9A**). However, Guerreiro et al. [66] reported a third strain, CBS10435, as haploid and compatible with CBS8507. We sequenced CBS10435 with Illumina and confirmed it carries the *P/R a2* allele and a distinct *HD b2* allele, rendering it compatible with CBS8507 (**Fig 9A**).

Crosses between CBS8507 and CBS10435 on CMA and V8 pH 5 media produced basidia with characteristic globose and lageniform morphologies, consistent with prior descriptions (**Fig 9B**) [52]. Progeny were recovered by dissecting eight clusters of cells germinating from basidia along the hyphae (**S5 Appendix**). In total, 51 F1 progeny were obtained from both culture media. To avoid analyzing clonally derived genotypes, we screened for recombination with a PCR-RFLP approach using two markers per chromosome, positioned on either side of the centromere (**S5 Appendix**). Evidence of allele exchange and heterozygosity was detected, and nine F1 progeny with distinct genotypes were selected for whole-genome sequencing. SNPs between the parental strains served as markers to infer inheritance patterns associated with recombination and loss of heterozygosity (LOH), while read coverage analysis and FACS were combined to assess ploidy.

These analyses revealed that most F1 progeny were non-haploid (**Figs 9C-D**, **S10, and S11**). Genotyping and FACS results were largely concordant, though some isolates (e.g., MP11

543 and MP18) showed discrepancies, suggesting variability within cell populations, possibly
544 stemming from intrinsic genomic instability. Accordingly, mapping reads to a combined reference
545 genome (CBS8507 and CBS10435) revealed uneven coverage for certain chromosomes. For
546 example, CBS10435 chr. 2 exhibited low coverage in progeny MP59 (**Fig 9D**). Although CBS8507
547 and CBS10435 were previously reported as haploid [66], our FACS analysis showed that
548 CBS10435 is predominantly diploid with a haploid subpopulation (**Figs 9C** and **S11**). This
549 difference in parental ploidy likely underlies the aneuploidy observed in the progeny, as haploid–
550 diploid matings are prone to chromosome mis-segregation, and the reduced karyotype of *K.*
551 *mangrovensis* (3 chromosomes) may further amplify these effects.

552 Analysis of the *MAT* gene content revealed that some progeny carried fully compatible *P/R*
553 and *HD* alleles (*a1a2b1b2*), potentially enabling self-fertility (**Fig 9C**). To investigate this, we
554 cultured the F1 progeny under mating conditions and compared their phenotypes to a parental
555 cross (**Figs 9E-F**, and **S12**). On CMA and V8 pH 5 media, progeny MP16, MP18, and MP54 with
556 fully compatible *MAT* alleles produced hyphae and basidia similar to the parental cross. Some
557 hyphal growth was also observed in solo culture of strains MP49, MP51 and MP59, exclusively
558 on V8 pH 5, but the filaments were shorter and had no structures resembling basidia (**S12 Fig**).
559 This morphology resembled that of previously described self-filamentous *K. mangrovensis* strains,
560 which form irregular, highly branched hyphae without clamp cells [66]. Taken together, these
561 analyses demonstrate that sexual reproduction in *K. mangrovensis* involves recombination and
562 can generate non-haploid progeny with potential for self-fertility.

563

564

565

566

Discussion

Our comparative genomic analysis revealed new insights into the evolution and structural dynamics of *Cryptococcus* and *Kwoniella MAT* loci, including distinct expansions of the *P/R* locus and additional independent *HD-P/R* fusion events, summarized in **Fig 10** as a roadmap of key transitions.

Multiple independent *P/R* locus expansions in *Cryptococcus* and *Kwoniella*

The archetypal basidiomycete *MAT* loci are thought to consist of a compact *P/R* region with one pheromone receptor and one pheromone gene, and an unlinked *HD* region containing two divergently transcribed homeodomain transcription factors (*HD1* and *HD2*). This configuration is retained in some lineages, such as in *Malassezia* species [20], but in most basidiomycetes the *P/R* locus has undergone expansions and structural changes, while the *HD* locus remains comparatively conserved (except in some rust fungi [109] and in mushroom-forming species with *HD* gene duplications [9, 28]). For example, in *Ustilago maydis*, allele-specific differences in *P/R* locus size arise from two additional genes (*lga2* and *rga2*) in the *a2* allele that direct mitochondrial uniparental DNA inheritance [110, 111]. Similarly, several *Microbotryomycete*s yeasts (*Pucciniomycotina*) harbor expanded *P/R* loci [26, 112, 113], as do tetrapolar *Cryptococcus* species [35, 47, 78]. Recent fully phased, chromosome-scale assemblies in rust fungi also uncovered multiple pheromone genes and *STE3* receptor duplications on single haplotypes [109, 114], though the full structure of the *P/R* locus in these fungi remains incompletely resolved.

Our analyses across tetrapolar *Cryptococcus* and *Kwoniella* support independent, lineage-specific *P/R* locus expansions. The inferred ancestral *P/R* locus likely comprised a conserved four-gene core (*MF, STE3, STE12,* and *STE20*) (**Fig 10**, event 1). In *Kwoniella*, this region has remained relatively compact, with 9 core conserved genes (**Fig 10**, event 2), though lineage-

specific modifications were detected, including mating-type-specific changes (e.g., *STE12* truncation in *a2* alleles) and small-scale expansions through the inclusion of genes likely entrapped by local inversions. We note that these additions more likely reflect neutral consequences of inversions expanding recombination-suppressed regions, rather than adaptive recruitment, consistent with stepwise extension models of sex chromosome and *MAT* locus evolution [39, 115]. In *K. ovata*, *K. endophytica*, and *K. dendrophila*, mosaic *P/R* configurations are better explained by past intra-locus recombination. This may have transiently enabled self-compatibility at the *P/R* locus, but the absence of self-filamentation in extant strains suggests a reversion to heterothallism. A full transition to homothallism would also require compatibility at the *HD* locus, either through mutations enabling pairing between otherwise non-self-compatible *HD1/HD2* alleles or through bypass of *HD* function, as seen in *C. depauperatus* [23].

In contrast to *Kwoniella*, tetrapolar *Cryptococcus* species from clades B and D exhibit pronounced *P/R* locus expansion, but with limited gene-content overlap, indicating that these expansions occurred independently after divergence from a common ancestor (**Fig 10**, event 5). A distinctive feature of the *Cryptococcus P/R* locus is the duplication of pheromone (*MF*) genes, with each mating type typically carrying multiple copies arranged in divergent orientations. Similar patterns occur in *Microbotryomycetes* yeasts [26, 112, 113, 116, 117], and have also been reported in rust fungi [109, 114]. However, in rusts some of the duplicated *MF* genes encode distinct pheromones, possibly reflecting adaptation to different receptor specificities, whereas in *Cryptococcus* and *Microbotryomycetes* the *MF* copies encode identical mature peptides, suggesting functional redundancy rather than diversification.

Experimental evidence in *C. deneoformans* supports a dosage-based model, in which all three *MF*α gene copies are expressed and contribute additively to mating efficiency and filamentation [118]. Triple mutants show severe mating defects, while overexpression enhances differentiation, indicating that pheromone dosage promotes mating responsiveness [118].

616 Although direct functional evidence in other *Cryptococcus* species is lacking, these duplications
617 may similarly enhance partner recognition. This interpretation aligns with sexual selection
618 frameworks in fungi, where pheromone production can act as a costly, honest signal of mating
619 quality (the handicap principle), which posits that only high-quality individuals can afford the cost
620 of producing strong signals and are therefore more likely to be chosen as mates [119, 120]. Studies
621 in model yeasts have shown preferential mating toward high pheromone producers [121, 122], but
622 equivalent tests in basidiomycetes are limited, and the ecological context for such selection in
623 *Cryptococcus* remains unclear. Why pheromone duplications recur in *Cryptococcus* but not in
624 *Kwoniella* remains uncertain. Their absence in *Kwoniella* may reflect lineage-specific constraints
625 or ecological differences—for instance, *Kwoniella* species produce embedded rather than aerial
626 spores, which could reduce the need for long-range mate signaling—although the lack of
627 ecological and population-level data prevents firm conclusions.

628 Notably, *MF* gene duplications can also introduce structural instability by facilitating the
629 formation of inverted repeats, which can promote inversion loops and allele-specific structural
630 rearrangements, potentially expanding recombination-suppressed regions between *P/R* alleles.
631 One way to mitigate this instability is by clustering *MF* gene pairs more closely, thereby restricting
632 the extent of rearrangements. Consistent with this, we observed reduced structural variation in *C.*
633 *neoformans MAT*α strains and in the *C. gattii* species complex, where the two *MF* gene pairs are
634 positioned in close proximity, separated by only two genes. In contrast, *MAT***a** strains exhibit a
635 more dispersed arrangement of *MF* genes, which appears to contribute to greater structural
636 diversity across strains, including the *C. neoformans* VNI-specific rearrangements that arose
637 following introgression of the *MAT***a** allele from the VNBI lineage. Once established, multiple *MF*
638 gene copies may be maintained as templates for intrallelic repair via gene conversion, a non-
639 reciprocal exchange that can occur during meiosis between homologous sequences but also at
640 lower frequencies between sister chromatids, or within duplicated regions on a single chromosome

641 during mitosis [123, 124]. If confirmed, this mechanism would resemble the role of palindromic
642 sequences in preserving gene integrity on the human Y chromosome [125-127]. Introgression
643 events, such as the transfer of *MAT***a** alleles between *C. neoformans* lineages, may further buffer
644 against degeneration by resetting mutational load [128], thereby helping maintain complex *MAT*
645 configurations.

646 Integrated with these structural features, our analyses revealed that the *P/R* locus in clades
647 B and D *Cryptococcus* species has consistently lower GC% relative to genome-wide averages
648 and that this depletion is best explained by reduced GC-biased gene conversion (gBGC) in
649 recombination-suppressed regions rather than by relaxed selection on codon usage. gBGC
650 normally favors the fixation of G/C alleles in regions of frequent recombination, and its reduction
651 allows the AT-biased mutational spectrum to dominate over time, driving local base composition
652 shifts. Similar GC depletion has been reported in the *Trichosporonales MAT* locus [18].
653 Interestingly, this trend is not observed in the *MAT* locus of pathogenic *Cryptococcus*, suggesting
654 that genomic GC background also influences the outcome. In high-GC genomes (e.g., clades B
655 and D), recombination suppression accentuates AT accumulation, whereas in lower-GC genomes
656 (pathogenic *Cryptococcus*; [49]), the absence of a shift suggests they may already be near
657 equilibrium under mutation pressure, masking localized effects.

658

659 Independent transitions to bipolar and pseudobipolar via chromosomal 660 translocations and inversions

661 Beyond the previously documented tetrapolar-to-bipolar transition in pathogenic
662 *Cryptococcus* lineages (clade A), we identified three additional transitions: two leading to bipolarity
663 (*Cryptococcus* sp. 3 and *K. fici*; **Fig 10**, events 6 and 4), and one resulting in a pseudobipolar
664 arrangement (*K. europaea*; **Fig 10**, event 3). Our findings suggest that the transition to bipolarity
665 in *Cryptococcus* sp. 3 likely occurred independently of that in pathogenic species. First, fusion of

666 the *P/R* and *HD* loci in *Cryptococcus* sp. 3 was unrelated to the reduction from 14 to 13
667 chromosomes and instead originated from a translocation followed by an inversion. Second, the
668 *MAT* locus in this species retains only *SXI2* (*HD2*) linked to the *STE3*α, unlike in pathogenic
669 species where *SXI2* is associated with *STE3***a**. Third, phylogenetic analyses revealed that many
670 genes within the *Cryptococcus* sp. 3 *MAT* locus do not group with **a** or α allele-specific clusters
671 from pathogenic species. If the fusion had predated the divergence of these clades, trans-specific
672 polymorphism would be expected, but this pattern was not observed, which is more consistent
673 with an independent origin.

674 However, whether the initial translocation event that brought the *P/R* and *HD* loci onto the
675 same chromosome occurred independently in *Cryptococcus* sp. 3 or in a common ancestor of
676 clades A and C, remains unresolved. This uncertainty stems from three main factors. First,
677 phylogenetic ties among clades A (bipolar), B (tetrapolar), and C (which includes *Cryptococcus*
678 sp. 3 and *C. depauperatus*) are still ambiguous. Second, although our synteny analyses indicate
679 that the translocation breakpoints at the origin of the physical linkage between *MAT* loci differ
680 between *Cryptococcus* sp. 3 and pathogenic species (supporting independent events), these
681 differences might also reflect subsequent rearrangements that accumulated along the two
682 lineages. Third, we have previously reported that *C. depauperatus* also shows a partial merging
683 of *HD*- and *P/R*-derived genes into the same genomic region, but with more extensive gene
684 reshuffling and *HD* gene loss likely associated with a transition to homothallism [23]. Further taxon
685 sampling, combined with phylogenomic approaches tailored to deep divergences, will be required
686 to conclusively resolve these relationships and clarify the broader implications of these transitions.

687 The tetrapolar-to-bipolar transition in *Cryptococcus* pathogens has been hypothesized to
688 result from a chromosomal translocation mediated by ectopic recombination between repetitive
689 elements in the centromeric regions of the *P/R*- and *HD*-containing chromosomes [35]. This model
690 had support from several observations: (i) *Cryptococcus* centromeres are enriched with long-

691 terminal-repeat retrotransposons (LTRs) from the Ty3 and Ty1 superfamilies, which are shared
692 among different centromeres and may facilitate recombination [23, 47, 49, 129, 130]; (ii)
693 chromosomal arm exchanges occurred during the divergence of *Cryptococcus* lineages from their
694 common ancestor [35, 108]; and (iii) the repair of experimentally induced double-strand breaks at
695 centromere-specific transposons in *C. neoformans* frequently results in chromosomal
696 translocations [108]. However, our broader comparisons indicate that the centromere of the *C.*
697 *neoformans MAT* chromosome, along with extended flanking regions, is conserved across most
698 *Cryptococcus* species and in *K. shandongensis*, suggesting an ancestral organization.

699 Indeed, our analyses suggest that translocations outside centromeric regions may have
700 played a more prominent role in repositioning the *P/R* and *HD* loci onto the same chromosome
701 (**Fig 7**). Such non-centromeric translocations also appear to underlie the transition to bipolarity in
702 several *Ustilaginales* species, including *Sporisorium scitamineum* [30] and in the common
703 ancestor of *Ustilago hordei*, *U. nuda*, and *U. bromivora* [31]. Non-centromeric translocation events
704 are also common across other genomic regions when comparing genomes of different
705 *Cryptococcus* species [49] and even among conspecific strains of *C. neoformans* [101, 131].
706 Whether such translocations are influenced by TEs has not yet been systematically analyzed, but
707 studies in *Saccharomyces cerevisiae* have shown they can occur via homologous recombination
708 between retrotransposons on different chromosomes [132]. Given the abundance of TEs in
709 *Cryptococcus* genomes [49], they may likewise have facilitated the chromosomal relocation of
710 *MAT* loci and the subsequent transition to bipolarity. Our findings offer an alternative to models
711 invoking intercentromeric recombination as the primary event initiating the tetrapolar-to-bipolar
712 transition in *Cryptococcus* pathogens.

713 Genetically linked *P/R-HD* loci can also arise from the fusion of entire ancestral *P/R* and
714 *HD* chromosomes, as reported in *Microbotryum violaceum* on *Silene paradoxa* [27]. In *Kwoniella*,
715 repeated and independent chromosome fusions have drastically reduced chromosome numbers,

716 with some extant species retaining only 3 (clade E) or 5 (clades G and H) chromosomes from a
717 14-chromosome ancestral karyotype [49]. Yet, aside from the bipolar arrangement in *K. fici* (clade
718 H) and the pseudobipolar arrangement in *K. europaea* (clade E), no other instances of *P/R-HD*
719 linkage or colocation were detected in *Kwoniella*, and even in these species the transition reflects
720 chromosomal translocations rather than whole-chromosome fusions.

721 In *K. fici*, the transition to fused *MAT* loci did not result in loss of *SXI1* (*HD1*) or *SXI2* (*HD2*),
722 possibly suggesting a relatively recent fusion where insufficient time has passed for one *HD* gene
723 to decay in each mating type, as observed in *Cryptococcus* sp. 3, *Cryptococcus* pathogens [133],
724 and *Trichosporonales* [18]. Other known instances of *HD* gene loss in bipolar species, albeit
725 distinct, include: (i) *Microbotryum violaceum* on *Silene caroliniana*, where *HD1* is absent in *a2*
726 strains, while *a1* retains both *HD* genes [27]; (ii) *Microbotryum superbum*, where loss of *HD*
727 function in mating compatibility may have relaxed constraints on *HD2* maintenance in *a1* strains,
728 leading to its disruption while *a2* strains retain both *HD* genes [117]; and (iii) xerotolerant *Wallemia*
729 species, where *HD1* is retained in *MAT a1*, while the opposite mating type appears to lack any *HD*
730 gene [134]. Because *HD* compatibility is no longer an independent determinant of mating success
731 in bipolar species, maintaining both *HD* genes in each *MAT* allele may become dispensable, with
732 loss potentially reflecting genomic streamlining once *MAT* loci are fused and recombination
733 suppressed. Yet, as in *K. fici*, the retention of both *HD* genes in each allele remains the
734 predominant organization in other bipolar basidiomycetes with fused *MAT* loci, including several
735 *Microbotryum* [27], *Sporisorium* [30], and *Ustilago* species [31, 135, 136], possibly reflecting
736 differences in mating strategies or genomic constraints. For instance, if both *HD* genes have
737 additional roles beyond mating-type determination that do not require heterodimerization, their
738 retention could be selectively maintained, although this possibility remains largely unexplored in
739 basidiomycetes.

740 In contrast to *K. fici*, where the *MAT* loci are fused, *K. europaea* has the two loci ~8.5 Mb
741 apart on the same chromosome. This distance makes tight genetic linkage unlikely, though
742 extended recombination suppression over megabase-long spans has been reported in
743 *Neurospora tetrasperma* and *Microbotryum* [39, 137]. Because crosses in *K. europaea* have not
744 yielded sexual reproduction [66], it remains unclear whether this configuration represents an
745 incipient step toward bipolarity or a neutral byproduct of chromosomal rearrangements. If
746 recombination persists, this system would functionally resemble tetrapolarity, as the two loci would
747 still reassort in most meioses, making *MAT* loci colocation unlikely to meaningfully increase sibling
748 compatibility. In this case, the arrangement may simply reflect a stochastic translocation rather
749 than a selectively maintained feature.

750 Together, these observations reinforce the view that chromosomal rearrangements provide
751 the mechanistic basis for tetrapolar-to-bipolar transitions but do not inherently drive shifts in
752 breeding systems. Instead, whether a lineage remains tetrapolar or transitions to bipolarity likely
753 depends on ecological and evolutionary pressures such as opportunities for outcrossing versus
754 inbreeding, the frequency of sibling or clonal mating after colonization, dispersal limitations, and
755 the long-term stability of chromosomal rearrangements that maintain linkage between the loci.
756 Accordingly, species with linked *MAT* loci are often associated with animals or plants as
757 commensals or pathogens, where linkage facilitates mating among siblings and provides an
758 advantage during host colonization [9, 28, 81, 138, 139]. A similar scenario has been proposed
759 for the *Trichosporonales*, where *MAT* locus fusion may have originated in a host-associated
760 ancestor and persisted in saprobic descendants [18]. Our results, however, show that bipolarity is
761 not restricted to pathogens: *Cryptococcus* sp. 3 (isolated from bark beetles) and *Kwoniella fici*
762 (isolated from fig) harbor fused *MAT* loci with no evidence of pathogenicity to date. This suggests
763 that restricted partner availability—whether in insect-associated microhabitats or free-living clonal
764 populations—may favor *MAT* loci fusion independently of pathogenicity. Once established, bipolar

systems may be difficult to revert, and their stability could in turn facilitate the persistence or emergence of pathogenic lifestyles by ensuring mating success under the constrained conditions typical of infection.

Outlook

Our characterization of *MAT* loci gene content and organization allowed us to infer putative breeding systems (heterothallism vs. homothallism) across species. However, determining how often sexual reproduction and recombination occur in nature, and whether mating involves primarily outcrossing or inbreeding, will require population-level analyses such as linkage disequilibrium decay [140]. Unlike basidiomycete macrofungi, where sexual structures can be directly observed in the field, or smut fungi, where disease symptoms visibly reflect the production of sexual spores, most *Tremellomycetes* are inconspicuous environmental isolates or parasites of lichens and other fungi, complicating the isolation of compatible mating partners. Their cryptic nature has led to many species being described from a single isolate [48], hindering mating assays. Progress will require expanded taxon and population-level sampling [48, 50], particularly for nonpathogenic species, to clarify reproductive strategies, transitions in mating systems, and potentially capture changes in *MAT* locus organization as they occur. Uncovering the hidden diversity of *Cryptococcus* species—particularly in their likely African origin [50]—will also be crucial for linking ecology, speciation, and adaptation with the evolutionary forces shaping *MAT* locus evolution and reproductive transitions, with possible implications for pathogenic emergence.

789 # Materials and methods

790 ## Strains and media

791 Strains were routinely grown on YPD medium (10 g/L yeast extract, 20 g/L Bacto Peptone,
792 20 g/L dextrose, and 20 g/L agar) unless indicated otherwise. *C. neoformans* and *C.*
793 *deneoformans* strains were incubated at 30°C, while other *Cryptococcus* and *Kwoniella* species
794 strains were grown at room temperature (20-23°C). A complete list of strains is provided in **S1**
795 **Appendix**. Strain NCYC1536 was obtained from the National Collection of Yeast Cultures
796 (Norwich, UK), and strain CMW60451 was isolated in October 2022 from a bark beetle (*Lanurgus*
797 sp.) infesting twigs of *Widdringtonia cedarbergensis* in the Cederberg Mountains, South Africa.

798

799 ## Genomic DNA extraction

800 High-molecular weight (HMW) DNA was extracted with a cetyltrimethylammonium bromide
801 (CTAB) extraction as previously described [108], minimizing DNA shearing during sample
802 preparation. DNA quality was evaluated by determining the A260/A280 and A260/A230 ratios on
803 NanoDrop spectrophotometer (Thermo). Integrity and fragment size were analyzed using clamped
804 homogeneous electric field (CHEF) electrophoresis, and gDNA for short-read whole-genome
805 sequencing (Illumina) was extracted with a phenol:chloroform-based protocol, both as previously
806 described [49]. DNA concentration was measured with Qubit dsDNA Assay Kits (Invitrogen) on
807 the Qubit fluorometer.

808

809 ## Genome sequencing

810 Whole-genome sequencing was performed with PacBio, Nanopore, and Illumina
811 technologies. For *K. heveanensis* BCC8398 and *K. mangrovensis* CBS10435, Illumina

812 sequencing at the Broad Institute Genomics Platform utilized “fragment” and “jumping” libraries,
813 prepared and sequenced as previously described [49]. All other Illumina sequencing was
814 conducted at the Duke University Sequencing and Genomic Technologies (DUSGT) Core, with
815 libraries prepared with Kapa HyperPlus kit and sequenced as paired-end 2 x 150 bp reads on
816 various Illumina platforms. For PacBio sequencing, 15–20 kb insert-size libraries were prepared
817 and run on a PacBio RS II or Sequel (2.0 chemistry) system at the DUSGT. Nanopore sequencing
818 was carried out in-house. Single-strain libraries were prepared with either the SQK-LSK108 or
819 SQK-LSK110 kit, whereas up to three DNA samples were barcoded with the SQK-LSK109 and
820 EXP-NBD103/EXP-NBD104, or SQK-NBD114.24 kits. Libraries were prepared following the
821 manufacturer’s protocols, either individually or pooled, and sequenced on R9 (FLO-MN106) or
822 R10 (FLO-MIN114) flow cells for 48–72 h at default voltage on a MinION Mk1B or Mk1C system.
823 The MinION software version current at the time of each run was applied. Further details on
824 sequencing platforms, basecalling, and demultiplexing are provided in **S1 Appendix**.

825

826 **Genome assembly**

827 Genomes were assembled with Canu [141] using Nanopore or PacBio sequencing data
828 and default parameters. Assembly accuracy was improved through initial error correction with
829 Medaka (https://github.com/nanoporetech/medaka) for Nanopore-based assemblies, followed by
830 up to five rounds of iterative polishing with Pilon v1.22 [142] (`--fix all`) using Illumina reads
831 aligned to the first pass-polished assembly with BWA-MEM v0.7.17-r1188 [143]. Pilon iterations
832 were stopped early if no additional changes were detected, based on the absence of reported
833 corrections in each round. Contigs containing only rDNA sequences, detected by Barrnap
834 (https://github.com/tseemann/barrnap) (`--kingdom euk`), or those classified as mitochondrial
835 DNA, were excluded from the final nuclear genome assembly. To confirm assembly completeness
836 and evaluate telomeric regions, Nanopore/PacBio and Illumina reads were realigned to the Canu-

corrected assembly using minimap2 v2.9-r720 [144] and BWA-MEM, respectively, and read coverage profiles were examined in the Integrative Genomics Viewer (IGV) [145]. Draft assemblies for *K. europaea* PYCC6162 and *K. botswanensis* CBS12717 were generated with SPAdes v3.15.3 using default settings, while assemblies for *K. heveanensis* BCC8398 and *K. mangrovensis* CBS10435 were constructed with Allpaths [146]. Genome assemblies and raw sequencing data were deposited in DDBJ/EMBL/GenBank under the BioProject numbers listed in **S1 Appendix**, which also provides details on assembly parameters for each genome.

Gene prediction and annotation

Gene models were predicted using either BRAKER2 v2.1.5 [147] or Funannotate v1.8.9 (https://github.com/nextgenusfs/funannotate), as previously described [20, 23, 49]. Prior to gene prediction, assemblies were masked with RepeatMasker v4.1.4 in sensitive mode, applying a custom library that combined *Cryptococcus–Kwoniella* repeat families generated with RepeatModeler2 v2.0.4 [49], centromere-associated transposable elements, and curated *Cryptococcus* elements compiled from published sources [148] and represented in Dfam. Manual inspection and correction were performed only for mating-type gene models, guided by ortholog alignments, and included adjustments to exon–intron boundaries or addition of small ORFs missed by automated pipelines (e.g., *MF* pheromone genes). These curated annotations were incorporated into the final GFF files and are part of the genome submissions deposited in NCBI. Functional annotation was added to the final gene models using the Funannotate *"annotate"* module, which integrated data for PFAM and InterPro domains, Gene Ontology (GO) terms, fungal transcription factors, Cluster of Orthologous Genes (COGs), secondary metabolites, Carbohydrate-Active Enzymes (CAZYmes), secreted proteins, proteases (MEROPS), and Benchmarking Universal Single-Copy Orthologs (BUSCO) groups. InterPro domain data, COG annotations, and secondary metabolite predictions were generated with InterProScan v5.55-88.0,

eggNOGmapper v.2.1.7 (eggNOG DB version: 5.0.2) [149], and AntiSMASH v6.1.0 [150], and then passed to Funannotate *annotate* with the options *--iprscan, --eggnog*, and *--antismash*. Specific parameters are provided in **S1 Appendix**.

Ortholog identification and sequence alignment

To construct the phylogenomic data matrix, single-copy orthologs (SC-OGs) were identified across *Cryptococcus* and *Kwoniella* species and three outgroups (*Tremella mesenterica* ATCC28783, GCA_004117975.1; *Saitozyma podzolica* DSM27192, GCA_003942215.1; and *Bullera alba* JCM2954, GCA_001600095.1) using OrthoFinder v3.0.1b1 with options: *-M msa -S diamond_ultra_sens -I 1.5 -M msa -A mafft -T fasttree -t 48 -a 6*. This identified 3,086 SC-OGs shared across species. Their amino acid sequences were individually aligned with MAFFT v7.310 [151] (*--localpair --maxiterate 1000*) and trimmed with TrimAl v1.4.rev22 [152] (*-gappyout -keepheader*). The same approach was applied to construct the phylogenomic data matrix for *C. neoformans* strains representing different VN groups, with three *C. deneoformans* outgroups, yielding 5,439 shared SC-OGs, which were then aligned and trimmed as above.

Species phylogeny, estimation of topological support, and gene genealogies

The updated phylogeny of *Cryptococcus* and *Kwoniella* species (**Figs 1A** and **S1**) was inferred using two complementary strategies: (i) concatenation-based partitioned maximum likelihood (ML) phylogeny reconstruction in IQ-TREE v2.1.6 [153], and (ii) gene-based coalescence analysis in ASTRAL v5.7.8 [154]. For the concatenation approach, amino acid alignments of 3,086 SC-OGs were combined into a partitioned supermatrix (52 taxa, 3,086 partitions, 1,686,691 sites) using the *"-p"* option in IQ-TREE. The edge-linked proportional

partition model [155] was applied to account for differences in evolutionary rates across partitions, and the best-fit substitution model for each partition was identified with ModelFinder [156] under the Bayesian information criterion. The ML tree was inferred with the parameters `--seed 54321 -m MFP -msub nuclear -B 1000 -alrt 1000 -T 14`, incorporating 1,000 ultrafast bootstrap (UFBoot) replicates [157] and Shimodaira–Hasegawa approximate likelihood ratio tests (SH-aLRT) for branch support assessment. For the coalescence-based approach, ML gene trees were constructed for each SC-OG alignment using IQ-TREE's `"-S"` option, which performs both model selection and tree inference for individual alignments. These trees were then input to ASTRAL under default settings to reconstruct the species phylogeny. Quartet support values were computed with the `-t 2` option, providing quartet support metrics for the primary topology (q1) and alternative topologies (q2, q3), and local posterior probability (LPP) support. Genealogical concordance and topological support for branches in the concatenated ML tree were evaluated with gene concordance factor (gCF) and site concordance factor (sCF) metrics in IQ-TREE. This analysis utilized both the best-scoring concatenated ML tree (concat.treefile) and the set of gene trees (loci.treefile), with options `-t –gcf -p --scf 100`. The concatenation-based approach was also applied to resolve relationships among *C. neoformans* VN lineages (**Fig 4A**). For gene genealogies, amino acid sequences of individual genes of interest were extracted from OGs identified by OrthoFinder, manually inspected, and reannotated as needed. Alignment, trimming and ML reconstruction were performed as described above. Trees were visualized and annotated with iTOL v7. Detailed model parameters are provided in the tree files accessible at https://doi.org/10.5281/zenodo.16987438.

Synteny analyses, *MAT* loci delineation, and centromere identification

Conserved synteny blocks in pairwise genome comparisons were identified with SynChro [105], using a delta parameter of 3 for high stringency. Comparisons in **Figs 6A**, **8A** and **S9A**

911 employed the *K. shandongensis* genome as reference. Detailed linear synteny plots of
912 chromosomes and specific genomic regions, including *MAT* loci, were generated with EasyFig
913 v2.2.2 [158] using BLASTN. Centromeres positions were determined in silico as previously
914 described [49], combining detection of centromere-associated LTR elements and synteny
915 analysis. Centromere lengths were defined as the intergenic regions between flanking centromeric
916 genes (**S1 Appendix**). *MAT* loci were initially identified by BLAST searches, with *C. neoformans*-
917 derived *MAT* genes and their flanking proteins as queries. The *HD* loci were defined as the regions
918 spanning the *HD1* and *HD2* genes. The *P/R* loci were delineated based on structural comparisons
919 between mating types. For species with available strains of opposite mating types, the *P/R* locus
920 was defined as the region where synteny between the mating types is disrupted, with boundaries
921 set at the points where synteny is restored. For species with only a single strain, the *P/R* locus
922 length was inferred from the distance between *P/R*-flanking genes, as determined from
923 comparisons involving opposite mating types.

924 To infer the origin of structural rearrangements observed in the *P/R* locus in *Kwoniella* (**S5A**
925 **Fig**), we manually inspected the orientation and synteny of *P/R*-associated genes across mating
926 types and species. Rearrangement breakpoints were approximated by identifying changes in gene
927 order and orientation between alleles, supported by the presence of gene fragments (e.g., partial
928 *NDC80*, *STE12*, *BSP3*) and conserved synteny in the opposite mating type. These
929 rearrangements were reconstructed by inverting or repositioning affected gene blocks in the more
930 derived *a2* allele to match the putative ancestral configuration in the more conserved *a1* allele.

931 Statistical analyses of *MAT* loci lengths across species, clades, or mating-types were
932 conducted with Python3 with Pandas, Seaborn, Matplotlib, and SciPy libraries. Differences
933 between the two groups were assessed using the two-sided Mann–Whitney U test. Scripts and
934 raw data are available at https://doi.org/10.5281/zenodo.16987438. Plots were refined for clarity
935 by adjusting color schemes, labels, and adding features in Adobe Illustrator.

Analysis of gene content in *MAT* loci, frequency across species, and gene essentiality classification

A curated gene presence/absence matrix was constructed after delineating *MAT* loci across species. Genes were categorized as “present” (1), “absent” (0), “unclear” (?), or “pseudogene” (pseudo). Unclear cases indicated instances where gene presence could not be conclusively determined due to uncertain locus boundaries. For frequency calculations, pseudogenes were treated as present and unclear cases as absent. The presence of either *SXI1* or *SXI2* was scored as present and combined for frequency estimates. Information on gene essentiality was inferred from *C. neoformans* H99, based on experimentally validated studies [34, 159, 160] or predictions from a high-throughput transposon mutagenesis (TN-seq) study [92]. Gene essentiality in other species was extrapolated solely from H99, and genes without H99 orthologs were categorized as “unknown” due to the lack of supporting data. A custom R script (`0_calculate_gene_presence_frequency.R`) analyzed and plotted gene presence frequencies. The matrix was also visualized as a heatmap (`1_plot_gene_matrix_based_on_frequency.R`), with genes ordered by frequency. *SXI1* and *SXI2* are shown as separate columns in the heatmap, but their ranking reflects their combined frequency. Analyses and visualizations were conducted in R with dplyr, ggplot2, ComplexHeatmap, and circlize packages. Gene presence/absence was further analyzed with a Python script (`2_compare_MAT_gene_content_across_clades.py`), which calculated clade-specific and pairwise presence, identified genes shared across specified clades, and highlighted clade-specific genes. Input matrices are provided in **S2 and S3 Appendices** and scripts are available at https://doi.org/10.5281/zenodo.16987438.

Base composition and codon-bias analyses

Genome-wide GC content and deviations from the mean GC% were analyzed with a custom Python script (*00_gc_content_analysis_and_plots.py*), employing a non-overlapping sliding window (1 kb for genome scans; 0.25 kb for zoomed-in views). Regions of interest (e.g., *P/R* loci) were highlighted from BED file coordinates. Plots were further refined in Adobe Illustrator for producing **Fig 2**. To assess whether the *P/R* locus exhibited lower GC content than genome-wide averages, a second script (*01_gc_content_analysis.py*) compared *P/R* locus GC% to 1,000 randomly sampled genome-wide regions of equal size (excluding the *P/R* locus). A one-sample *t*-test assessed whether the *P/R* locus GC content differed from the sampled mean, while a permutation test (10,000 iterations) generated a null distribution to calculate *P*-values and Z-scores. The analysis was automated with a shell script (*01a_run_script_vs_wg.sh*), consolidating results into a summary table (**S4 Appendix**).

To assess whether GC depletion within the *P/R* locus reflects reduced GC-biased gene conversion (gBGC) or relaxed selection on codon usage, we performed a four-step Python3-based analysis (NumPy, pandas, SciPy, Biopython): (i) neutral non-coding GC comparison, (ii) coding third-position composition (AT3 vs GC3), (iii) codon-bias indices (Fop, Nc, ENC, ΔENC), and (iv) CAI analyses controlling for GC3 and CDS length (details in **S1 Text**). As preparation for CAI-related analyses, species-specific CAI reference sets were generated with a custom script (*02_build_cai_reference.py*) in *"rp_only"* mode, selecting ribosomal-protein genes as proxies for highly expressed, codon-optimized, genes [161, 162], since RNA-seq data for these species was unavailable. The script counted codons and generated a CAI weight table in which, within each synonymous family, relative adaptiveness weights (w) were normalized so that the most frequent codon had $w = 1$ and others $0 < w \leq 1$. Per-gene CAI values were then computed with *03_compute_cai_per_gene.py*, which reads each species' CAI weight table and CDS

annotations and returns gene-level CAI (geometric mean of *w* across codons; start/stop excluded; non-ACGT ignored; Met/Trp treated as neutral set to *w = 1*).

To test for GC depletion in the *P/R* region, non-coding GC within *P/R* (intergenic plus introns) was compared to same-chromosome, length-matched nulls with script *04_neutral_non_coding_GC.py* using 10,000 *P/R*-excluded windows (*--n_null 10000 --no_overlap --min_gap 1000*). The script reports ΔGC (*gc_intergenic* – *null_mean_intergenic*), a standardized *z*, and a one-sided empirical permutation p-value (PR ≤ null).

Coding third-position composition (AT3 vs GC3) was analyzed with script *05_coding_composition_and_codon_bias.py* by counting AT- vs GC-ending third positions inside *P/R* and background regions (same chromosome, outside *P/R*) and testing the 2×2 table by χ^2 with Fisher's exact fallback. Using the same script and the CAI weights above, codon-bias indices were calculate: Fop (frequency of optimal codons based on the CAI reference); Nc (effective number of codons, representing the observed codon usage bias in a gene); ENC (the expected Nc based solely on the gene's GC3, calculated from the GC3–Nc relationship described by Wright (1990) [163]); and ΔENC = Nc − ENC (representing codon bias beyond that expected from GC3 composition alone). To improve the stability of Nc estimates, particularly for short CDS, we applied a small pseudocount (0.5 per codon), excluded very small synonymous families, bounded intermediate calculations to avoid division by near-zero values, and constrained Nc values to the theoretical range of 20 (maximum bias) to 61 (no bias) before computing ΔENC. *P/R* versus background contrasts were evaluated as median differences using Mann–Whitney tests with 10,000 permutations.

Finally, CAI differences independent of nucleotide composition were tested using three complementary analyses implemented in script *06_cai_vs_gc3_controls.py* (detailed in **S1 Text**), using the following parameters: *--n_perm 10000*, *--gc3_tol 0.03*, *--len_tol 0.10*, and *--k_match 5*. Briefly, we (i) fit CAI ~ inside_pr + Δ(exon-intron GC) + log(length_cds) to all genes

using ordinary-least-squares (OLS) with heteroskedasticity-consistent (HC1) robust standard errors; inside_pr = 1 for CDS fully within the *P/R* window and 0 for same-chromosome genes outside (boundary overlaps excluded); (ii) we trained CAI ~ Δ(exon-intron GC) + log(length_cds) on background genes only, computed residuals for all genes, and tested median(PR residual) − median(BG residual) with a one-sided permutation test (10,000 shuffles; alternative PR < BG); and (iii) we matched each *P/R* locus gene to same-chromosome controls within ±0.03 GC3 and ±10% CDS length (dropping unmatched *P/R* genes), computed *CAI_match_median = median[CAI_PR − mean(CAI_BG matches)]*, and used a sign-flip permutation test (10,000 flips; alternative PR < BG). Fop was analyzed identically to step (iii) with the same matching tolerances and permutation settings. All scripts are available at https://doi.org/10.5281/zenodo.16987438, and per-species summaries and statistical tests are given in **S4 Appendix**.

Variant analysis and SNP distribution in *C. neoformans MAT*a strains

Multi-genome variant analysis was performed with the Snippy pipeline v4.6.0 (https://github.com/tseemann/snippy) using the newly assembled genome of *C. neoformans* Ftc555-1 (VNBI) as the reference, with parameters: `--cpus 10, --unmapped, --mincov 10, and --minfrac 0.9`. Paired-end reads were obtained from the NCBI SRA database (**S1 Appendix**). Three datasets were independently used: (i) the entire genome, (ii) only the *MAT* locus region (chr_5:153,773-277,230), and (iii) only chr. 5. The *MAT* locus and chr. 5 were extracted from the reference genome to generate region-specific GenBank files for Snippy to identify SNPs and construct region-specific phylogenies. Visualization of SNV distributions was based on the whole-genome dataset and included both chromosome-wide and zoomed-in views of specific regions. A custom Python script processed merged SNV datasets, computed total SNP counts for each strain, and generated gradient color-coded SNP density plots. Final composite figures were refined using Adobe Illustrator. Core SNP alignments (core.aln) from each dataset were used for

1034 phylogenetic reconstruction with IQ-TREE2, incorporating 10,000 UFBoot replicates and SH-
1035 aLRT tests for branch support. Scripts for SNV analysis and visualization are available at
1036 https://doi.org/10.5281/zenodo.16987438.

1037

1038 **Chromosome composition analysis of *K. mangrovensis* progeny**

1039 To characterize chromosome composition in *K. mangrovensis* progeny, a combined
1040 nuclear reference genome was constructed from assemblies of the two parental strains, CBS8507
1041 and CBS10435. For CBS8507, the original assembly consisted of four contigs, two of which
1042 represented the same chromosome fragmented at the rDNA array. To streamline downstream
1043 analyses and facilitate interpretation, the two contigs were merged into a single scaffold:
1044 orientation was first established from rDNA gene direction; the corresponding ends were aligned
1045 and trimmed; and a 5-N gap was inserted to join them, yielding a finalized three-chromosome
1046 assembly. For CBS10435, the draft assembly of 37 contigs was reordered and reoriented to match
1047 the CBS8507 3-chromosome assembly using D-GENIES [164], which employs minimap2 for
1048 genome alignment. Raw Illumina paired-end reads from selected progeny were then mapped to a
1049 combined reference with the sppIDer pipeline [165], which sequentially mapped reads, applied
1050 stringent quality filtering (MQ > 3), and generated depth-of-coverage plots. Chromosome number
1051 and ploidy were estimated by integrating spider coverage data with flow cytometry results.

1052

1053 **Mating assays, phenotyping on mating inducing media, and microscopy**

1054 Mating assays with *K. mangrovensis* strains CBS8507 and CBS10435 were performed as
1055 previously described [66, 67]. Equal amounts of cells from each strain were mixed on V8 agar (10
1056 g/L yeast extract, 20 g/L Bacto Peptone, 20 g/L dextrose, 20 g/L agar; pH 5) or corn meal agar
1057 (CMA; 15 g/L corn meal agar, 5 g/L agar) and incubated in the dark at room temperature (20-23°C)

1058 for up to one month. Plates were regularly monitored for the development of mating structures.
1059 Random F1 progeny were recovered by microdissecting individual cells from cell clusters [79]
1060 embedded in or on the surface of the mating media (V8 and CMA) at the edges of mating patches.
1061 A total of 51 progeny were collected, grown axenically on YPD plates, and stored as glycerol
1062 stocks at -80 °C. Selected F1 progeny (MP11, MP15, MP16, MP18, MP49, MP50, MP51, MP54
1063 and MP59) were assessed for hyphal formation and mating structures on V8 pH5 and CMA,
1064 compared to the parental cross (CBS8507 x CBS10432) and the solo culture of each parental
1065 strain. Potentially compatible strain pairs from *Cryptococcus* species lacking documented sexual
1066 reproduction (IND107 × CBS11718; CBS11687 × 7685027; and DSM108351 × NCYC1536) were
1067 tested for mating ability under conditions known to induce mating in *C. neoformans* and *C.*
1068 *deneoformans* (V8 media, dark, room temperature) for up to a month, with regular monitoring [79].
1069 Solo cultures of each strain were also evaluated for their ability to reproduce sexually without a
1070 compatible partner. Similar assays were performed for strains of newly described species lacking
1071 known compatible partners. All mating assays were repeated three separate times to ensure
1072 consistent phenotypic observations. To assess hyphal growth, basidia, and spores, the edges of
1073 yeast colonies and mating patches were examined and photographed with a Zeiss Axio Scope.A1
1074 microscope equipped with an Axiocam Color camera and ZEN Lite v3.4 software.

1075

1076 Analysis of *K. mangrovensis* progeny by PCR-restriction fragment length 1077 polymorphism (RFLP) analysis

1078 *Kwoniella mangrovensis* has only three chromosomes. To analyze the F1 progeny from
1079 the CBS8507 × CBS10432 crosses, six primer pairs (one per chromosomal arm) were designed
1080 for the initial screening. Primers were manually designed to produce distinct parental patterns after
1081 PCR product digestion with specific restriction enzymes. As a heterozygosity control, PCR
1082 products from a 1:1 DNA mixture of both parental strains were amplified for each primer pair,

1083 followed by digestion with the corresponding restriction enzyme. Results and primer sequences
1084 are provided in **S5 Appendix**.

1085

1086 ## Fluorescence-activated cell-sorting (FACS)

1087 FACS was performed as previously described [166] to determine ploidy of *K. mangrovensis*
1088 CBS8507, CBS10432, and nine selected progeny. Strains were grown overnight at room
1089 temperature (21-23°C) on YPD medium, harvested, and washed with PBS. Cells were fixed in 2
1090 ml of 70% ethanol at 4°C overnight, washed with 1 ml of NS buffer (10 mM Tris-HCl pH 7.2, 250
1091 mM sucrose, 1 mM EDTA pH 8.0, 1 mM $MgCl_2$, 0.1mM $CaCl_2$, 0.1 mM $ZnCl_2$, 0.4 mM
1092 phenylmethylsulfonyl fluoride, and 7 mM β-mercaptoethanol), and then stained with 5 µl of
1093 propidium iodide (0.5 mg/ml) in 180 µl NS buffer with 20 µl of RNase (10 mg/ml) at 4°C overnight.
1094 Lastly, 50 µl of stained cells were diluted in 2 ml of 50 mM Tris-HCl pH 8.0 and sonicated for 1 min
1095 before analysis at the Duke Cancer Institute Flow Cytometry Shared Resource. Data were
1096 collected from 10,000 cells using the FL1 channel on a Becton-Dickinson FACScan and analyzed
1097 with FlowJo software. Strains JEC21 and XL143 served as haploid and diploid controls,
1098 respectively [167].

Funding Statement

This study was supported by the National Institute of Allergy and Infectious Diseases of the National Institutes of Health under awards R01 AI050113-20 (J.H.), R01 AI039115-27 (J.H.), and R01 AI33654-08 (J.H.). We note that these collaborative studies were concluded prior to June 27, 2025. Funding for the collection of *Cryptococcus* isolates from bark beetles in South Africa was supported entirely and independently by the Harry Oppenheimer Fellowship Award of The Oppenheimer Memorial Trust (to M.J.W) and the SARChI Chair in Fungal Genomics, supported by the Department of Science and Innovation (DSI)/National Research Foundation (NRF), South Africa (to B.D.W.). JH is Co-Director and Fellow of the CIFAR program Fungal Kingdom: Threats & Opportunities. The funders had no role in study design, data collection and analysis, decision to publish, or preparation of the manuscript.

Acknowledgements

We thank Vikas Yadav for assistance with Nanopore data acquisition, Terrance Shea and Christina Cuomo for providing the genomes assemblies of *K. mangrovensis* CBS8886 and CBS10435, as well as *K. heveanensis* BCC8398, and the Broad Institute Genomics Platform for generating Illumina sequencing data for these three strains. We also thank Fred Dietrich for computational resources, Prof Francois Roets for providing permits to collect specimens in South Africa, and Minou Nowrousian for critical reading of this manuscript.

Author contributions

Conceptualization: Marco A. Coelho, Márcia David-Palma, Joseph Heitman

Data Curation: Marco A. Coelho, Márcia David-Palma

Formal analysis: Marco A. Coelho

Funding acquisition: Brenda D. Wingfield, Michael J. Wingfield, Joseph Heitman

Investigation: Marco A. Coelho, Márcia David-Palma, Nam Pham, Seonju Marincowitz, Janneke Aylward, Sheng Sun

Project Administration: Brenda D. Wingfield, Michael J. Wingfield, Joseph Heitman

Resources: Andrey M. Yurkov, Brenda D. Wingfield, Michael J. Wingfield, Joseph Heitman

Software: Marco A. Coelho

Supervision: Joseph Heitman

Visualization: Marco A. Coelho, Márcia David-Palma

Writing – original draft: Marco A. Coelho, Márcia David-Palma

Writing – review & editing: Marco A. Coelho, Márcia David-Palma, Nam Pham, Seonju Marincowitz, Janneke Aylward, Andrey M. Yurkov, Brenda D. Wingfield, Michael J. Wingfield, Sheng Sun, Joseph Heitman

References

1. Otto SP, Lenormand T. Resolving the paradox of sex and recombination. Nat Rev Genet. 2002;3(4):252-61. Epub 2002/04/23. doi: 10.1038/nrg761. PubMed PMID: 11967550.

2. de Visser JA, Elena SF. The evolution of sex: empirical insights into the roles of epistasis and drift. Nat Rev Genet. 2007;8(2):139-49. Epub 2007/01/19. doi: 10.1038/nrg1985. PubMed PMID: 17230200.

3. Goodenough U, Heitman J. Origins of eukaryotic sexual reproduction. Cold Spring Harb Perspect Biol. 2014;6(3). Epub 2014/03/05. doi: 10.1101/cshperspect.a016154. PubMed PMID: 24591519; PubMed Central PMCID: PMCPMC3949356.

4. Hawksworth DL, Lucking R. Fungal diversity revisited: 2.2 to 3.8 million species. Microbiol Spectr. 2017;5(4). doi: 10.1128/microbiolspec.FUNK-0052-2016. PubMed PMID: 28752818; PubMed Central PMCID: PMCPMC11687528.

5. Heitman J, Howlett BJ, Crous PW, Stukenbrock EH, James TY, Gow NAR. The Fungal Kingdom: American Society of Microbiology; 2017.

6. Begerow D, Kemler M, Feige A, Yurkov A. Parasitism in yeasts. In: Buzzini P, Lachance M-A, Yurkov A, editors. Yeasts in Natural Ecosystems: Ecology. Cham: Springer International Publishing; 2017. p. 179-210.

7. Lee SC, Ni M, Li W, Shertz C, Heitman J. The evolution of sex: a perspective from the fungal kingdom. Microbiol Mol Biol Rev. 2010;74(2):298-340. Epub 2010/05/29. doi: 10.1128/MMBR.00005-10. PubMed PMID: 20508251; PubMed Central PMCID: PMCPMC2884414.

8. Lin X, Heitman J. Mechanisms of homothallism in Fungi and transitions between heterothallism and homothallism. In: Heitman J, Kronstad JW, Taylor JW, Casselton LA, editors. Sex in fungi: Molecular determination and evolutionary implications. Washington D.C.: ASM Press; 2007. p. 35-57.

9. Coelho MA, Bakkeren G, Sun S, Hood ME, Giraud T. Fungal Sex: the Basidiomycota. Microbiol Spectr. 2017;5(3):10.1128/microbiolspec.FUNK-0046-2016. Epub 2017/06/10. doi: 10.1128/microbiolspec.FUNK-0046-2016. PubMed PMID: 28597825; PubMed Central PMCID: PMCPMC5467461.

10. Kües U, James TY, Heitman J. Mating type in basidiomycetes: unipolar, bipolar, and tetrapolar patterns of sexuality. In: Pöggeler S, Wöstemeyer J, editors. Evolution of fungi and Fungal-like organisms. The Mycota. 6. Heidelberg, Germany: Springer Berlin Heidelberg; 2011. p. 97-160.

11. James TY, Srivilai P, Kues U, Vilgalys R. Evolution of the bipolar mating system of the mushroom *Coprinellus disseminatus* from its tetrapolar ancestors involves loss of mating-type-specific pheromone receptor function. Genetics. 2006;172(3):1877-91. Epub 2006/02/08. doi: 10.1534/genetics.105.051128. PubMed PMID: 16461425; PubMed Central PMCID: PMCPMC1456265.

12. Yi R, Tachikawa T, Ishikawa M, Mukaiyama H, Bao D, Aimi T. Genomic structure of the *A* mating-type locus in a bipolar basidiomycete, *Pholiota nameko*. Mycol Res. 2009;113(Pt 2):240-8. Epub 20081119. doi: 10.1016/j.mycres.2008.11.002. PubMed PMID: 19049868.

13. James TY, Lee M, van Diepen LT. A single mating-type locus composed of homeodomain genes promotes nuclear migration and heterokaryosis in the white-rot fungus *Phanerochaete chrysosporium*. Eukaryot Cell. 2011;10(2):249-61. Epub 20101203. doi: 10.1128/EC.00212-10. PubMed PMID: 21131435; PubMed Central PMCID: PMCPMC3067404.

14. Olson A, Aerts A, Asiegbu F, Belbahri L, Bouzid O, Broberg A, et al. Insight into trade-off between wood decay and parasitism from the genome of a fungal forest pathogen. New Phytol. 2012;194(4):1001-13. Epub 20120328. doi: 10.1111/j.1469-8137.2012.04128.x. PubMed PMID: 22463738.

15. Bakkeren G, Kronstad JW. Linkage of mating-type loci distinguishes bipolar from tetrapolar mating in basidiomycetous smut fungi. Proc Natl Acad Sci U S A. 1994;91(15):7085-9. Epub 1994/07/19. doi: 10.1073/pnas.91.15.7085. PubMed PMID: 7913746; PubMed Central PMCID: PMCPMC44343.

16. Lengeler KB, Fox DS, Fraser JA, Allen A, Forrester K, Dietrich FS, et al. Mating-type locus of *Cryptococcus neoformans*: a step in the evolution of sex chromosomes. Eukaryot Cell. 2002;1(5):704-18. doi: 10.1128/ec.1.5.704-718.2002. PubMed PMID: 12455690; PubMed Central PMCID: PMCPMC126754.

17. Badouin H, Hood ME, Gouzy J, Aguileta G, Siguenza S, Perlin MH, et al. Chaos of rearrangements in the mating-type chromosomes of the anther-smut fungus microbotryum lychnidis-dioicae. Genetics. 2015;200(4):1275-84. Epub 2015/06/06. doi: 10.1534/genetics.115.177709. PubMed PMID: 26044594; PubMed Central PMCID: PMCPMC4574255.

18. Sun S, Coelho MA, Heitman J, Nowrousian M. Convergent evolution of linked mating-type loci in basidiomycete fungi. PLOS Genet. 2019;15(9):e1008365. Epub 2019/09/07. doi: 10.1371/journal.pgen.1008365. PubMed PMID: 31490920; PubMed Central PMCID: PMCPMC6730849.

19. Gioti A, Nystedt B, Li W, Xu J, Andersson A, Averette AF, et al. Genomic insights into the atopic eczema-associated skin commensal yeast *Malassezia sympodialis*. mBio. 2013;4(1):e00572-12. Epub 2013/01/24. doi: 10.1128/mBio.00572-12. PubMed PMID: 23341551; PubMed Central PMCID: PMCPMC3560662.

20. Coelho MA, Ianiri G, David-Palma M, Theelen B, Goyal R, Narayanan A, et al. Frequent transitions in mating-type locus chromosomal organization in *Malassezia* and early steps in sexual reproduction. Proc Natl Acad Sci U S A. 2023;120(32):e2305094120. Epub 2023/07/31. doi: 10.1073/pnas.2305094120. PubMed PMID: 37523560; PubMed Central PMCID: PMCPMC10410736.

21. David-Palma M, Sampaio JP, Gonçalves P. Genetic dissection of sexual reproduction in a primary homothallic basidiomycete. PLOS Genet. 2016;12(6):e1006110. Epub 2016/06/22. doi: 10.1371/journal.pgen.1006110. PubMed PMID: 27327578; PubMed Central PMCID: PMCPMC4915694.

22. Cabrita A, David-Palma M, Brito PH, Heitman J, Coelho MA, Goncalves P. Multiple pathways to homothallism in closely related yeast lineages in the Basidiomycota. mBio. 2021;12(1). Epub 2021/02/18. doi: 10.1128/mBio.03130-20. PubMed PMID: 33593979; PubMed Central PMCID: PMCPMC8545103.

23. Passer AR, Clancey SA, Shea T, David-Palma M, Averette AF, Boekhout T, et al. Obligate sexual reproduction of a homothallic fungus closely related to the *Cryptococcus* pathogenic species complex. eLife. 2022;11. Epub 2022/06/18. doi: 10.7554/eLife.79114. PubMed PMID: 35713948; PubMed Central PMCID: PMCPMC9296135.

24. Wang YW, McKeon MC, Elmore H, Hess J, Golan J, Gage H, et al. Invasive Californian death caps develop mushrooms unisexually and bisexually. Nat Commun. 2023;14(1):6560. Epub 2023/10/25. doi: 10.1038/s41467-023-42317-z. PubMed PMID: 37875491; PubMed Central PMCID: PMCPMC10598064.

25. Lin X, Hull CM, Heitman J. Sexual reproduction between partners of the same mating type in *Cryptococcus neoformans*. Nature. 2005;434(7036):1017-21. doi: 10.1038/nature03448. PubMed Central PMCID: PMCPMID: 15846346.

26. Maia TM, Lopes ST, Almeida JM, Rosa LH, Sampaio JP, Goncalves P, et al. Evolution of mating systems in basidiomycetes and the genetic architecture underlying mating-type determination in the yeast *Leucosporidium scottii*. Genetics. 2015;201(1):75-89. Epub 2015/07/17. doi: 10.1534/genetics.115.177717. PubMed PMID: 26178967; PubMed Central PMCID: PMCPMC4566278.

27. Branco S, Carpentier F, Rodriguez de la Vega RC, Badouin H, Snirc A, Le Prieur S, et al. Multiple convergent supergene evolution events in mating-type chromosomes. Nat Commun. 2018;9(1):2000.

Epub 2018/05/23. doi: 10.1038/s41467-018-04380-9. PubMed PMID: 29784936; PubMed Central PMCID: PMCPMC5962589.

28. Nieuwenhuis BP, Billiard S, Vuilleumier S, Petit E, Hood ME, Giraud T. Evolution of uni- and bifactorial sexual compatibility systems in fungi. Heredity. 2013;111(6):445-55. Epub 2013/07/11. doi: 10.1038/hdy.2013.67. PubMed PMID: 23838688; PubMed Central PMCID: PMCPMC3833681.

29. James TY. Why mushrooms have evolved to be so promiscuous: Insights from evolutionary and ecological patterns. Fungal Biol Rev. 2015;29(3):167-78. doi: https://doi.org/10.1016/j.fbr.2015.10.002.

30. Taniguti LM, Schaker PD, Benevenuto J, Peters LP, Carvalho G, Palhares A, et al. Complete genome sequence of *Sporisorium scitamineum* and biotrophic interaction transcriptome with sugarcane. PLOS ONE. 2015;10(6):e0129318. Epub 20150612. doi: 10.1371/journal.pone.0129318. PubMed PMID: 26065709; PubMed Central PMCID: PMCPMC4466345.

31. Depotter JRL, Okmen B, Ebert MK, Beckers J, Kruse J, Thines M, et al. High nucleotide substitution rates associated with retrotransposon proliferation drive dynamic secretome evolution in smut pathogens. Microbiol Spectr. 2022;10(5):e0034922. Epub 20220816. doi: 10.1128/spectrum.00349-22. PubMed PMID: 35972267; PubMed Central PMCID: PMCPMC9603552.

32. Carpentier F, Rodriguez de la Vega RC, Branco S, Snirc A, Coelho MA, Hood ME, et al. Convergent recombination cessation between mating-type genes and centromeres in selfing anther-smut fungi. Genome Res. 2019;29(6):944-53. Epub 20190501. doi: 10.1101/gr.242578.118. PubMed PMID: 31043437; PubMed Central PMCID: PMCPMC6581054.

33. Duhamel M, Carpentier F, Begerow D, Hood ME, Rodriguez de la Vega RC, Giraud T. Onset and stepwise extensions of recombination suppression are common in mating-type chromosomes of *Microbotryum* anther-smut fungi. J Evol Biol. 2022;35(12):1619-34. Epub 20220310. doi: 10.1111/jeb.13991. PubMed PMID: 35271741; PubMed Central PMCID: PMCPMC10078771.

34. Fraser JA, Diezmann S, Subaran RL, Allen A, Lengeler KB, Dietrich FS, et al. Convergent evolution of chromosomal sex-determining regions in the animal and fungal kingdoms. PLOS Biol. 2004;2(12):e384. doi: 10.1371/journal.pbio.0020384. PubMed PMID: 15538538; PubMed Central PMCID: PMCPMC526376.

35. Sun S, Yadav V, Billmyre RB, Cuomo CA, Nowrousian M, Wang L, et al. Fungal genome and mating system transitions facilitated by chromosomal translocations involving intercentromeric recombination. PLOS Biol. 2017;15(8):e2002527. Epub 2017/08/12. doi: 10.1371/journal.pbio.2002527. PubMed PMID: 28800596; PubMed Central PMCID: PMCPMC5568439.

36. Nichols CB, Fraser JA, Heitman J. PAK kinases Ste20 and Pak1 govern cell polarity at different stages of mating in *Cryptococcus neoformans*. Mol Biol Cell. 2004;15(10):4476-89. Epub 2004/07/30. doi: 10.1091/mbc.e04-05-0370. PubMed PMID: 15282344; PubMed Central PMCID: PMCPMC519142.

37. Sun S, Coelho MA, David-Palma M, Priest SJ, Heitman J. The evolution of sexual reproduction and the mating-type locus: links to pathogenesis of *Cryptococcus* human pathogenic fungi. Annu Rev Genet. 2019;53(1):417-44. doi: 10.1146/annurev-genet-120116-024755. PubMed PMID: 31537103.

38. Branco S, Badouin H, Rodriguez de la Vega RC, Gouzy J, Carpentier F, Aguileta G, et al. Evolutionary strata on young mating-type chromosomes despite the lack of sexual antagonism. Proc Natl Acad Sci U S A. 2017;114(27):7067-72. Epub 2017/06/21. doi: 10.1073/pnas.1701658114. PubMed PMID: 28630332; PubMed Central PMCID: PMCPMC5502610.

39. Hartmann FE, Duhamel M, Carpentier F, Hood ME, Foulongne-Oriol M, Silar P, et al. Recombination suppression and evolutionary strata around mating-type loci in fungi: documenting patterns and understanding evolutionary and mechanistic causes. New Phytol. 2021;229(5):2470-91. Epub 2020/10/29. doi: 10.1111/nph.17039. PubMed PMID: 33113229; PubMed Central PMCID: PMCPMC7898863.

40. Hagen F, Khayhan K, Theelen B, Kolecka A, Polacheck I, Sionov E, et al. Recognition of seven species in the *Cryptococcus gattii*/*Cryptococcus neoformans* species complex. Fungal Genetics and Biology. 2015;78:16-48. doi: https://doi.org/10.1016/j.fgb.2015.02.009.

41. Farrer RA, Chang M, Davis MJ, van Dorp L, Yang D-H, Shea T, et al. A new lineage of *Cryptococcus gattii* (VGV) discovered in the Central Zambezian Miombo Woodlands. mBio. 2019;10(6):e02306-19. doi: 10.1128/mBio.02306-19.

42. Fisher MC, Denning DW. The WHO fungal priority pathogens list as a game-changer. Nat Rev Microbiol. 2023;21(4):211-2. doi: 10.1038/s41579-023-00861-x. PubMed PMID: 36747091; PubMed Central PMCID: PMCPMC9901396.

43. Casalini G, Giacomelli A, Antinori S. The WHO fungal priority pathogens list: a crucial reappraisal to review the prioritisation. Lancet Microbe. 2024;5(7):717-24. Epub 20240409. doi: 10.1016/S2666-5247(24)00042-9. PubMed PMID: 38608682.

44. Ginns J, Bernicchia A. *Filobasidiella lutea*: parasitism of *Hypochnicium vellereum*. Karstenia. 2000;40:49-51.

45. Findley K, Rodriguez-Carres M, Metin B, Kroiss J, Fonseca A, Vilgalys R, et al. Phylogeny and phenotypic characterization of pathogenic *Cryptococcus* species and closely related saprobic taxa in the Tremellales. Eukaryot Cell. 2009;8(3):353-61. Epub 2009/01/20. doi: 10.1128/EC.00373-08. PubMed PMID: 19151324; PubMed Central PMCID: PMCPMC2653247.

46. Liu XZ, Wang QM, Goker M, Groenewald M, Kachalkin AV, Lumbsch HT, et al. Towards an integrated phylogenetic classification of the Tremellomycetes. Stud Mycol. 2015;81:85-147. doi: 10.1016/j.simyco.2015.12.001. PubMed PMID: 26955199; PubMed Central PMCID: PMCPMC4777781.

47. Passer AR, Coelho MA, Billmyre RB, Nowrousian M, Mittelbach M, Yurkov AM, et al. Genetic and genomic analyses reveal boundaries between species closely related to *Cryptococcus* pathogens. mBio. 2019;10(3):e00764-19. doi: 10.1128/mBio.00764-19. PubMed PMID: 31186317; PubMed Central PMCID: PMCPMC6561019.

48. Kachalkin AV, Turchetti B, Inácio J, Carvalho C, Mašínová T, Pontes A, et al. Rare and undersampled dimorphic basidiomycetes. Mycol Prog. 2019. doi: 10.1007/s11557-019-01491-5.

49. Coelho MA, David-Palma M, Shea T, Bowers K, McGinley-Smith S, Mohammad AW, et al. Comparative genomics of the closely related fungal genera *Cryptococcus* and *Kwoniella* reveals karyotype dynamics and suggests evolutionary mechanisms of pathogenesis. PLOS Biol. 2024;22(6):e3002682. Epub 2024/06/06. doi: 10.1371/journal.pbio.3002682. PubMed PMID: 38843310; PubMed Central PMCID: PMCPMC11185503 declared that no competing interests exist.

50. Coelho MA, David-Palma M, Aylward J, Pham NQ, Visagie CM, Fuchs T, et al. Decoding *Cryptococcus*: from African biodiversity to worldwide prevalence. PLOS Pathogens. 2025;21(2):e1012876. doi: 10.1371/journal.ppat.1012876.

51. Chen R, Jiang YM, Wei SC, Wang QM. *Kwoniella shandongensis* sp. nov., a basidiomycetous yeast isolated from soil and bark from an apple orchard. Int J Syst Evol Microbiol. 2012;62(Pt 11):2774-7. Epub 2012/03/27. doi: 10.1099/ijs.0.039172-0. PubMed PMID: 22447698.

52. Statzell-Tallman A, Belloch C, Fell JW. *Kwoniella mangroviensis* gen. nov., sp.nov. (*Tremellales*, *Basidiomycota*), a teleomorphic yeast from mangrove habitats in the Florida Everglades and Bahamas. FEMS Yeast Res. 2008;8(1):103-13. Epub 2007/10/27. doi: 10.1111/j.1567-1364.2007.00314.x. PubMed PMID: 17961172.

53. Wang L, Zhai B, Lin X. The link between morphotype transition and virulence in *Cryptococcus neoformans*. PLOS Pathog. 2012;8(6):e1002765. Epub 20120621. doi: 10.1371/journal.ppat.1002765. PubMed PMID: 22737071; PubMed Central PMCID: PMCPMC3380952.

54. Heitman J, Carter DA, Dyer PS, Soll DR. Sexual reproduction of human fungal pathogens. Cold Spring Harb Perspect Med. 2014;4(8):a019281. Epub 2014/08/03. doi:

10.1101/cshperspect.a019281. PubMed PMID: 25085958; PubMed Central PMCID: PMCPMC4109574.

55. Zhao Y, Lin X. *Cryptococcus neoformans*: sex, morphogenesis, and virulence. Infect Genet Evol. 2021;89:104731. Epub 20210123. doi: 10.1016/j.meegid.2021.104731. PubMed PMID: 33497839; PubMed Central PMCID: PMCPMC8092418.

56. Phadke SS, Feretzaki M, Heitman J. Unisexual reproduction enhances fungal competitiveness by promoting habitat exploration via hyphal growth and sporulation. Eukaryot Cell. 2013;12(8):1155-9. Epub 20130621. doi: 10.1128/EC.00147-13. PubMed PMID: 23794511; PubMed Central PMCID: PMCPMC3754539.

57. Fu C, Thielhelm TP, Heitman J. Unisexual reproduction promotes competition for mating partners in the global human fungal pathogen *Cryptococcus deneoformans*. PLOS Genet. 2019;15(9):e1008394. Epub 2019/09/20. doi: 10.1371/journal.pgen.1008394. PubMed PMID: 31536509; PubMed Central PMCID: PMCPMC6772093.

58. Wang L, Lin X. The morphotype heterogeneity in *Cryptococcus neoformans*. Curr Opin Microbiol. 2015;26:60-4. Epub 20150619. doi: 10.1016/j.mib.2015.06.003. PubMed PMID: 26094087.

59. Fu MS, Liporagi-Lopes LC, Dos Santos SRJ, Tenor JL, Perfect JR, Cuomo CA, et al. Amoeba predation of *Cryptococcus* neoformans results in pleiotropic changes to traits associated with virulence. mBio. 2021;12(2). Epub 20210427. doi: 10.1128/mBio.00567-21. PubMed PMID: 33906924; PubMed Central PMCID: PMCPMC8092252.

60. Sauters TJC, Roth C, Murray D, Sun S, Floyd Averette A, Onyishi CU, et al. Amoeba predation of *Cryptococcus*: A quantitative and population genomic evaluation of the accidental pathogen hypothesis. PLOS Pathog. 2023;19(11):e1011763. Epub 20231113. doi: 10.1371/journal.ppat.1011763. PubMed PMID: 37956179; PubMed Central PMCID: PMCPMC10681322.

61. Idnurm A. Isolation of a fungal calcineurin A mutant suggests that amoebae can counter-select virulence attributes of microbes. Med Mycol. 2023;61(2). doi: 10.1093/mmy/myad013. PubMed PMID: 36708172; PubMed Central PMCID: PMCPMC9927882.

62. Price CTD, Hanford HE, Al-Quadan T, Santic M, Shin CJ, Da'as MSJ, et al. Amoebae as training grounds for microbial pathogens. mBio. 2024;15(8):e0082724. Epub 20240708. doi: 10.1128/mbio.00827-24. PubMed PMID: 38975782; PubMed Central PMCID: PMCPMC11323580.

63. Velagapudi R, Hsueh YP, Geunes-Boyer S, Wright JR, Heitman J. Spores as infectious propagules of *Cryptococcus neoformans*. Infect Immun. 2009;77(10):4345-55. Epub 2009/07/22. doi: 10.1128/IAI.00542-09. PubMed PMID: 19620339; PubMed Central PMCID: PMCPMC2747963.

64. Walsh NM, Botts MR, McDermott AJ, Ortiz SC, Wuthrich M, Klein B, et al. Infectious particle identity determines dissemination and disease outcome for the inhaled human fungal pathogen *Cryptococcus*. PLOS Pathog. 2019;15(6):e1007777. Epub 2019/06/28. doi: 10.1371/journal.ppat.1007777. PubMed PMID: 31247052; PubMed Central PMCID: PMCPMC6597114.

65. Ortiz SC, Hull CM. Biogenesis, germination, and pathogenesis of *Cryptococcus* spores. Microbiol Mol Biol Rev. 2024;88(1):e0019623. Epub 20240305. doi: 10.1128/mmbr.00196-23. PubMed PMID: 38440970; PubMed Central PMCID: PMCPMC10966950.

66. Guerreiro MA, Springer DJ, Rodrigues JA, Rusche LN, Findley K, Heitman J, et al. Molecular and genetic evidence for a tetrapolar mating system in the basidiomycetous yeast *Kwoniella mangrovensis* and two novel sibling species. Eukaryot Cell. 2013;12(5):746-60. Epub 2013/03/26. doi: 10.1128/ec.00065-13. PubMed PMID: 23524993; PubMed Central PMCID: PMCPmc3647770.

67. Metin B, Findley K, Heitman J. The mating type locus (*MAT*) and sexual reproduction of *Cryptococcus heveanensis*: insights into the evolution of sex and sex-determining chromosomal regions in fungi. PLOS Genet. 2010;6(5):e1000961. Epub 2010/05/27. doi: 10.1371/journal.pgen.1000961. PubMed PMID: 20502678; PubMed Central PMCID: PMCPMC2873909.

68. Cheng T, Veselská T, Křížková B, Švec K, Havlíček V, Stadler M, et al. Insight into the genomes of dominant yeast symbionts of European spruce bark beetle, *Ips typographus*. Front Microbiol. 2023;14:1108975. Epub 20230403. doi: 10.3389/fmicb.2023.1108975. PubMed PMID: 37077248; PubMed Central PMCID: PMCPMC10106607.

69. Basson JR, Roets F, Wingfield MJ, Aylward J. Bark beetles and their associated fungi infesting native *Widdringtonia* species in the Western Cape province of South Africa. Afr Entomol. 2024;32:1-8.

70. Crous PW, Luangsa-Ard JJ, Wingfield MJ, Carnegie AJ, Hernandez-Restrepo M, Lombard L, et al. Fungal Planet description sheets: 785-867. Persoonia. 2018;41:238-417. Epub 2019/02/08. doi: 10.3767/persoonia.2018.41.12. PubMed PMID: 30728607; PubMed Central PMCID: PMCPMC6344811.

71. Li AH, Yuan FX, Groenewald M, Bensch K, Yurkov AM, Li K, et al. Diversity and phylogeny of basidiomycetous yeasts from plant leaves and soil: Proposal of two new orders, three new families, eight new genera and one hundred and seven new species. Stud Mycol. 2020;96:17-140. Epub 20200128. doi: 10.1016/j.simyco.2020.01.002. PubMed PMID: 32206137; PubMed Central PMCID: PMCPMC7082220.

72. Leufvén A, Bergström G, Falsen E. Interconversion of verbenols and verbenone by identified yeasts isolated from the spruce bark beetle *Ips typographus*. J Chem Ecol. 1984;10(9):1349-61. doi: 10.1007/BF00988116. PubMed PMID: 24317586.

73. Yurkov AM, Rohl O, Pontes A, Carvalho C, Maldonado C, Sampaio JP. Local climatic conditions constrain soil yeast diversity patterns in Mediterranean forests, woodlands and scrub biome. FEMS Yeast Res. 2016;16(1):fov103. doi: 10.1093/femsyr/fov103. PubMed PMID: 26568202.

74. Kwon-Chung KJ. A new genus, *Filobasidiella*, the perfect state of *Cryptococcus neoformans*. Mycologia. 1975;67:1197-200.

75. Kwon-Chung KJ. A new species of *Filobasidiella*, the sexual state of *Cryptococcus neoformans* B and C serotypes. Mycologia 1976;68:943-6.

76. Kwon-Chung KJ. Morphogenesis of *Filobasidiella neoformans*, the sexual state of *Cryptococcus neoformans*. Mycologia. 1976;68:821-33.

77. Rodriguez-Carres M, Findley K, Sun S, Dietrich FS, Heitman J. Morphological and genomic characterization of *Filobasidiella depauperata*: a homothallic sibling species of the pathogenic *Cryptococcus* species complex. PLOS ONE. 2010;5(3):e9620. doi: 10.1371/journal.pone.0009620.

78. Findley K, Sun S, Fraser JA, Hsueh Y-P, Averette AF, Li W, et al. Discovery of a modified tetrapolar sexual cycle in *Cryptococcus amylolentus* and the evolution of *MAT* in the *Cryptococcus* species complex. PLOS Genet. 2012;8(2):e1002528. doi: 10.1371/journal.pgen.1002528.

79. Sun S, Priest SJ, Heitman J. *Cryptococcus neoformans* mating and genetic crosses. Curr Protoc Microbiol. 2019:e75. Epub 2019/01/21. doi: 10.1002/cpmc.75. PubMed PMID: 30661293.

80. Raper J, Flexer A. Mating systems and evolution of the basidiomycetes. Evolution in the higher basidiomycetes. Knoxville, TN: University of Tennessee Press; 1971. p. 149-67.

81. Fraser JA, Hsueh Y-P, Findley KM, Heitman J. Evolution of the mating-type locus: the basidiomycetes. Sex in Fungi2007. p. 19-34.

82. Phadke SS, Feretzaki M, Clancey SA, Mueller O, Heitman J. Unisexual reproduction of *Cryptococcus gattii*. PLOS ONE. 2014;9(10):e111089. Epub 2014/10/23. doi: 10.1371/journal.pone.0111089. PubMed PMID: 25337713; PubMed Central PMCID: PMCPMC4206507.

83. Chang YC, Wickes BL, Miller GF, Penoyer LA, Kwon-Chung KJ. *Cryptococcus neoformans STE12*α regulates virulence but is not essential for mating. J Exp Med. 2000;191(5):871-82. doi: 10.1084/jem.191.5.871. PubMed PMID: 10704467; PubMed Central PMCID: PMCPMC2195848.

84. Yue C, Cavallo LM, Alspaugh JA, Wang P, Cox GM, Perfect JR, et al. The *STE12*α homolog is required for haploid filamentation but largely dispensable for mating and virulence in *Cryptococcus*

neoformans. Genetics. 1999;153(4):1601-15. doi: 10.1093/genetics/153.4.1601. PubMed PMID: 10581270; PubMed Central PMCID: PMCPMC1460866.

85. Burger F, Daugeron MC, Linder P. Dbp10p, a putative RNA helicase from *Saccharomyces cerevisiae*, is required for ribosome biogenesis. Nucleic Acids Res. 2000;28(12):2315-23. doi: 10.1093/nar/28.12.2315. PubMed PMID: 10871363; PubMed Central PMCID: PMCPMC102738.

86. Parnell KM, Bass BL. Functional redundancy of yeast proteins Reh1 and Rei1 in cytoplasmic 60S subunit maturation. Mol Cell Biol. 2009;29(14):4014-23. Epub 20090511. doi: 10.1128/MCB.01582-08. PubMed PMID: 19433447; PubMed Central PMCID: PMCPMC2704747.

87. Mizushima N, Noda T, Yoshimori T, Tanaka Y, Ishii T, George MD, et al. A protein conjugation system essential for autophagy. Nature. 1998;395(6700):395-8. doi: 10.1038/26506. PubMed PMID: 9759731.

88. Zhu YH, Hyun J, Pan YZ, Hopper JE, Rizo J, Wu JQ. Roles of the fission yeast UNC-13/Munc13 protein Ync13 in late stages of cytokinesis. Mol Biol Cell. 2018;29(19):2259-79. Epub 20180725. doi: 10.1091/mbc.E18-04-0225. PubMed PMID: 30044717; PubMed Central PMCID: PMCPMC6249806.

89. Wigge PA, Kilmartin JV. The Ndc80p complex from *Saccharomyces cerevisiae* contains conserved centromere components and has a function in chromosome segregation. J Cell Biol. 2001;152(2):349-60. doi: 10.1083/jcb.152.2.349. PubMed PMID: 11266451; PubMed Central PMCID: PMCPMC2199619.

90. Guterman A, Glickman MH. Complementary roles for Rpn11 and Ubp6 in deubiquitination and proteolysis by the proteasome. J Biol Chem. 2004;279(3):1729-38. Epub 20031027. doi: 10.1074/jbc.M307050200. PubMed PMID: 14581483.

91. Sridhar S, Hori T, Nakagawa R, Fukagawa T, Sanyal K. Bridgin connects the outer kinetochore to centromeric chromatin. Nat Commun. 2021;12(1):146. Epub 20210108. doi: 10.1038/s41467-020-20161-9. PubMed PMID: 33420015; PubMed Central PMCID: PMCPMC7794384.

92. Billmyre RB, Craig CJ, Lyon J, Reichardt C, Eickbush MT, Zanders SE. Saturation transposon mutagenesis enables genome-wide identification of genes required for growth and fluconazole resistance in the human fungal pathogen *Cryptococcus neoformans*. bioRxiv. 2024:2024.07.28.605507. doi: 10.1101/2024.07.28.605507.

93. Mancera E, Bourgon R, Brozzi A, Huber W, Steinmetz LM. High-resolution mapping of meiotic crossovers and non-crossovers in yeast. Nature. 2008;454(7203):479-85. Epub 2008/07/11. doi: 10.1038/nature07135. PubMed PMID: 18615017; PubMed Central PMCID: PMCPMC2780006.

94. Weber CC, Boussau B, Romiguier J, Jarvis ED, Ellegren H. Evidence for GC-biased gene conversion as a driver of between-lineage differences in avian base composition. Genome Biol. 2014;15(12):549. Epub 2014/12/17. doi: 10.1186/s13059-014-0549-1. PubMed PMID: 25496599; PubMed Central PMCID: PMCPMC4290106.

95. Desjardins CA, Giamberardino C, Sykes SM, Yu CH, Tenor JL, Chen Y, et al. Population genomics and the evolution of virulence in the fungal pathogen *Cryptococcus neoformans*. Genome Res. 2017;27(7):1207-19. Epub 2017/06/15. doi: 10.1101/gr.218727.116. PubMed PMID: 28611159; PubMed Central PMCID: PMCPMC5495072.

96. Lengeler KB, Wang P, Cox GM, Perfect JR, Heitman J. Identification of the *MAT***a** mating-type locus of *Cryptococcus neoformans* reveals a serotype A *MAT***a** strain thought to have been extinct. Proc Natl Acad Sci U S A. 2000;97(26):14455-60. doi: 10.1073/pnas.97.26.14455. PubMed PMID: 11121047; PubMed Central PMCID: PMCPMC18940.

97. Viviani MA, Esposto MC, Cogliati M, Montagna MT, Wickes BL. Isolation of a *Cryptococcus neoformans* serotype A *MAT***a** strain from the Italian environment. Med Mycol. 2001;39(5):383-6. doi: 10.1080/mmy.39.5.383.386. PubMed PMID: 12054047.

98. Viviani MA, Nikolova R, Esposto MC, Prinz G, Cogliati M. First European case of serotype A *MAT***a** *Cryptococcus neoformans* infection. Emerg Infect Dis. 2003;9(9):1179-80. doi: 10.3201/eid0909.020770. PubMed PMID: 14528882; PubMed Central PMCID: PMCPMC3016796.

99. Litvintseva AP, Marra RE, Nielsen K, Heitman J, Vilgalys R, Mitchell TG. Evidence of sexual recombination among *Cryptococcus neoformans* serotype A isolates in sub-Saharan Africa. Eukaryot Cell. 2003;2(6):1162-8. doi: 10.1128/EC.2.6.1162-1168.2003. PubMed PMID: 14665451; PubMed Central PMCID: PMCPMC326657.

100. Ashton PM, Thanh LT, Trieu PH, Van Anh D, Trinh NM, Beardsley J, et al. Three phylogenetic groups have driven the recent population expansion of *Cryptococcus neoformans*. Nat Commun. 2019;10(1):2035. Epub 20190502. doi: 10.1038/s41467-019-10092-5. PubMed PMID: 31048698; PubMed Central PMCID: PMCPMC6497710.

101. Yadav V, Sun S, Heitman J. Uniparental nuclear inheritance following bisexual mating in fungi. eLife. 2021;10. Epub 2021/08/03. doi: 10.7554/eLife.66234. PubMed PMID: 34338631; PubMed Central PMCID: PMCPMC8412948.

102. Hsueh YP, Idnurm A, Heitman J. Recombination hotspots flank the *Cryptococcus* mating-type locus: implications for the evolution of a fungal sex chromosome. PLOS Genet. 2006;2(11):e184. Epub 2006/11/07. doi: 10.1371/journal.pgen.0020184. PubMed PMID: 17083277; PubMed Central PMCID: PMCPMC1630710.

103. Loftus BJ, Fung E, Roncaglia P, Rowley D, Amedeo P, Bruno D, et al. The genome of the basidiomycetous yeast and human pathogen *Cryptococcus neoformans*. Science. 2005;307(5713):1321-4. Epub 2005/01/18. doi: 10.1126/science.1103773. PubMed PMID: 15653466; PubMed Central PMCID: PMCPMC3520129.

104. Huang J, Larmore CJ, Priest SJ, Xu Z, Dietrich FS, Yadav V, et al. Distinct evolutionary trajectories following loss of RNA interference in *Cryptococcus neoformans*. Proc Natl Acad Sci U S A. 2024;121(47):e2416656121. Epub 20241113. doi: 10.1073/pnas.2416656121. PubMed PMID: 39536081; PubMed Central PMCID: PMCPMC11588098.

105. Drillon G, Carbone A, Fischer G. SynChro: a fast and easy tool to reconstruct and visualize synteny blocks along eukaryotic chromosomes. PLOS ONE. 2014;9(3):e92621. Epub 2014/03/22. doi: 10.1371/journal.pone.0092621. PubMed PMID: 24651407; PubMed Central PMCID: PMCPMC3961402.

106. D'Souza CA, Kronstad JW, Taylor G, Warren R, Yuen M, Hu G, et al. Genome variation in *Cryptococcus gattii*, an emerging pathogen of immunocompetent hosts. MBio. 2011;2(1):e00342-10. Epub 2011/02/10. doi: 10.1128/mBio.00342-10. PubMed PMID: 21304167; PubMed Central PMCID: PMCPMC3037005.

107. Morrow CA, Lee IR, Chow EW, Ormerod KL, Goldinger A, Byrnes EJ, 3rd, et al. A unique chromosomal rearrangement in the *Cryptococcus neoformans* var. *grubii* type strain enhances key phenotypes associated with virulence. MBio. 2012;3(2). doi: 10.1128/mBio.00310-11. PubMed PMID: 22375073; PubMed Central PMCID: PMCPMC3302566.

108. Yadav V, Sun S, Coelho MA, Heitman J. Centromere scission drives chromosome shuffling and reproductive isolation. Proc Natl Acad Sci U S A. 2020;117(14):7917-28. Epub 2020/03/21. doi: 10.1073/pnas.1918659117. PubMed PMID: 32193338; PubMed Central PMCID: PMCPMC7149388.

109. Gomez-Zapata PA, Tellgren-Roth C, Samils B, Stenlid J, Kaitera J, Brandström Durling M, et al. Mating type gene divergence is associated with life cycle differentiation in scots pine blister rust. bioRxiv. 2025. doi: 10.1101/2025.05.02.651906.

110. Urban M, Kahmann R, Bolker M. The biallelic *a* mating type locus of *Ustilago maydis*: remnants of an additional pheromone gene indicate evolution from a multiallelic ancestor. Mol Gen Genet. 1996;250(4):414-20. Epub 1996/03/07. doi: 10.1007/BF02174029. PubMed PMID: 8602158.

111. Fedler M, Luh KS, Stelter K, Nieto-Jacobo F, Basse CW. The *a2* mating-type locus genes *lga2* and *rga2* direct uniparental mitochondrial DNA (mtDNA) inheritance and constrain mtDNA recombination during sexual development of *Ustilago maydis*. Genetics. 2009;181(3):847-60. Epub 2008/12/24. doi: 10.1534/genetics.108.096859. PubMed PMID: 19104076; PubMed Central PMCID: PMCPMC2651059.

112. Coelho MA, Gonçalves P, Sampaio JP. Evidence for maintenance of sex determinants but not of sexual stages in red yeasts, a group of early diverged basidiomycetes. BMC Evol Biol. 2011;11(1):249. doi: 10.1186/1471-2148-11-249.

113. Huang J, Hu P, Ye L, Shen Z, Chen X, Liu F, et al. Pan-drug resistance and hypervirulence in a human fungal pathogen are enabled by mutagenesis induced by mammalian body temperature. Nat Microbiol. 2024;9(7):1686-99. Epub 2024/06/20. doi: 10.1038/s41564-024-01720-y. PubMed PMID: 38898217.

114. Sperschneider J, Chen J, Anderson C, Morin E, Zhang X, Lewis D, et al. A chromosome-scale genome assembly of the flax rust fungus reveals the two unusually large effector proteins, AvrM3 and AvrN. Mol Plant Microbe Interact. 2025. Epub 20250528. doi: 10.1094/MPMI-04-25-0047-R. PubMed PMID: 40435161.

115. Jay P, Jeffries D, Hartmann FE, Veber A, Giraud T. Why do sex chromosomes progressively lose recombination? Trends Genet. 2024;40(7):564-79. Epub 2024/04/28. doi: 10.1016/j.tig.2024.03.005. PubMed PMID: 38677904.

116. Xu L, Petit E, Hood ME. Variation in mate-recognition pheromones of the fungal genus Microbotryum. Heredity (Edinb). 2016;116(1):44-51. Epub 2015/08/27. doi: 10.1038/hdy.2015.68. PubMed PMID: 26306729; PubMed Central PMCID: PMCPMC4675872.

117. Lucotte EA, Jay P, Rougemont Q, Boyer L, Cornille A, Snirc A, et al. Repeated loss of function at HD mating-type genes and of recombination in anther-smut fungi. Nat Commun. 2025;16(1):4962. Epub 2025/05/29. doi: 10.1038/s41467-025-60222-5. PubMed PMID: 40436846; PubMed Central PMCID: PMCPMC12119880.

118. Shen WC, Davidson RC, Cox GM, Heitman J. Pheromones stimulate mating and differentiation via paracrine and autocrine signaling in *Cryptococcus neoformans*. Eukaryot Cell. 2002;1(3):366-77. doi: 10.1128/EC.1.3.366-377.2002. PubMed PMID: 12455985; PubMed Central PMCID: PMCPMC118021.

119. Zahavi A. Mate selection-a selection for a handicap. J Theor Biol. 1975;53(1):205-14. doi: 10.1016/0022-5193(75)90111-3. PubMed PMID: 1195756.

120. Nieuwenhuis BP, Aanen DK. Sexual selection in fungi. J Evol Biol. 2012;25(12):2397-411. doi: 10.1111/jeb.12017. PubMed PMID: 23163326.

121. Jackson CL, Hartwell LH. Courtship in *S. cerevisiae*: both cell types choose mating partners by responding to the strongest pheromone signal. Cell. 1990;63(5):1039-51. doi: 10.1016/0092-8674(90)90507-b. PubMed PMID: 2257622.

122. Rogers DW, Greig D. Experimental evolution of a sexually selected display in yeast. Proc Biol Sci. 2009;276(1656):543-9. doi: 10.1098/rspb.2008.1146. PubMed PMID: 18842545; PubMed Central PMCID: PMCPMC2590883.

123. Jackson JA, Fink GR. Gene conversion between duplicated genetic elements in yeast. Nature. 1981;292(5821):306-11. Epub 1981/07/23. doi: 10.1038/292306a0. PubMed PMID: 6265790.

124. Szostak JW, Orr-Weaver TL, Rothstein RJ, Stahl FW. The double-strand-break repair model for recombination. Cell. 1983;33(1):25-35. Epub 1983/05/01. doi: 10.1016/0092-8674(83)90331-8. PubMed PMID: 6380756.

125. Hawley RS. The human Y chromosome: rumors of its death have been greatly exaggerated. Cell. 2003;113(7):825-8. doi: 10.1016/s0092-8674(03)00470-7. PubMed PMID: 12837241.

126. Rozen S, Skaletsky H, Marszalek JD, Minx PJ, Cordum HS, Waterston RH, et al. Abundant gene conversion between arms of palindromes in human and ape Y chromosomes. Nature. 2003;423(6942):873-6. doi: 10.1038/nature01723. PubMed PMID: 12815433.

127. Connallon T, Clark AG. Gene duplication, gene conversion and the evolution of the Y chromosome. Genetics. 2010;186(1):277-86. Epub 2010/06/17. doi: 10.1534/genetics.110.116756. PubMed PMID: 20551442; PubMed Central PMCID: PMCPMC2940292.

128. Corcoran P, Anderson JL, Jacobson DJ, Sun Y, Ni P, Lascoux M, et al. Introgression maintains the genetic integrity of the mating-type determining chromosome of the fungus *Neurospora tetrasperma*. Genome Res. 2016;26(4):486-98. Epub 2016/02/20. doi: 10.1101/gr.197244.115. PubMed PMID: 26893460; PubMed Central PMCID: PMCPMC4817772.

129. Janbon G, Ormerod KL, Paulet D, Byrnes EJ, 3rd, Yadav V, Chatterjee G, et al. Analysis of the genome and transcriptome of *Cryptococcus neoformans* var. *grubii* reveals complex RNA expression and microevolution leading to virulence attenuation. PLOS Genet. 2014;10(4):e1004261. Epub 2014/04/20. doi: 10.1371/journal.pgen.1004261. PubMed PMID: 24743168; PubMed Central PMCID: PMCPMC3990503.

130. Yadav V, Sun S, Billmyre RB, Thimmappa BC, Shea T, Lintner R, et al. RNAi is a critical determinant of centromere evolution in closely related fungi. Proc Natl Acad Sci U S A. 2018. Epub 2018/03/07. doi: 10.1073/pnas.1713725115. PubMed PMID: 29507212.

131. Priest SJ, Yadav V, Roth C, Dahlmann TA, Kück U, Magwene PM, et al. Uncontrolled transposition following RNAi loss causes hypermutation and antifungal drug resistance in clinical isolates of *Cryptococcus neoformans*. Nat Microbiol. 2022;7(8):1239-51. Epub 2022/08/03. doi: 10.1038/s41564-022-01183-z. PubMed PMID: 35918426.

132. Lemoine FJ, Degtyareva NP, Lobachev K, Petes TD. Chromosomal translocations in yeast induced by low levels of DNA polymerase a model for chromosome fragile sites. Cell. 2005;120(5):587-98. Epub 2005/03/16. doi: 10.1016/j.cell.2004.12.039. PubMed PMID: 15766523.

133. Byrnes EJ, 3rd, Li W, Ren P, Lewit Y, Voelz K, Fraser JA, et al. A diverse population of *Cryptococcus gattii* molecular type VGIII in southern Californian HIV/AIDS patients. PLOS Pathog. 2011;7(9):e1002205. Epub 2011/09/13. doi: 10.1371/journal.ppat.1002205. PubMed PMID: 21909264; PubMed Central PMCID: PMCPMC3164645.

134. Gostinčar C, Sun X, Zajc J, Fang C, Hou Y, Luo Y, et al. Population genomics of an obligately halophilic basidiomycete *Wallemia ichthyophaga*. Front Microbiol. 2019;10:2019. Epub 2019/09/26. doi: 10.3389/fmicb.2019.02019. PubMed PMID: 31551960; PubMed Central PMCID: PMCPMC6738226.

135. Lee N, Bakkeren G, Wong K, Sherwood JE, Kronstad JW. The mating-type and pathogenicity locus of the fungus *Ustilago hordei* spans a 500-kb region. Proc Natl Acad Sci U S A. 1999;96(26):15026-31. Epub 1999/12/28. doi: 10.1073/pnas.96.26.15026. PubMed PMID: 10611332; PubMed Central PMCID: PMCPMC24767.

136. Liang SW, Huang YH, Chiu JY, Tseng HW, Huang JH, Shen WC. The smut fungus *Ustilago esculenta* has a bipolar mating system with three idiomorphs larger than 500 kb. Fungal Genet Biol. 2019;126:61-74. Epub 2019/02/23. doi: 10.1016/j.fgb.2019.02.007. PubMed PMID: 30794950.

137. Sun Y, Svedberg J, Hiltunen M, Corcoran P, Johannesson H. Large-scale suppression of recombination predates genomic rearrangements in *Neurospora tetrasperma*. Nat Commun. 2017;8(1):1140. Epub 2017/10/28. doi: 10.1038/s41467-017-01317-6. PubMed PMID: 29074958; PubMed Central PMCID: PMCPMC5658415.

138. Heitman J, Sun S, James TY. Evolution of fungal sexual reproduction. Mycologia. 2013;105(1):1-27. Epub 2012/10/27. doi: 10.3852/12-253. PubMed PMID: 23099518; PubMed Central PMCID: PMCPMID: 23099518.

139. Hartmann FE, Rodriguez de la Vega RC, Carpentier F, Gladieux P, Cornille A, Hood ME, et al. Understanding adaptation, coevolution, host specialization, and mating system in castrating anther-smut fungi by combining population and comparative Genomics. Annu Rev Phytopathol. 2019;57:431-57. Epub 20190723. doi: 10.1146/annurev-phyto-082718-095947. PubMed PMID: 31337277.

140. Taylor JW, Hann-Soden C, Branco S, Sylvain I, Ellison CE. Clonal reproduction in fungi. Proc Natl Acad Sci U S A. 2015;112(29):8901-8. Epub 2015/07/22. doi: 10.1073/pnas.1503159112. PubMed PMID: 26195774; PubMed Central PMCID: PMCPMC4517272.

141. Koren S, Walenz BP, Berlin K, Miller JR, Bergman NH, Phillippy AM. Canu: scalable and accurate long-read assembly via adaptive k-mer weighting and repeat separation. Genome Res. 2017;27(5):722-36. Epub 2017/03/17. doi: 10.1101/gr.215087.116. PubMed PMID: 28298431; PubMed Central PMCID: PMCPMC5411767.

142. Walker BJ, Abeel T, Shea T, Priest M, Abouelliel A, Sakthikumar S, et al. Pilon: an integrated tool for comprehensive microbial variant detection and genome assembly improvement. PLOS ONE. 2014;9(11):e112963. Epub 2014/11/20. doi: 10.1371/journal.pone.0112963. PubMed PMID: 25409509; PubMed Central PMCID: PMCPMC4237348.

143. Li H, Durbin R. Fast and accurate short read alignment with Burrows-Wheeler transform. Bioinformatics. 2009;25(14):1754-60. Epub 2009/05/20. doi: 10.1093/bioinformatics/btp324. PubMed PMID: 19451168; PubMed Central PMCID: PMCPMC2705234.

144. Li H. Minimap2: pairwise alignment for nucleotide sequences. Bioinformatics. 2018;34(18):3094-100. Epub 2018/05/12. doi: 10.1093/bioinformatics/bty191. PubMed PMID: 29750242; PubMed Central PMCID: PMCPMC6137996.

145. Robinson JT, Thorvaldsdóttir H, Winckler W, Guttman M, Lander ES, Getz G, et al. Integrative genomics viewer. Nat Biotechnol. 2011;29(1):24-6. Epub 2011/01/12. doi: 10.1038/nbt.1754. PubMed PMID: 21221095; PubMed Central PMCID: PMCPMC3346182.

146. Gnerre S, Maccallum I, Przybylski D, Ribeiro FJ, Burton JN, Walker BJ, et al. High-quality draft assemblies of mammalian genomes from massively parallel sequence data. Proc Natl Acad Sci U S A. 2011;108(4):1513-8. Epub 2010/12/29. doi: 10.1073/pnas.1017351108. PubMed PMID: 21187386; PubMed Central PMCID: PMCPMC3029755.

147. Bruna T, Hoff KJ, Lomsadze A, Stanke M, Borodovsky M. BRAKER2: automatic eukaryotic genome annotation with GeneMark-EP+ and AUGUSTUS supported by a protein database. NAR Genom Bioinform. 2021;3(1):lqaa108. Epub 2021/02/13. doi: 10.1093/nargab/lqaa108. PubMed PMID: 33575650; PubMed Central PMCID: PMCPMC7787252.

148. Goodwin TJ, Poulter RT. The diversity of retrotransposons in the yeast *Cryptococcus neoformans*. Yeast. 2001;18(9):865-80. Epub 2001/06/28. doi: 10.1002/yea.733. PubMed PMID: 11427969.

149. Cantalapiedra CP, Hernandez-Plaza A, Letunic I, Bork P, Huerta-Cepas J. eggNOG-mapper v2: functional annotation, orthology assignments, and domain prediction at the metagenomic scale. Mol Biol Evol. 2021;38(12):5825-9. Epub 2021/10/02. doi: 10.1093/molbev/msab293. PubMed PMID: 34597405; PubMed Central PMCID: PMCPMC8662613.

150. Blin K, Shaw S, Kloosterman AM, Charlop-Powers Z, van Wezel GP, Medema MH, et al. antiSMASH 6.0: improving cluster detection and comparison capabilities. Nucleic Acids Res. 2021;49(W1):W29-W35. Epub 2021/05/13. doi: 10.1093/nar/gkab335. PubMed PMID: 33978755; PubMed Central PMCID: PMCPMC8262755.

151. Katoh K, Standley DM. MAFFT multiple sequence alignment software version 7: improvements in performance and usability. Mol Biol Evol. 2013;30(4):772-80. Epub 2013/01/19. doi: 10.1093/molbev/mst010. PubMed PMID: 23329690; PubMed Central PMCID: PMCPMC3603318.

152. Capella-Gutierrez S, Silla-Martinez JM, Gabaldon T. trimAl: a tool for automated alignment trimming in large-scale phylogenetic analyses. Bioinformatics. 2009;25(15):1972-3. Epub 2009/06/10. doi: 10.1093/bioinformatics/btp348. PubMed PMID: 19505945; PubMed Central PMCID: PMCPmc2712344.

153. Minh BQ, Schmidt HA, Chernomor O, Schrempf D, Woodhams MD, von Haeseler A, et al. IQ-TREE 2: new models and efficient methods for phylogenetic inference in the genomic era. Mol Biol Evol. 2020;37(5):1530-4. Epub 2020/02/06. doi: 10.1093/molbev/msaa015. PubMed PMID: 32011700; PubMed Central PMCID: PMCPMC7182206.

154. Zhang C, Rabiee M, Sayyari E, Mirarab S. ASTRAL-III: polynomial time species tree reconstruction from partially resolved gene trees. BMC Bioinformatics. 2018;19(Suppl 6):153. Epub 2018/05/11. doi:

10.1186/s12859-018-2129-y. PubMed PMID: 29745866; PubMed Central PMCID: PMCPMC5998893.

155. Chernomor O, von Haeseler A, Minh BQ. Terrace aware data structure for phylogenomic inference from supermatrices. Syst Biol. 2016;65(6):997-1008. Epub 2016/04/29. doi: 10.1093/sysbio/syw037. PubMed PMID: 27121966; PubMed Central PMCID: PMCPMC5066062.

156. Kalyaanamoorthy S, Minh BQ, Wong TKF, von Haeseler A, Jermiin LS. ModelFinder: fast model selection for accurate phylogenetic estimates. Nat Methods. 2017;14(6):587-9. Epub 2017/05/10. doi: 10.1038/nmeth.4285. PubMed PMID: 28481363; PubMed Central PMCID: PMCPMC5453245.

157. Hoang DT, Chernomor O, von Haeseler A, Minh BQ, Vinh LS. UFBoot2: improving the ultrafast bootstrap approximation. Mol Biol Evol. 2018;35(2):518-22. Epub 2017/10/28. doi: 10.1093/molbev/msx281. PubMed PMID: 29077904; PubMed Central PMCID: PMCPMC5850222.

158. Sullivan MJ, Petty NK, Beatson SA. Easyfig: a genome comparison visualizer. Bioinformatics. 2011;27(7):1009-10. Epub 2011/02/01. doi: 10.1093/bioinformatics/btr039. PubMed PMID: 21278367; PubMed Central PMCID: PMCPMC3065679.

159. Ianiri G, Fang YF, Dahlmann TA, Clancey SA, Janbon G, Kuck U, et al. Mating-type-specific ribosomal proteins control aspects of sexual reproduction in *Cryptococcus neoformans*. Genetics. 2020;214(3):635-49. Epub 2019/12/29. doi: 10.1534/genetics.119.302740. PubMed PMID: 31882399; PubMed Central PMCID: PMCPMC7054023.

160. Bian Z, Xu Z, Peer A, Choi Y, Priest SJ, Akritidou K, et al. Essential genes encoded by the mating-type locus of the human fungal pathogen *Cryptococcus neoformans*. bioRxiv. 2024. Epub 2024/12/16. doi: 10.1101/2024.12.02.626420. PubMed PMID: 39677606; PubMed Central PMCID: PMCPMC11642766.

161. Hershberg R, Petrov DA. General rules for optimal codon choice. PLOS Genet. 2009;5(7):e1000556. Epub 2009/07/14. doi: 10.1371/journal.pgen.1000556. PubMed PMID: 19593368; PubMed Central PMCID: PMCPMC2700274.

162. LaBella AL, Opulente DA, Steenwyk JL, Hittinger CT, Rokas A. Signatures of optimal codon usage in metabolic genes inform budding yeast ecology. PLOS Biol. 2021;19(4):e3001185. Epub 2021/04/20. doi: 10.1371/journal.pbio.3001185. PubMed PMID: 33872297; PubMed Central PMCID: PMCPMC8084343.

163. Wright F. The 'effective number of codons' used in a gene. Gene. 1990;87(1):23-9. Epub 1990/03/01. doi: 10.1016/0378-1119(90)90491-9. PubMed PMID: 2110097.

164. Cabanettes F, Klopp C. D-GENIES: dot plot large genomes in an interactive, efficient and simple way. PeerJ. 2018;6:e4958. Epub 2018/06/12. doi: 10.7717/peerj.4958. PubMed PMID: 29888139; PubMed Central PMCID: PMCPMC5991294.

165. Langdon QK, Peris D, Kyle B, Hittinger CT. sppIDer: A Species Identification Tool to Investigate Hybrid Genomes with High-Throughput Sequencing. Mol Biol Evol. 2018;35(11):2835-49. Epub 2018/09/06. doi: 10.1093/molbev/msy166. PubMed PMID: 30184140; PubMed Central PMCID: PMCPMC6231485.

166. Fu C, Heitman J. *PRM1* and *KAR5* function in cell-cell fusion and karyogamy to drive distinct bisexual and unisexual cycles in the *Cryptococcus pathogenic* species complex. PLOS Genet. 2017;13(11):e1007113. Epub 2017/11/28. doi: 10.1371/journal.pgen.1007113. PubMed PMID: 29176784; PubMed Central PMCID: PMCPMC5720818.

167. Priest SJ, Coelho MA, Mixao V, Clancey SA, Xu Y, Sun S, et al. Factors enforcing the species boundary between the human pathogens *Cryptococcus neoformans* and *Cryptococcus deneoformans*. PLOS Genet. 2021;17(1):e1008871. Epub 2021/01/20. doi: 10.1371/journal.pgen.1008871. PubMed PMID: 33465111; PubMed Central PMCID: PMCPMC7846113.

Figure legends

Fig 1. Phylogeny, breeding systems, and *MAT* loci organization in *Cryptococcus* and *Kwoniella*. (A) Maximum likelihood phylogeny of strains analyzed in this study, inferred from a concatenated data matrix comprising protein alignments of 3,086 single-copy genes. Clades are labeled as A–I, with clade E shown as a nested subclade within clade F for easier cross-referencing. Branch lengths are given as substitutions per site (scale bar). All branches are supported >95% by SH-aLTR and UFBoot tests unless otherwise indicated. Gene concordance factor (gCF) and site concordance factor (sCF) were assessed to evaluate genealogical concordance, revealing unresolved branching order of clades A, B, and C (dashed branches; see **S1 Fig** for details). A black asterisk denotes that VGV has not yet been associated with human infections, and a white asterisk marks strains sequenced solely with Illumina, yielding more fragmented assemblies. **(B)** Predicted breeding systems, *MAT* locus organization, and mating-type identity of the *P/R* locus. Breeding systems are classified as heterothallic or homothallic for species with defined sexual cycles, and as likely heterothallic for species inferred to exhibit heterothallism based on *MAT* gene content. **(C)** Heatmap of gene presence/absence and pseudogene annotations within inferred *MAT* loci. Genes are ordered by their frequency of presence across species, with the most conserved genes on the left. Genes marked as “unclear” indicate cases where presence within *MAT* is uncertain because locus boundaries could not be precisely determined. *BSP3* and *IKS1*, evicted from the *MAT* locus in *C. deneoformans* [34], are listed as absent in this species. Gene essentiality, as predicted or experimentally validated in strain H99 in prior studies rather than direct assessments in each species, is displayed at the bottom. Genes scored as absent from *MAT* may still be present elsewhere in the genome. **(D)** Gene presence frequency plot summarizing panel C. Pseudogenes were treated as present for frequency calculations, while unclear cases were treated as absent. The identification of either

1740 *SXI1* or *SXI2* was scored as "present" and combined for frequency quantification. **(E)** *MAT* loci
1741 locations in *Cryptococcus* sp. 3 (CWM60451), *K. fici*, and *K. europaea*, illustrating bipolar and
1742 pseudobipolar arrangements, respectively. Genes typically found either within or near the *HD* and
1743 *P/R* loci in tetrapolar species are designated as *HD*- and *P/R*-associated genes, and their
1744 respective chromosomal locations are indicated by gold or teal vertical bars. The data underlying
1745 this Figure can be found in **S1 Appendix** and at https://doi.org/10.5281/zenodo.16987438.
1746

1747 **Fig 2. Synteny analysis of the *P/R* locus in tetrapolar *Cryptococcus* and *Kwoniella* species.**
1748 **(A-B)** Detailed views of the *P/R* locus of representative *Cryptococcus* species from clades B and
1749 D. In both clades, the *P/R* locus exhibits lower GC content compared to other genomic regions. In
1750 clade D species, the predicted *P/R* locus contains only a subset of the genes found within the *P/R*
1751 locus of clade B species or the *MAT* locus of pathogenic *Cryptococcus* species. The additional
1752 genes in clade B or pathogenic species are instead located in the immediate downstream region,
1753 suggesting independent expansion of this genomic segment in clade D species. **(C-D)** *P/R* locus
1754 region in representative *Kwoniella* species of clades E and G. In *a2* strains, the *STE12* gene
1755 appears truncated. Remnants of the *NDC80* gene (in clade E/F species) or the *BSP3* gene (in
1756 clade G species) are observed at the right edge of the *P/R a2* allele, likely resulting from inversion
1757 events. In all panels, *P/R*-associated genes are colored teal if their orthologs in *Cryptococcus*
1758 pathogens are located within the *MAT* locus, with darker teal indicating genes positioned in the
1759 flanking regions, and bright green for genes present within the *P/R* locus of *C. amylolentus*, but
1760 absent in most *Cryptococcus* pathogens. The *P/R* allele of each strain (*a1* or *a2*) is indicated on
1761 the left. Chromosomes inverted relative to their original assembly orientations are marked with
1762 asterisks. GC content is depicted as the deviation from the genome average, calculated in 0.5 kb
1763 non-overlapping windows. Gene essentiality within and in the immediate vicinity of the *P/R* locus
1764 is inferred from predictions or experimental validations in *C. neoformans* H99 rather than direct
1765 assessments in these species. Other features are annotated as shown in the key. See **S4 Fig** for

1766 additional comparisons. The data underlying this Figure can be found at
1767 https://doi.org/10.5281/zenodo.16987438.
1768

1769 **Fig 3. The *P/R* locus in *K. ovata*, *K. endophytica*, and *K. dendrophila* likely arose through**
1770 **intra-*P/R* recombination**. **(A)** Synteny analysis comparing *P/R a1* and *P/R a2* alleles in select
1771 *Kwoniella* species from clade F. The *P/R* loci of *K. ovata* and *K. endophytica* contain *STE3***a** and
1772 *MF***a** alleles, along with truncated (ψ) versions of *STE3*α. Additionally, *K. ovata* harbors a truncated
1773 *MF*α gene. Synteny analysis indicates that the left side of the *P/R* locus in *K. ovata*, *K.*
1774 *endophytica*, and *K. dendrophila* is structurally more similar to *P/R a2* alleles of *K. pini* and *K.*
1775 *shivajii*, while the right side aligns more closely with the *P/R a1* alleles of *K. bestiolae* and *K.*
1776 *dejecticola*. **(B)** Gene genealogy of the *NDC80* gene inferred with IQ-TREE2 (model JTT+G4)
1777 showing trans-specific polymorphism across clade E/F species (labeled as 1) and within clade G
1778 species (labeled as 2). The *NDC80* alleles of *K. ovata*, *K. endophytica*, and *K. dendrophila* cluster
1779 more closely with *a1* alleles than with other *a2* alleles. The data underlying this Figure can be
1780 found at https://doi.org/10.5281/zenodo.16987438.
1781

1782 **Fig 4. Synteny analysis of the mating-type locus (*MAT*α and *MAT*a) across different**
1783 ***Cryptococcus neoformans* lineages. (A)** Phylogenetic tree of representative *C. neoformans*
1784 strains from different VN lineages, inferred using maximum likelihood analysis of a concatenated
1785 matrix of protein alignments from 5,439 single-copy genes. Branch support is based on SH-aLTR
1786 and UFBoot tests. Mating types were determined based on the allelic version of the pheromone
1787 receptor gene (*STE3*). **(B)** Synteny analysis of chr. 5, where the *MAT* locus resides, showing
1788 significant conservation across strains, except within the *MAT* and centromere regions, which
1789 exhibit rearrangements. Strains are organized by mating type and lineage, as in panel D. **(C)** Box
1790 plot comparing *MAT* locus size between α and **a** strains of *C. neoformans* (*C.n.*) and *C. gattii*

species complex (*C.g.c.*). The red dashed line, blue line, and boxes denote the mean value, median value, and interquartile range, respectively. Outliers are labeled with the corresponding strain name. Statistical significance (*P*-values) was determined by the Mann–Whitney U test. **(D)** Detailed synteny of the *MAT* locus, highlighting strain- and mating-type-specific rearrangements. The *MAT***a** configuration is more variable both across and within VN lineages, existing in three distinct configurations, whereas the *MAT*α structure is more conserved, with limited rearrangements between ancestrally linked homeodomain (*HD*) and pheromone receptor (*P/R*) genes. Observed rearrangements appear to result from inversions mediated by identical copies of pheromone genes. KDZ transposons are detected within the *MAT* locus of certain strains. Genes typically associated with the *P/R* and *HD* loci in tetrapolar species are colored green and gold, respectively, with darker shades denoting genes flanking the *MAT* locus in *Cryptococcus* pathogens. Gene essentiality within the *MAT* locus, as predicted or experimentally validated in strain H99, is indicated by color-coded circles as given in the key. The data underlying this Figure can be found at https://doi.org/10.5281/zenodo.16987438.

Fig 5. SNP distribution, phylogenetic analysis, and revised introgression model of the *MAT*a allele from VNBI into VNI. **(A)** Genome-wide distribution of SNPs across chromosome 5 in *C. neoformans MAT***a** strains from different VN lineages relative to the *C. neoformans* Ftc555-1 VNBI genome reference. Empty spaces in the plots represent either sites identical to the reference genome (monomorphic sites) or regions excluded due to low coverage or repetitive/duplicated sequences. Strains on the y-axis are ordered by the total number of SNPs across the genome, with a color gradient (right) indicating SNP counts: darker colors represent higher SNP densities relative to the reference (strains positioned at the top), while lighter colors indicate fewer SNPs (strains at the bottom). Reads from the reference strain were also mapped as a control. The x-axis shows genomic coordinates. **(B)** Zoomed-in view of the *MAT* locus region plus 50 kb flanking regions, with genes and other features represented as in Fig 4. Notably, VNI strains exhibit a

1817 markedly lower number of SNPs at the *MAT***a** locus relative to the VNBI reference, compared to
1818 VNBII strains. **(C)** Midpoint-rooted tree based on genome-wide SNPs across all chromosomes,
1819 illustrating the evolutionary relationships of the strains. **(D)** Midpoint-rooted tree constructed using
1820 SNPs from chromosome 5 only, showing similar relationships to the genome-wide analysis. **(E)**
1821 Midpoint-rooted tree based on SNPs restricted to the *MAT* locus, highlighting a closer relationship
1822 between VNI and VNBI strains. In all trees, branches are shown as the number of substitutions
1823 per site (scale bars) and have >95% support based on SH-aLTR and UFBoot tests, unless
1824 otherwise indicated. "Ref" represents the reference genome assembly employed for read mapping
1825 and is thus identical to Ftc555-1 reads, serving as a control to validate the SNP calling pipeline.
1826 **(F)** Proposed model for the introgression of the VNBI *MAT***a** allele into VNI, shown alongside the
1827 key stages of the *C. neoformans* sexual cycle (right). Step 1: possible loss of the *MAT***a** allele in
1828 the VNI lineage, likely due to a bottleneck; step 2: mating and cell-cell fusion between a VNBI
1829 (*MAT***a**) and a VNI (*MAT*α) strain; step 3: formation of dikaryotic hyphae, nuclear fusion, meiosis,
1830 recombination, and sporulation; step 4: some of the resulting F1 progeny emerged with a ~50:50
1831 VNBI:VNI genome composition, retaining the VNBI *MAT***a** locus; step 5: repeated backcrossing of
1832 the *MAT***a** F1 progeny to VNI *MAT*α strains progressively purging VNBI genomic regions while
1833 retaining the introgressed *MAT***a** allele; step 6: after ~10 backcrosses, the genome became
1834 ~99.95% VNI, with only the VNBI *MAT***a** locus and possibly a small fraction (~0.05%) of the VNBI
1835 genome remaining; step 7: over time, the introgressed VNBI *MAT***a** locus diverged and underwent
1836 rearrangements within the VNI background, reflecting strain-specific changes. The data
1837 underlying this Figure can be found at https://doi.org/10.5281/zenodo.16987438.
1838

1839 **Fig 6. Transition to linked *P/R-HD* loci in *Cryptococcus* sp. 3 (CMW60451) and**
1840 ***Cryptococcus* pathogens. (A)** The karyotype of *K. shandongensis* (with 14 chrs.) served as the
1841 reference for reconstructing synteny blocks in pairwise comparisons. For simplicity, only synteny
1842 blocks corresponding to *P/R*- and *HD*-containing chromosomes (chrs. 12 and 5, colored teal and

1843 gold, respectively) were plotted in representative *Cryptococcus* species of clades A (*C. neo.* H99),
1844 B (*C. amy.* CBS6039), C (*C.* sp. CMW60451), and D (*C. sp.* DSM108351). Besides the *MAT*-
1845 containing chromosomes, synteny blocks of two additional chromosomes in *K. shandongensis*
1846 (chrs. 10 and 14), which correspond to a large portion of *P/R* and *HD* chromosomes in *C.*
1847 *amylolentus* were also plotted (color-coded light blue and green, respectively). Other synteny
1848 blocks can be visualized in **S9A Fig**. A red arrowhead pinpoints the predicted location of an
1849 inactivated centromere (ic) in *Cryptococcus* sp. CMW60451. **(B)** Linear chromosome plots
1850 depicting gene synteny conservation across species with zoomed-in views depicted in **(C)**. In
1851 panel B, the *MAT* chromosome of bipolar species (*C. neoformans* and *C.* sp. 3, CMW60451) is
1852 shown twice: the left column depicts synteny relative to the *P/R*-containing chromosomes of
1853 tetrapolar species, and the right column depicts synteny relative to the *HD*-containing
1854 chromosomes.

1855

1856 **Fig 7. Hypothesized mechanisms underlying the tetrapolar-to-bipolar transitions in**
1857 ***Cryptococcus* sp. 3 and in *Cryptococcus* pathogens.** Comparative synteny analysis between
1858 *K. shandongensis* and **(A)** *Cryptococcus* sp. 3 or **(B)** *C. neoformans*, illustrating the inferred
1859 sequence of chromosomal rearrangements leading to this transition. In both panels, the left side
1860 displays pairwise alignments, with syntenic regions connected by red (collinear) and gray
1861 (inverted) links, while the right side depicts a stepwise model of the proposed structural changes.
1862 The transition likely began with (1) an initial chromosomal break and reciprocal translocation (red
1863 dashed line), leading to (2) the repositioning of the *P/R* locus onto the same chromosome as the
1864 *HD* locus. (3) In *Cryptococcus* sp. 3, a subsequent inversion relocated the *HD* locus closer to the
1865 presumed ancestral position of the *P/R* locus, whereas in *Cryptococcus* pathogens, an inversion
1866 instead shifted the *P/R* locus toward the original location of the *HD* locus. (4) Additional structural
1867 modifications further refined the newly linked configuration, ultimately resulting in (5) the extant
1868 *MAT* locus organization observed in each species. These models suggest that despite

independent evolutionary trajectories, both lineages underwent convergent genomic rearrangements that facilitated the transition to bipolar mating systems.

Fig 8. Linkage of *P/R* and *HD* loci in *Kwoniella fici* and *MAT* locus structure. (A) The karyotype of *K. shandongensis* (with 14 chrs.) served as a reference for reconstructing synteny blocks in pairwise comparisons with *Kwoniella* sp. 4 and *K. fici*. **(B)** Phylogenetic relationships among selected *Kwoniella* species, highlighting their *MAT* locus organization and inferred breeding systems. **(C)** Synteny comparison between *K. fici* and its closest relative *Kwoniella* sp. 4, illustrating chromosomal rearrangements underlying the linkage of *P/R* and *HD* loci in *K. fici*. A red double-headed arrow indicates that the centromere-proximal regions of chr. 2 in *Kwoniella* sp. 4 correspond to a region near the fusion point on the *K. fici* "giant" chromosome (chr. 1), whereas the telomere-proximal regions of *Kwoniella* sp. 4 chr. 2 align with more internalized regions. This suggests that a large pericentric inversion targeting the centromere-adjacent region is associated with this fusion event, as previously reported for other *Kwoniella* species [49]. **(D)** Detailed gene-level organization of the *MAT* locus in *K. fici* compared to *Kwoniella* sp. 4. Each track (labeled a–d in dark circles) corresponds to a specific region marked by a black bar in panel C. Chromosomes inverted relative to their original assembly orientations are marked with asterisks.

Fig 9. Sexual reproduction and recombination in *Kwoniella mangrovensis*. (A) Synteny analysis of the *P/R* and *HD* loci among three *K. mangrovensis* strains of different mating types (CBS8507, *a1b1*; CBS8886, *a2b1*; and CBS10435, *a2b2*). Note the pronounced divergence in the N-terminal domains of both *HD1* (*SXI1*) and *HD2* (*SXI2*) gene products, which are known to mediate mating-type specificity in other basidiomycetes. **(B)** Micrographs showing hyphal filaments extending from colony peripheries in a sexual cross between CBS8507 and CBS10435 after 2 weeks of incubation on CMA and V8 pH 5 media, in the dark, at room temperature. Insets depict two types of basidia: globose (a–c) and lageniform (b–d). Black arrows indicate clusters of

cells emerging near basidia (either at the surface or embedded), scored as potential meiotic progeny (basidiospores). Single cells from these clusters were isolated using a micromanipulator, cultured into colonies, and genotyped by PCR-RFLP (see S5 Appendix). Putative recombinants were further analyzed using Illumina sequencing. Scale bars = 100 μm (25 μm in insets). **(C)** Genotypic analysis of selected meiotic progeny. SNP density between the parental strains was calculated as the number of SNPs per 10 kb (top). The genotypes of 9 segregants, derived from four distinct cell clusters, were inferred from SNP data and are depicted as follows: orange for regions inherited from CBS8507, purple for regions inherited from CBS10435, and brown for heterozygous regions (i.e., inherited from both parents). Instances of recombination or loss of heterozygosity (LOH) are detected by changes in genotype along the chromosomes. Discrepancies in ploidy, as inferred from FACS and sequencing read coverage, suggest potential genomic instability (marked by asterisks). Mating-type identity was inferred through sequencing, coverage analysis, and FACS. **(D)** Sequencing coverage plot for progeny MP59 with color-coded contributions from each parent. Haplotype blocks inferred from SNP data are overlaid for each chromosome for comparison (additional progeny data is presented in S8 Fig). **(E)** Self-filamentation phenotype of *K. mangrovensis* progeny. Parental strains CBS8507 and CBS10435 (grown individually and in co-culture) and their recovered progeny were cultivated on CMA at room temperature. Self-filamentation was assessed after 2 weeks of incubation. While neither parental strain exhibited self-filamentation in solo culture, their co-culture produced hyphal filaments and basidia. Progeny MP16, MP18, and MP54 also exhibited robust self-filamentation on both CMA and V8 pH 5 (see **S9 Fig**), whereas progeny MP49, MP51, and MP59 displayed weaker filamentous growth, detectable only on V8 pH 5 (S9 Fig). Scale bars = 200 μm. **(F)** Summary of the growth phenotype of the recovered progeny. The production of mycelium and basidia was classified as: extensive (+++), when observed across the entire periphery of the mating patch; moderate (++), when restricted to specific areas of the mating patch; poor (+), when limited to a

single spot of the mating patch and slower to develop; and negative (–), when no filamentous growth was observed. Results represent observations from two independent tests.

Fig 10. Summary of the evolutionary transitions in *MAT* locus organization across *Kwoniella* and *Cryptococcus* species. Schematic representation of key chromosomal rearrangements and evolutionary events underlying transitions from tetrapolar to bipolar and pseudobipolar mating configurations. The phylogenetic tree highlights inferred changes in *MAT* locus structure, with color-coded branches representing both extant and reconstructed *MAT* configurations. Dashed lines indicate unresolved phylogenetic relationships among clades A, B, and C. Insets summarize distinct evolutionary stages, including: the ancestral organization with unlinked and compact *P/R* and *HD* loci (1); small-scale expansion of the *P/R* locus in *Kwoniella* (2); two independent large-scale expansions of the *P/R* locus in *Cryptococcus* (5); relocation of *P/R* and *HD* loci onto the same chromosome in *Kwoniella* resulting in either pseudobipolar (3) or fused (4) *MAT* configurations; and independent *HD-P/R* fusion events with *HD* gene loss in *Cryptococcus* pathogens and *Cryptococcus* sp. 3 (6). These transitions illustrate the diverse pathways by which chromosomal rearrangements (CRs) have shaped *MAT* locus architecture in these fungal lineages.

Supporting information

S1 Fig. *Cryptococcus* and *Kwoniella* species phylogenies. Both trees were inferred using a dataset of 3,086 single-copy genes shared across all species and three outgroups (depicted in grey). **(A)** Phylogeny inferred using a concatenation-based approach, corresponding to the tree in Fig 1A, but with all branch support and concordance values displayed (SH-aLRT, UFBoot, gCF, and sCF). **(B)** Tree topology inferred using a coalescence-based approach (ASTRAL), with local posterior probability (LPP) values shown for each branch. Quartet values for the main topology (q1) and alternative topologies (q2 and q3) are included for branches where q1 < 0.4, reflecting some uncertainty considering the expected value of 0.33 for a hard polytomy.

S2 Fig. Assessing sexual reproduction assays in *Cryptococcus* species. All micrographs are from cultures incubated for 2 weeks in the dark at room temperature on the indicated media. For each panel, the left image shows the colony edge, and the right image shows a higher-magnification view of cell or hyphal morphology from the same culture. **(A)** *C. decagattii*: solo cultures of strains 7685027 (*MAT*α) and CBS11687 (*MAT***a**) produced only yeast cells (right panels). In contrast, the α × **a** cross generated hyphae at the colony margin, with basidia and a few elongated basidiospores (arrowheads). Long spore chains were not observed, possibly due to rapid spore discharge. **(B)** *C. tetragattii*: solo cultures of strains IND107 (*MAT*α) and CBS11718 (*MAT***a**) produced only yeast cells (right panels), and the α × **a** cross did not form hyphae or sexual structures, even after prolonged incubation (>1 month). **(C)** Solo cultures of *Cryptococcus* sp. 3 (CMW60451) and *C. depauperatus* (CBS7841) on YPD and V8 pH 5 media. *C. depauperatus* produced abundant hyphae on both media; however, basidia (arrowhead) and spore chains (brackets) were only observed under V8 conditions. In contrast, *Cryptococcus* sp. 3 grew primarily as yeast on YPD, occasionally forming pseudohyphae on V8 pH 5, but no sexual

1970 structures were detected even after extended incubation (>1 month). **(D)** *Cryptococcus* sp. 4:
1971 solo cultures of NCYC1536 (*a1b1*) and DSM108351 (*a2b2*) grew as yeast (right panels). The
1972 *a1b1* × *a2b2* cross produced limited hyphae (right panel, zoomed view), but these were incipient
1973 and non-recurrent, and no sexual structures were observed even after >2 months. Scale bars:
1974 200 μm (colony edge images); 10 μm (right panels), except for panel D bottom right = 25 μm.
1975

1976 **S3 Fig. Structure and genomic context of the *HD* mating-type locus in tetrapolar**
1977 ***Cryptococcus* and *Kwoniella* species.** This supplementary figure spans five pages and contains
1978 a total of 15 panels (labeled A–O), with three consecutive panels per page. For each group of
1979 three panels, the top-left panel shows a synteny view of the full chromosomes, highlighting the
1980 chromosomal location of the *HD* locus; the bottom panel provides a zoomed-in synteny view (~200
1981 kb) centered on the *HD* locus; and the top-right panel displays a simplified phylogenetic tree,
1982 providing contextual information for the species included in the synteny analyses. For cross-
1983 referencing, *HD*-associated genes in the zoomed-in panel are colored gold if the corresponding
1984 ortholog in *Cryptococcus* pathogens is located within the *MAT* locus or shown in a darker shade
1985 when positioned in the immediate flanking regions. The *P/R* allele of each strain (*a1* or *a2*) is
1986 indicated on the left. Chromosomes inverted relative to their original assembly orientations are
1987 marked with asterisks. In panel G, only one representative of *K. europaea* and *K. botswanensis* is
1988 shown, and in panel M, only one representative of *K. heveanensis* is included, as the genomes of
1989 their mating-type counterparts are not assembled at the chromosome level; the scaffolds
1990 containing the *HD* locus are, however, included in the zoomed-in view. Other features are
1991 annotated as shown in the key.
1992

1993 **S4 Fig. Structure and genomic context of the *P/R* mating-type locus in tetrapolar**
1994 ***Cryptococcus* and *Kwoniella* species.** This supplementary figure spans five pages and contains
1995 a total of 15 panels (labeled A–O), with three consecutive panels per page. For each group of

1996 three panels, the top-left panel shows a synteny view of the full chromosomes, highlighting the
1997 chromosomal location of the *P/R* locus; the bottom panel provides a zoomed-in synteny view
1998 (~200 kb) that includes the full *P/R* locus; and the top-right panel displays a simplified phylogenetic
1999 tree, providing contextual information for the species included in the synteny analyses. For cross-
2000 referencing, *P/R*-associated genes in the zoomed-in panel are colored teal if the corresponding
2001 ortholog in *Cryptococcus* pathogens is located within the *MAT* locus, shown in a darker shade
2002 when positioned in the flanking regions, or colored bright green if the gene is found within the *P/R*
2003 locus of some species. The *P/R* allele of each strain (*a1* or *a2*) is indicated on the left.
2004 Chromosomes inverted relative to their original assembly orientations are marked with asterisks.
2005 In panels A and D, the GC content is depicted as the deviation from the genome average,
2006 calculated in 0.5 kb non-overlapping windows. In panel G, only one representative of *K. europaea*
2007 and *K. botswanensis* is shown, and in panel M, only one representative of *K. heveanensis* is
2008 included, as the genomes of their mating-type counterparts are not assembled at the chromosome
2009 level; the scaffolds containing the *P/R* locus are, however, included in the zoomed-in view. Other
2010 features are annotated as shown in the key.

2011

2012 **S5 Fig. Predicted rearrangements leading to the extant *P/R* configuration in *Kwoniella***
2013 **species within clades E/F and clade G. (A)** The extant *P/R* locus configuration in *K.*
2014 *mangrovensis* is inferred to derive from a putative ancestral state through three inversion events:
2015 (INV1) involving *STE3* and *STE12*, truncating *STE12* in the *a2* allele; (INV2) relocating *DBP10*
2016 and *REI1* from the locus edge to its center; and (INV3) moving *NDC80* from the edge to the middle
2017 of the locus. **(B)** The extant *P/R* locus configuration in *K. heveanensis*, inferred from a putative
2018 ancestral state involving four inversion events: (INV1) involving *STE3* and *STE12*, truncating
2019 *STE12* in the a2 allele; (INV1b) inverting only the pheromone gene; (INV2) relocating *DBP10* and
2020 *REI1* from the locus edge to its center; (INV3) relocating *BSP3-NDC80* to the middle of the locus;
2021 and (INV4) relocating *UBP6* to the center of the locus. INV1 and INV2 are likely ancestral in

2022 *Kwoniella*. **(C)** Gene genealogies reveal trans-specific polymorphism for *ATG7*, *UBP6*, and *BSP3*
2023 within clade G species only. Genes that required manual correction are marked with an asterisk.
2024
2025 **S6 Fig. *MAT* locus structure in *Cryptococcus deneoformans*.** Synteny analysis is shown for
2026 five strains organized by mating type. Strain JEC20**a** is an F1 progeny of the cross between
2027 isolates NIH12α and NIH433**a**, while JEC21α is its congenic partner, generated through 10 rounds
2028 of backcrossing to JEC20**a**. Therefore, the *MAT*α allele in JEC21α was inherited from NIH12α,
2029 and the *MAT***a** allele in JEC20**a** was inherited from NIH433**a**. The genes *BSP3* and *IKS1* are no
2030 longer part of the *MAT* locus in this species. Chromosomes inverted relative to their original
2031 assembly orientations are marked with asterisks.
2032
2033 **S7 Fig. *MAT* locus structure in *Cryptococcus gattii* species complex.** This supplementary
2034 figure spans 2 pages. **(A)** Synteny analysis with strains organized by mating type and, within each
2035 mating type, sorted according to their phylogenetic relationships. The analysis shows that the
2036 *MAT***a** configuration is highly variable across species, with each species exhibiting a distinct
2037 organization. In contrast, the *MAT*α structure is more conserved across species. **(B)** Synteny
2038 analysis with strains grouped by species to compare differences between mating types and define
2039 the exact boundaries of the *MAT* locus based on synteny conservation. Note that no *MAT***a** strain
2040 of the VGV lineage has been isolated to date. In both panels, chromosomes inverted relative to
2041 their original assembly orientations are marked with asterisks.
2042
2043 **S8 Fig. Phylogenies of *BSP3*, *PRT1*, *SPO14*, and *CAP1* within the predicted *MAT* locus of**
2044 ***Cryptococcus* sp. 3.** In pathogenic *Cryptococcus* species, these genes exhibit trans-specific
2045 polymorphism, characterized by mating-type-specific clustering, with **a** and α alleles forming
2046 distinct clades. An exception is observed in *BSP3* from *C. deneoformans* (marked with asterisks),

where mating-type specificity has been lost, representing a derived state. In contrast, protein sequences from *Cryptococcus* sp. 3 (highlighted in bold) do not group with either the **a** or α allele-specific clusters and instead occupy distinct positions outside these groups. Maximum likelihood phylogenies were constructed using protein sequences. For clarity, sequences from other *Cryptococcus* and *Kwoniella* species are collapsed, and well-supported nodes (≥90% SH-aLRT/UFBoot support) are indicated by filled circles. Scale bars represent the number of substitutions per site.

S9 Fig. Chromosome number reduction in *Cryptococcus* sp. 3 (CWM60451) involves centromere inactivation via loss of LTR-rich regions. (A) The karyotype of *K. shandongensis* (with 14 chrs.) served as the reference for reconstructing synteny blocks in pairwise comparisons with representative *Cryptococcus* species of clades A (*C. neoformans* H99), B (*C. amylolentus* CBS6039), C (*Cryptococcus* sp. CMW60451), and D (*Cryptococcus* sp. DSM108351). Each *K. shandongensis* chromosome is assigned a distinct color, which defines the color scheme for homologous synteny blocks in the corresponding chromosomes of other species. Centromeres are labeled "*CEN*" and colored according to their associated reference chromosome. Centromeres inferred to result from intercentromeric recombination are shown with two colors, reflecting ancestry from two distinct *K. shandongensis* centromeres. Inactivated centromeres ("*iCEN*" or "ic") are marked with red arrowheads. **(B)** Linear chromosome plots show synteny conservation among these species and detail the region of centromere inactivation (*iCEN*) in *Cryptococcus* sp. 3. Centromeres are marked with black boxes with white circles and repeat-rich regions are highlighted in pink.

S10 Fig. Nuclear genome composition of *K. mangrovensis* progeny reveals substantial aneuploidy and recombination. Sequencing read-depth coverage and inheritance patterns of progeny derived from a CBS8507 (*a1b1*) x CBS10435 (*a2b2*) sexual cross. For each progeny,

2073 sequencing coverage plots (normalized to the genome-wide average coverage) are color-coded
2074 according to each parent contribution, as shown in the key. Haplotypes blocks inferred from SNP
2075 data are overlaid for each chromosome for comparison, reflecting instances of recombination or
2076 loss of heterozygosity (LOH). In some strains (MP18, MP50, MP59 and MP54), coverage analysis
2077 suggests potential changes in ploidy in a subset of the sequenced cell population. This is indicated
2078 by skewed read proportions favoring one parent genome over the other while still retaining the
2079 corresponding haplotype, suggestive of genomic instability.
2080
2081 **S11 Fig. FACS analysis of *K. mangrovensis* parental strains CBS8507 and CBS10435, and**
2082 **their progeny.** The *C. neoformans* strain JEC21 and XL143 served as haploid (1n), and diploid
2083 (2n) controls, respectively.
2084
2085 **S12 Fig. Self-filamentation phenotype of *K. mangrovensis* progeny**. Parental strains
2086 CBS8507 and CBS10435 (grown individually and in co-culture) and their recovered progeny were
2087 cultivated on V8, pH 5.0 at room temperature. Self-filamentation was assessed after 2 weeks of
2088 incubation. While neither parental strain exhibited self-filamentation in solo culture, their co-culture
2089 produced hyphal filaments and basidia.
2090
2091 **S1 Text. GC depletion at the *P/R* locus in tetrapolar Cryptococcus is best explained by**
2092 **reduced GC-biased gene conversion**
2093
2094 **S2 Text. Karyotype reduction in *Cryptococcus* sp. 3 is independent of *P/R–HD* linkage.**
2095
2096 **S1 Appendix**. **Genome assembly, genomic features, and information on raw sequencing**
2097 **data generated in this study.** (A) List of *Cryptococcus* and *Kwoniella* isolates used in this study
2098 and summary of genome assembly statistics and other genomic features. (B) Genome

sequencing, assembly, and polishing approaches. (C) NCBI accession numbers of each genome and raw read data generated and used in this study. (D) SRA accession numbers of Illumina read data of *C. neoformans MAT***a** strains used for variant calling and SNP distribution. (E) Contig length, centromere coordinates, and telomeric sequences of genome assemblies generated and analyzed in this study.

S2 Appendix. **Mating-type (*MAT*) loci regions and genes within *MAT* in *Cryptococcus* and *Kwoniella*.** (A) Summary of the *MAT* loci regions in bipolar and tetrapolar *Cryptococcus* and *Kwoniella* species. (B) List of genes within the *P/R* locus in tetrapolar *Cryptococcus* and *Kwoniella* species and within *MAT* in bipolar species and their essentiality classification. (C) *P/R* locus size comparisons between tetrapolar *Cryptococcus* and *Kwoniella* species. (D) *P/R* locus size comparisons between tetrapolar *Cryptococcus* species. (E) *MAT* locus size comparisons between *MAT*α and *MAT***a** strains of *C. neoformans*. (F) *MAT* locus size comparisons between *MAT*α and *MAT***a** strains of the *C. gattii* species complex.

S3 Appendix. **Shared and unique mating-type (*MAT*) genes across *Cryptococcus* and *Kwoniella* clades.** (A) List of genes within *MAT* across *Cryptococcus* and *Kwoniella* species and clades. (B) Shared and unique genes within *P/R* locus in *Cryptococcus* and *Kwoniella* clades. (C) Shared and unique genes within *MAT* loci (i.e., including *P/R*- and *HD*-associated genes) in *Cryptococcus* and *Kwoniella* clades.

S4 Appendix. **GC content and codon composition/usage analysis.** (A) Genome-wide GC content and deviation from genome mean in clade B and D strains included in Fig 2. (B) GC content reduction in the *P/R* locus relative to genome-wide background (clades C and D). (C) Neutral comparison of non-coding GC in *P/R* locus vs. chromosome-matched background windows (Test 1). (D) Third-position codon usage (AT3 vs. GC3) in *P/R* locus vs. background (Test

2). (E) Codon usage and bias metrics in *P/R* vs. matched background genes (Tests 2 & 3). (F) Statistical tests for codon usage bias in *P/R* vs. background (Tests 3 & 4). (G) Tests for reduced codon adaptation (CAI) after controlling for GC3 and gene length (Test 4).

S5 Appendix. **List of Primers and PCR-RFLP analysis of *K. mangrovensis* sexual progeny.** (A) List of primers and conditions used to perform PCR-RFLP. (B) List of F1 progeny recovered from CBS8507 x CBS10435 cross and selected for Illumina sequencing after PCR-RFLP analysis. (C) List of all F1 progeny recovered from CBS8507 x CBS10435 cross. (D) PCR-RFLP results for amplicon MP293-MP294 digested with EcoRV. (E) PCR-RFLP results for amplicon MP303-MP304 digested with EcoRV. (F) PCR-RFLP results for amplicon MP307-MP308 digested with EcoRV. (G) PCR-RFLP results for amplicon MP309-MP310 digested with EcoRV. (H) PCR-RFLP results for amplicon MP311-MP312 digested with EcoRI. (I) PCR-RFLP results for amplicon MP313-MP314 digested with ClaI.

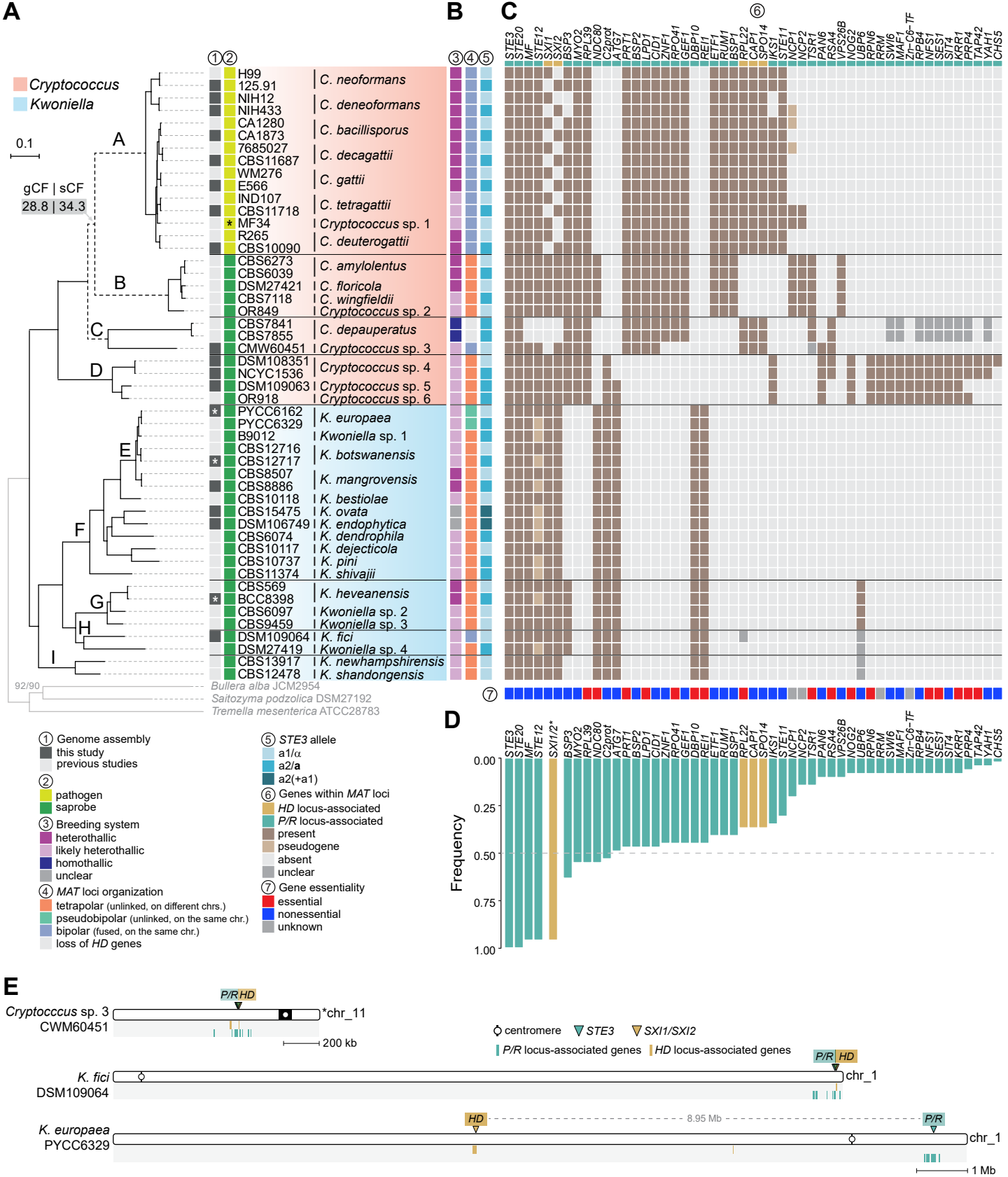

A
B
C
D
E
Cryptococcus
Kwoniella
0.1
gCF | sCF
28.8 | 34.3
H99
125.91
NIH12
NIH433
CA1280
CA1873
7685027
CBS11687
WM276
E566
IND107
CBS11718
MF34
R265
CBS10090
CBS6273
CBS6039
DSM27421
CBS7118
OR849
CBS7841
CBS7855
CMW60451
DSM108351
NCYC1536
DSM109063
OR918
PYCC6162
PYCC6329
B9012
CBS12716
CBS12717
CBS8507
CBS8886
CBS10118
CBS15475
DSM106749
CBS6074
CBS10117
CBS10737
CBS11374
CBS569
BCC8398
CBS6097
CBS9459
DSM109064
DSM27419
CBS13917
CBS12478
C. neoformans
C. deneoformans
C. bacillisporus
C. decagattii
C. gattii
C. tetragattii
Cryptococcus sp. 1
C. deuterogattii
C. amylolentus
C. floricola
C. wingfieldii
Cryptococcus sp. 2
C. depauperatus
Cryptococcus sp. 3
Cryptococcus sp. 4
Cryptococcus sp. 5
Cryptococcus sp. 6
K. europaea
Kwoniella sp. 1
K. botswanensis
K. mangrovensis
K. bestiolae
K. ovata
K. endophytica
K. dendrophila
K. dejecticola
K. pini
K. shivajii
K. heveanensis
Kwoniella sp. 2
Kwoniella sp. 3
K. fici
Kwoniella sp. 4
K. newhampshirensis
K. shandongensis
92/90
Bullera alba JCM2954
Saitozyma podzolica DSM27192
Tremella mesenterica ATCC28783
STE3
STE20
MF
STE12
SXI1
SXI2
BSP3
MYO2
RPL39
NDC80
C2prot
ATG7
PRT1
BSP2
LPD1
CID1
ZNF1
RPO41
GEF1
DBP10
REI1
ETF1
RUM1
BSP1
RPL22
CAP1
SPO14
IKS1
STE11
NCP1
NCP2
TSR1
PAN6
RSA4
VPS26B
NOG2
UBP6
RPN6
RRM
SWI6
MAF1
Zn-C6-TF
RPB4
NFS1
SES1
SIT4
KRR1
PRP4
TAP42
YAH1
CHS5
Genome assembly
this study
previous studies
pathogen
saprobe
Breeding system
heterothallic
likely heterothallic
homothallic
unclear
MAT loci organization
tetrapolar (unlinked, on different chrs.)
pseudobipolar (unlinked, on the same chr.)
bipolar (fused, on the same chr.)
loss of HD genes
STE3 allele
a1/α
a2/a
a2(+a1)
Genes within MAT loci
HD locus-associated
P/R locus-associated
present
pseudogene
absent
unclear
Gene essentiality
essential
nonessential
unknown
Frequency
0.00
0.25
0.50
0.75
1.00
Cryptocccus sp. 3
CWM60451
P/R HD
*chr_11
200 kb
centromere
STE3
SXI1/SXI2
P/R locus-associated genes
HD locus-associated genes
K. fici
DSM109064
chr_1
K. europaea
PYCC6329
8.95 Mb
1 Mb

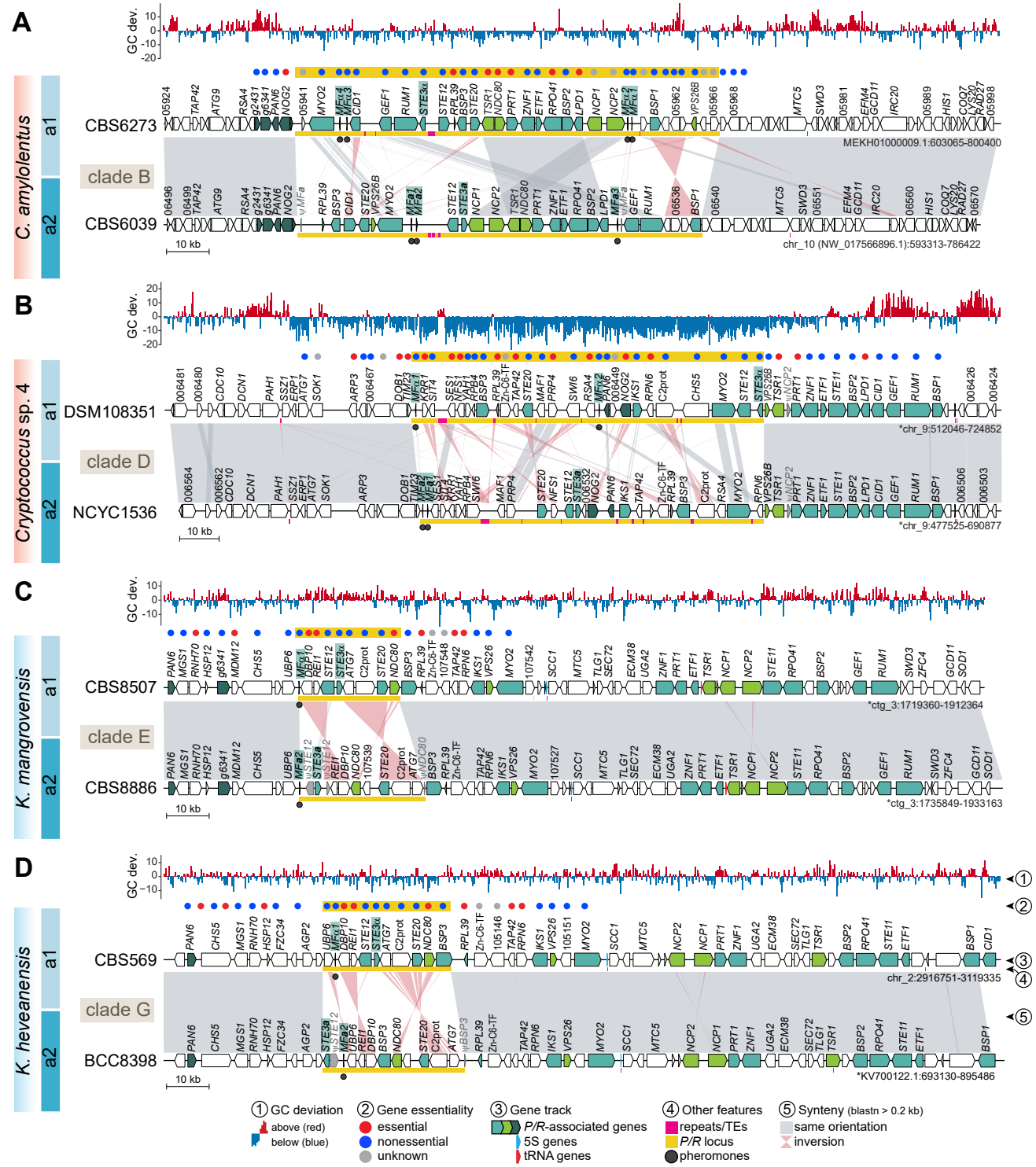
A
C. amylolentus
a1
a2
clade B
CBS6273
CBS6039
MEKH01000009.1:603065-800400
chr_10 (NW_017566896.1):593313-786422
10 kb
B
Cryptococcus sp. 4
DSM108351
NCYC1536
clade D
*chr_9:512046-724852
*chr_9:477525-690877
C
K. mangrovensis
CBS8507
CBS8886
clade E
*ctg_3:1719360-1912364
*ctg_3:1735849-1933163
D
K. heveanensis
CBS569
BCC8398
clade G
chr_2:2916751-3119335
*KV700122.1:693130-895486
GC dev.
① GC deviation
above (red)
below (blue)
② Gene essentiality
essential
nonessential
unknown
③ Gene track
P/R-associated genes
5S genes
tRNA genes
④ Other features
repeats/TEs
P/R locus
pheromones
⑤ Synteny (blastn > 0.2 kb)
same orientation
inversion

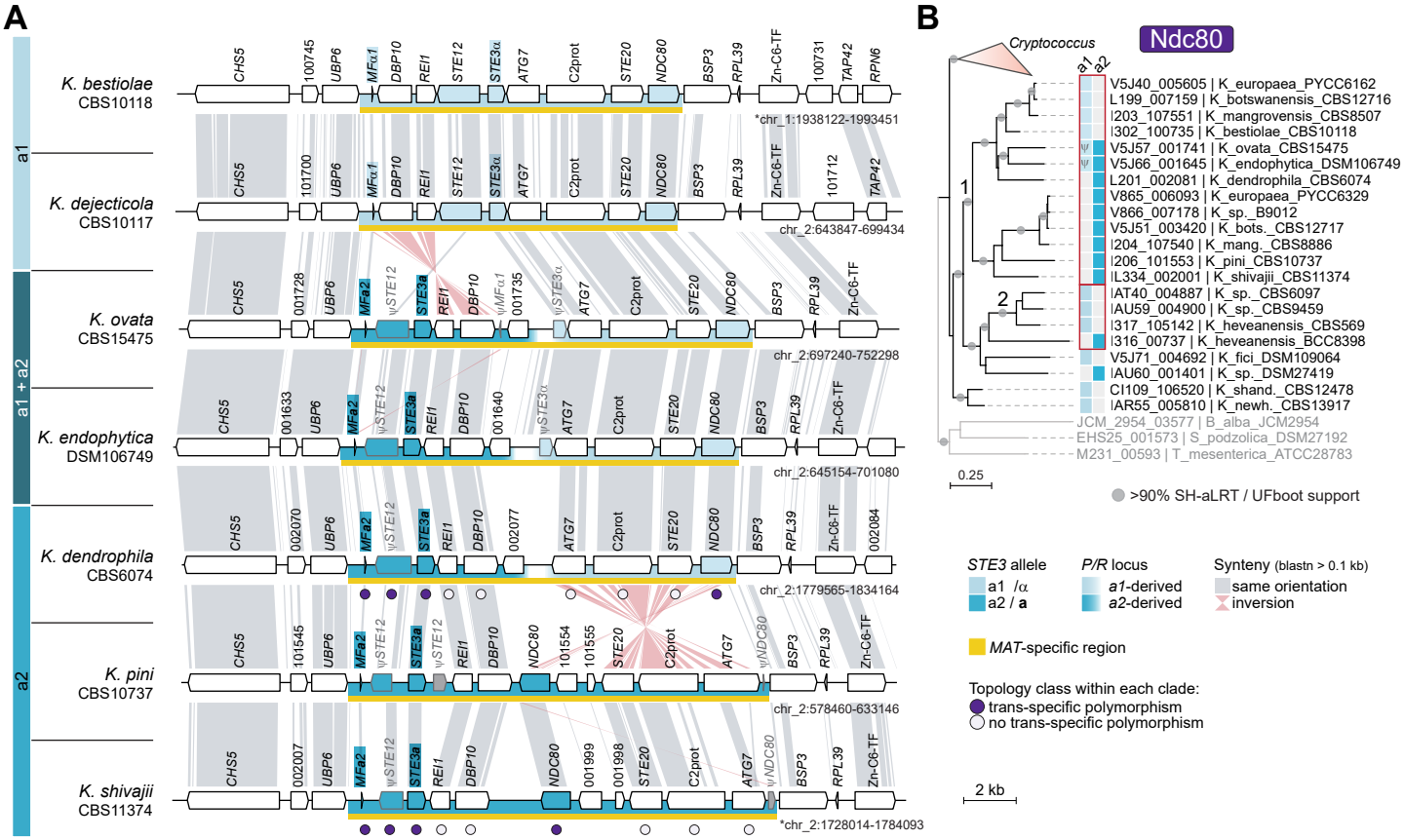
A
B
Ndc80
Cryptococcus
a1
a1 + a2
a2
K. bestiolae
CBS10118
K. dejecticola
CBS10117
K. ovata
CBS15475
K. endophytica
DSM106749
K. dendrophila
CBS6074
K. pini
CBS10737
K. shivajii
CBS11374
*chr_1:1938122-1993451
chr_2:643847-699434
chr_2:697240-752298
chr_2:645154-701080
chr_2:1779565-1834164
chr_2:578460-633146
*chr_2:1728014-1784093
V5J40_005605 | K_europaea_PYCC6162
L199_007159 | K_botswanensis_CBS12716
I203_107551 | K_mangrovensis_CBS8507
I302_100735 | K_bestiolae_CBS10118
V5J57_001741 | K_ovata_CBS15475
V5J66_001645 | K_endophytica_DSM106749
L201_002081 | K_dendrophila_CBS6074
V865_006093 | K_europaea_PYCC6329
V866_007178 | K_sp._B9012
V5J51_003420 | K_bots._CBS12717
I204_107540 | K_mang._CBS8886
I206_101553 | K_pini_CBS10737
L334_002001 | K_shivajii_CBS11374
IAT40_004887 | K_sp._CBS6097
IAU59_004900 | K_sp._CBS9459
I317_105142 | K_heveanensis_CBS569
I316_00737 | K_heveanensis_BCC8398
V5J71_004692 | K_fici_DSM109064
IAU60_001401 | K_sp._DSM27419
CI109_106520 | K_shand._CBS12478
IAR55_005810 | K_newh._CBS13917
JCM_2954_03577 | B_alba_JCM2954
EHS25_001573 | S_podzolica_DSM27192
M231_00593 | T_mesenterica_ATCC28783
0.25
>90% SH-aLRT / UFboot support
STE3 allele
a1 /α
a2 / a
P/R locus
a1-derived
a2-derived
Synteny (blastn > 0.1 kb)
same orientation
inversion
MAT-specific region
Topology class within each clade:
trans-specific polymorphism
no trans-specific polymorphism
2 kb

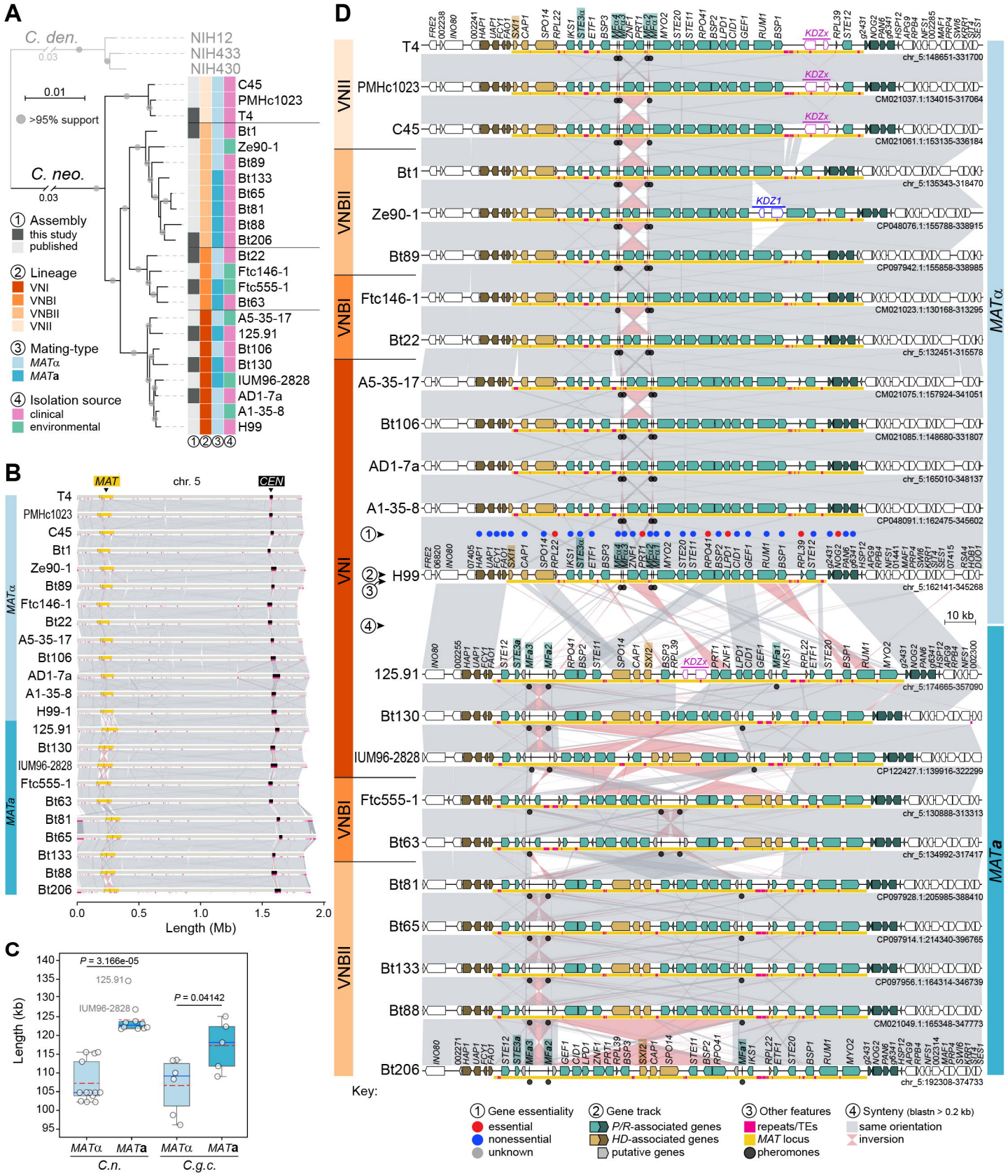
A
C. den.
0.03
NIH12
NIH433
NIH430
0.01
>95% support
C. neo.
0.03
C45
PMHc1023
T4
Bt1
Ze90-1
Bt89
Bt133
Bt65
Bt81
Bt88
Bt206
Bt22
Ftc146-1
Ftc555-1
Bt63
A5-35-17
125.91
Bt106
Bt130
IUM96-2828
AD1-7a
A1-35-8
H99
① Assembly
this study
published
② Lineage
VNI
VNBI
VNBII
VNII
③ Mating-type
MATα
MATa
④ Isolation source
clinical
environmental
①②③④
B
MAT
chr. 5
CEN
MATα
MATa
Length (Mb)
C
P = 3.166e-05
125.91
IUM96-2828
P = 0.04142
Length (kb)
MATα
MATa
C.n.
C.g.c.
D
VNII
VNBII
VNBI
VNI
MATα
MATa
KDZx
KDZ1
chr_5:148651-331700
CM021037.1:134015-317064
CM021061.1:153135-336184
chr_5:135343-318470
CP048076.1:155788-338915
CP097942.1:155858-338985
CM021023.1:130168-313295
chr_5:132451-315578
CM021075.1:157924-341051
CM021085.1:148680-331807
chr_5:165010-348137
CP048091.1:162475-345602
chr_5:162141-345268
10 kb
chr_5:174665-357090
CP122427.1:139916-322299
chr_5:130888-313313
chr_5:134992-317417
CP097928.1:205985-388410
CP097914.1:214340-396765
CP097956.1:164314-346739
CM021049.1:165348-347773
chr_5:192308-374733
Key:
① Gene essentiality
essential
nonessential
unknown
② Gene track
P/R-associated genes
HD-associated genes
putative genes
③ Other features
repeats/TEs
MAT locus
pheromones
④ Synteny (blastn > 0.2 kb)
same orientation
inversion

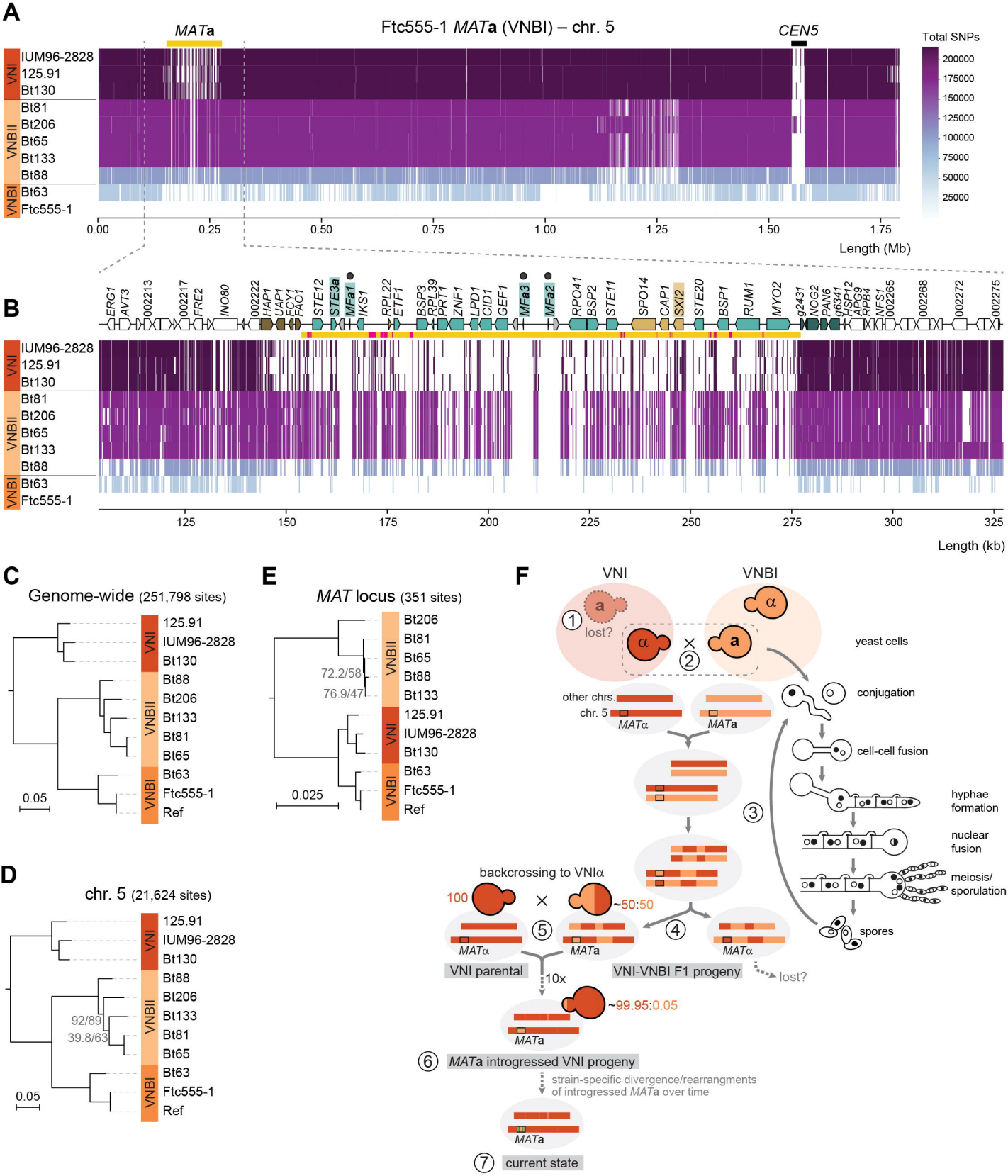
A
Ftc555-1 MATa (VNBI) – chr. 5
MATa
CEN5
Total SNPs
200000
175000
150000
125000
100000
75000
50000
25000
VNI
IUM96-2828
125.91
Bt130
VNBII
Bt81
Bt206
Bt65
Bt133
Bt88
VNBI
Bt63
Ftc555-1
0.00
0.25
0.50
0.75
1.00
1.25
1.50
1.75
Length (Mb)
B
ERG1 AVT3 002213 002217 FRE2 INO80 002222 HAP1 UAP1 FCY1 FAO1 STE12 STE3a MFa1 IKS1 RPL22 ETF1 BSP3 RPL39 PRT1 ZNF1 LPD1 CID1 GEF1 MFa3 MFa2 RPO41 BSP2 STE11 SPO14 CAP1 SXI2 STE20 BSP1 RUM1 MYO2 g2431 NOG2 PAN6 g6341 HSP12 APG9 RPB4 NFS1 002265 002268 002272 002275
125
150
175
200
225
250
275
300
325
Length (kb)
C
Genome-wide (251,798 sites)
125.91
IUM96-2828
Bt130
Bt88
Bt206
Bt133
Bt81
Bt65
Bt63
Ftc555-1
Ref
0.05
D
chr. 5 (21,624 sites)
92/89
39.8/63
0.05
E
MAT locus (351 sites)
72.2/58
76.9/47
0.025
F
VNI
VNBI
lost?
yeast cells
other chrs.
chr. 5
MATα
MATa
conjugation
cell-cell fusion
hyphae formation
nuclear fusion
meiosis/ sporulation
spores
backcrossing to VNIα
100
~50:50
VNI parental
VNI-VNBI F1 progeny
10x
~99.95:0.05
MATa introgressed VNI progeny
strain-specific divergence/rearrangments of introgressed MATa over time
current state

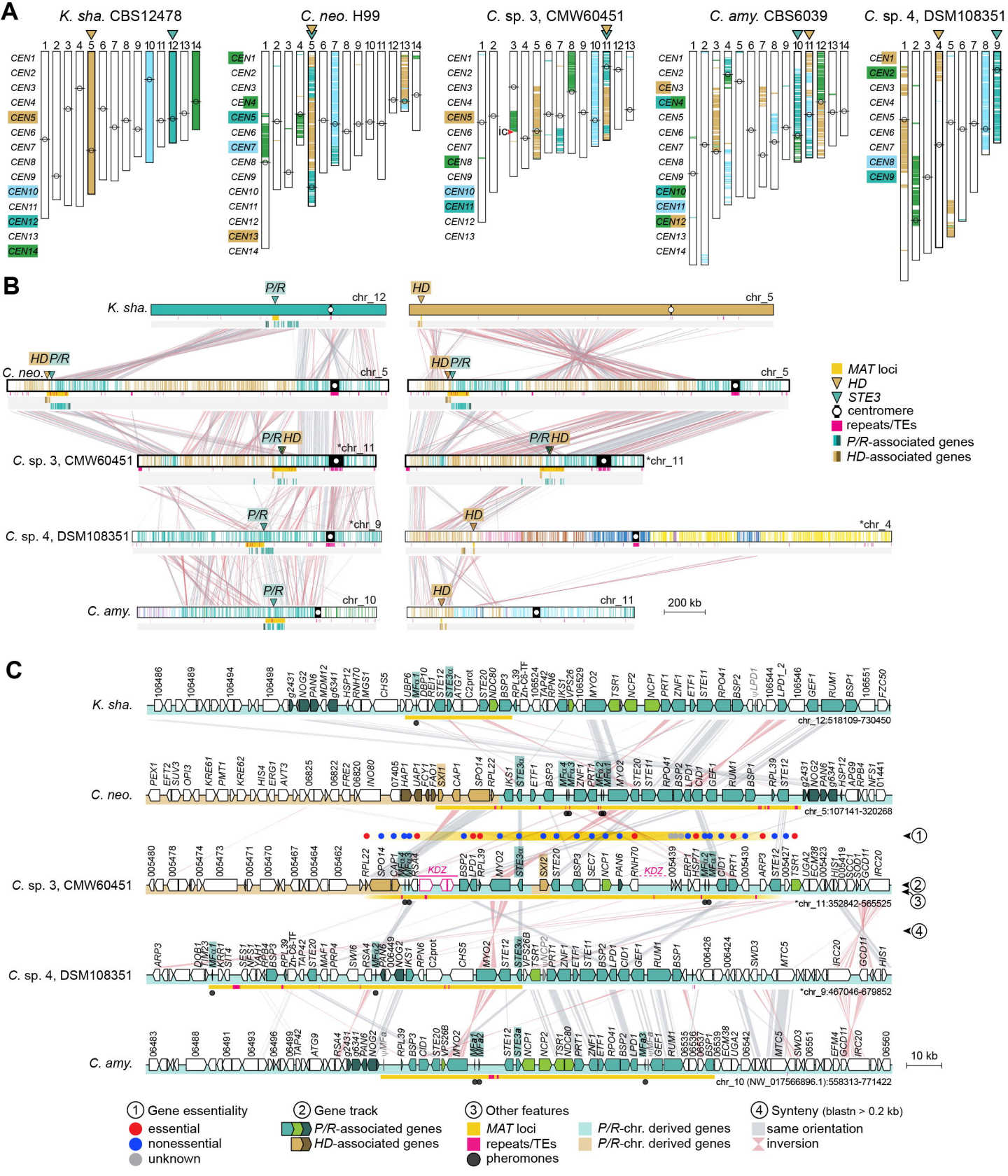
A
K. sha. CBS12478
C. neo. H99
C. sp. 3, CMW60451
C. amy. CBS6039
C. sp. 4, DSM108351
B
K. sha.
C. neo.
C. sp. 3, CMW60451
C. sp. 4, DSM108351
C. amy.
chr_12
chr_5
chr_11
chr_9
chr_10
P/R
HD
200 kb
MAT loci
HD
STE3
centromere
repeats/TEs
P/R-associated genes
HD-associated genes
C
K. sha.
chr_12:518109-730450
C. neo.
chr_5:107141-320268
C. sp. 3, CMW60451
*chr_11:352842-565525
C. sp. 4, DSM108351
*chr_9:467046-679852
C. amy.
chr_10 (NW_017566896.1):558313-771422
10 kb
① Gene essentiality
essential
nonessential
unknown
② Gene track
P/R-associated genes
HD-associated genes
③ Other features
MAT loci
repeats/TEs
pheromones
P/R-chr. derived genes
P/R-chr. derived genes
④ Synteny (blastn > 0.2 kb)
same orientation
inversion

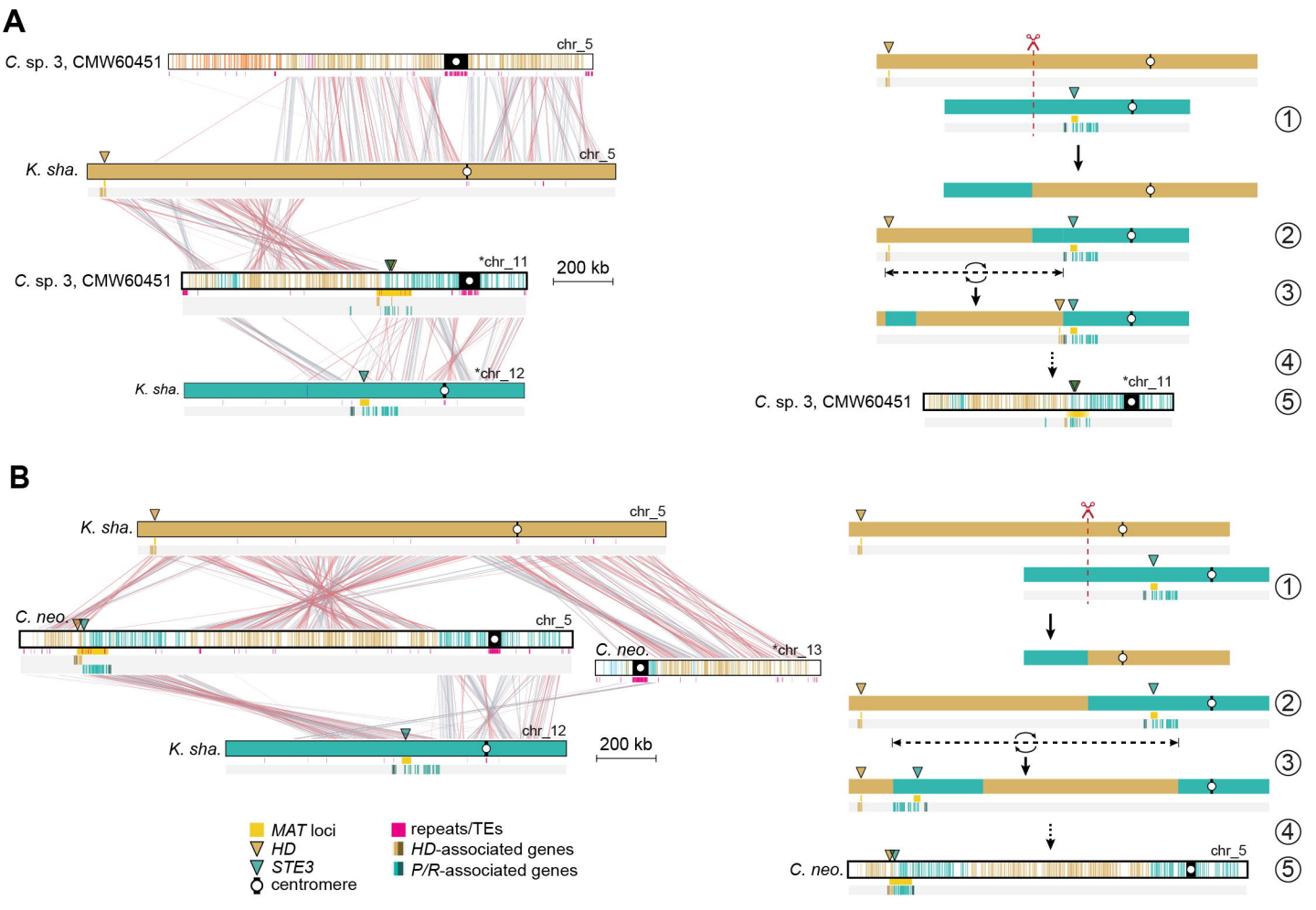
A
C. sp. 3, CMW60451
chr_5
K. sha.
chr_5
C. sp. 3, CMW60451
*chr_11
200 kb
K. sha.
*chr_12
C. sp. 3, CMW60451
*chr_11
①
②
③
④
⑤
B
K. sha.
chr_5
C. neo.
chr_5
C. neo.
*chr_13
K. sha.
chr_12
200 kb
C. neo.
chr_5
①
②
③
④
⑤
MAT loci
HD
STE3
centromere
repeats/TEs
HD-associated genes
P/R-associated genes

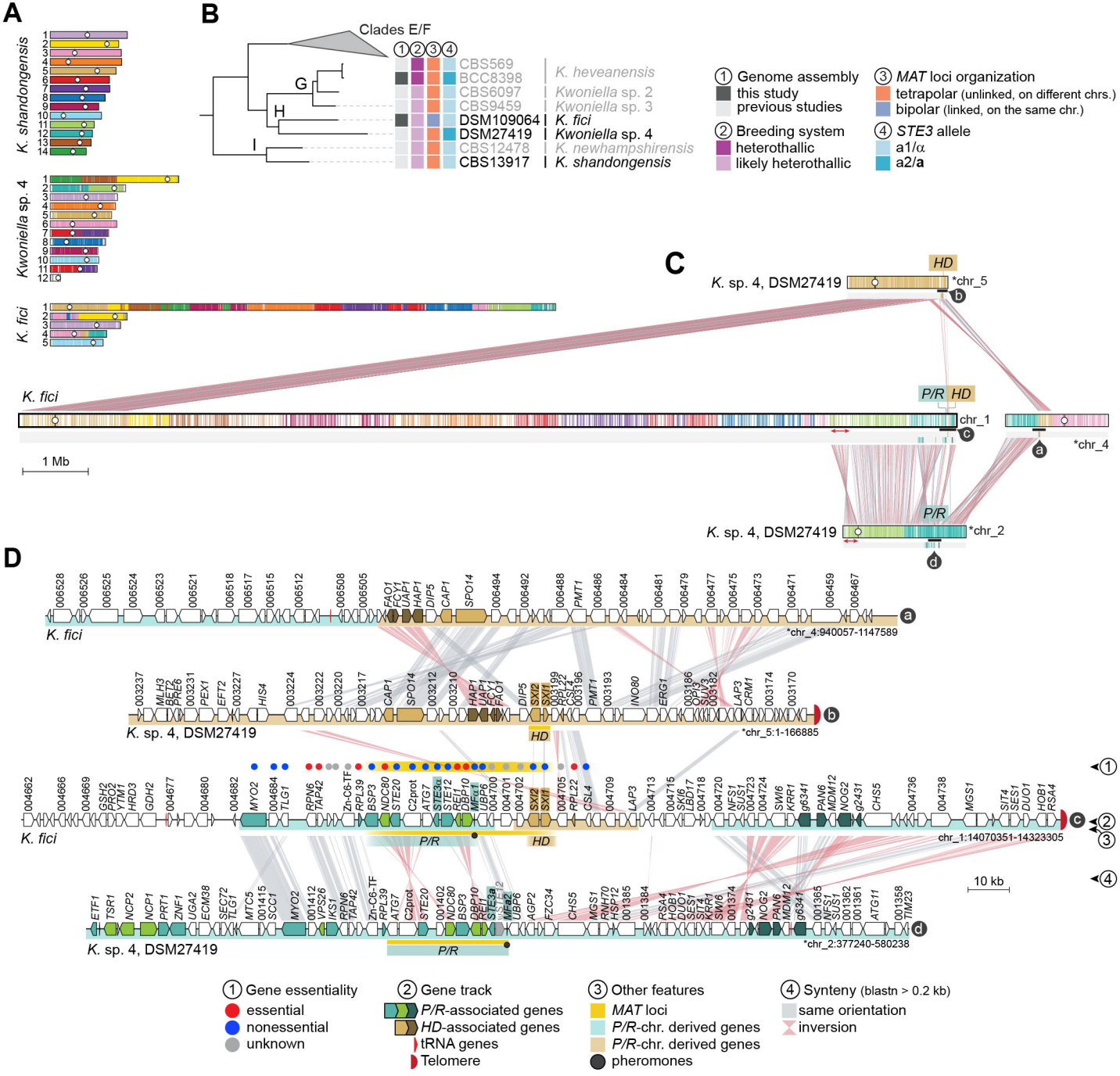
A
K. shandongensis
Kwoniella sp. 4
K. fici
B
Clades E/F
G
H
I
CBS569
BCC8398
CBS6097
CBS9459
DSM109064
DSM27419
CBS12478
CBS13917
K. heveanensis
Kwoniella sp. 2
Kwoniella sp. 3
K. fici
Kwoniella sp. 4
K. newhampshirensis
K. shandongensis
① Genome assembly
this study
previous studies
② Breeding system
heterothallic
likely heterothallic
③ MAT loci organization
tetrapolar (unlinked, on different chrs.)
bipolar (linked, on the same chr.)
④ STE3 allele
a1/α
a2/a
C
K. sp. 4, DSM27419
HD
*chr_5
K. fici
P/R
HD
chr_1
*chr_4
1 Mb
P/R
*chr_2
D
K. fici
*chr_4:940057-1147589
K. sp. 4, DSM27419
HD
*chr_5:1-166885
K. fici
P/R
HD
chr_1:14070351-14323305
10 kb
K. sp. 4, DSM27419
P/R
*chr_2:377240-580238
① Gene essentiality
essential
nonessential
unknown
② Gene track
P/R-associated genes
HD-associated genes
tRNA genes
Telomere
③ Other features
MAT loci
P/R-chr. derived genes
P/R-chr. derived genes
pheromones
④ Synteny (blastn > 0.2 kb)
same orientation
inversion

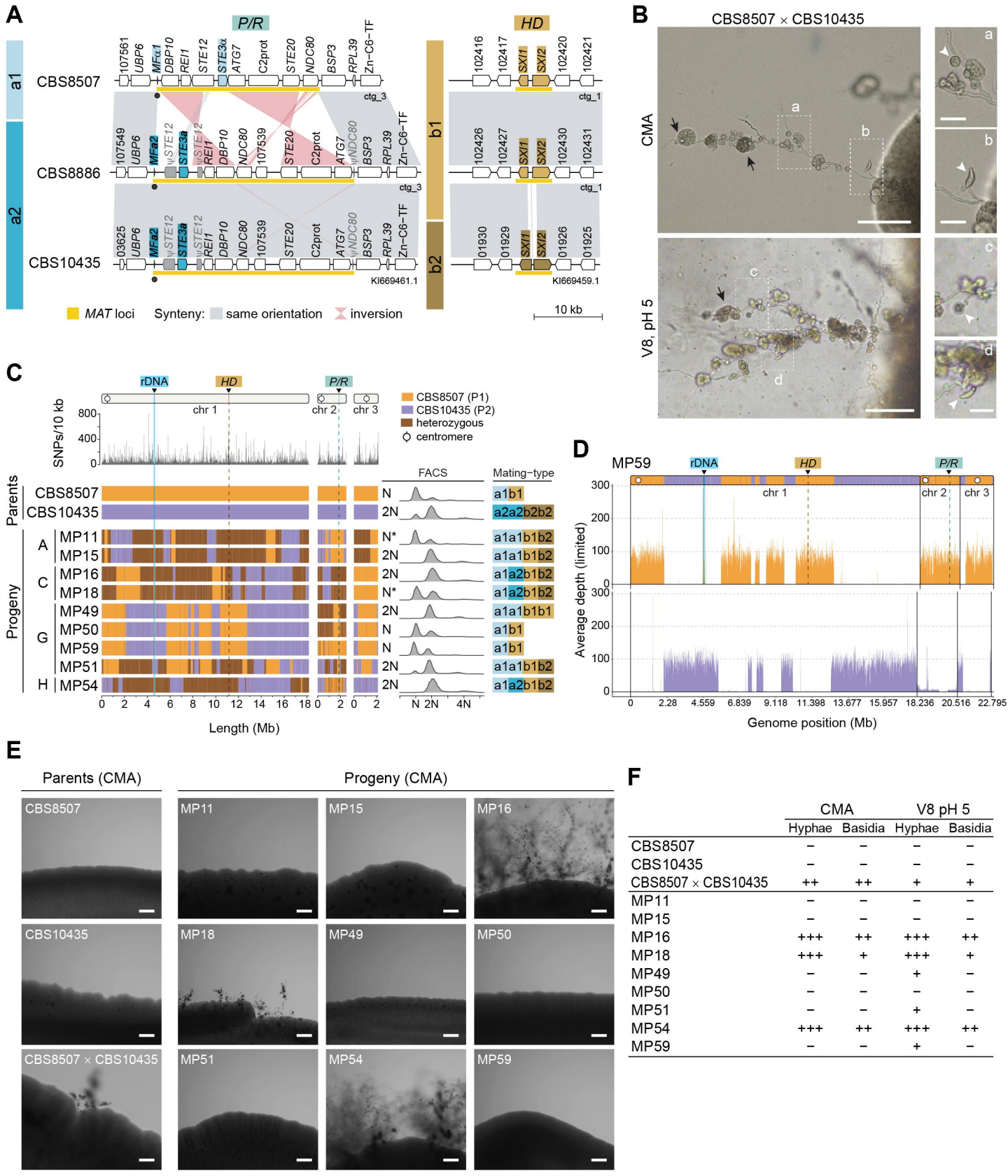

	CMA		V8 pH 5	
	Hyphae	Basidia	Hyphae	Basidia
CBS8507	–	–	–	–
CBS10435	–	–	–	–
CBS8507 × CBS10435	++	++	+	+
MP11	–	–	–	–
MP15	–	–	–	–
MP16	+++	++	+++	++
MP18	+++	+	+++	+
MP49	–	–	+	–
MP50	–	–	–	–
MP51	–	–	+	–
MP54	+++	++	+++	++
MP59	–	–	+	–

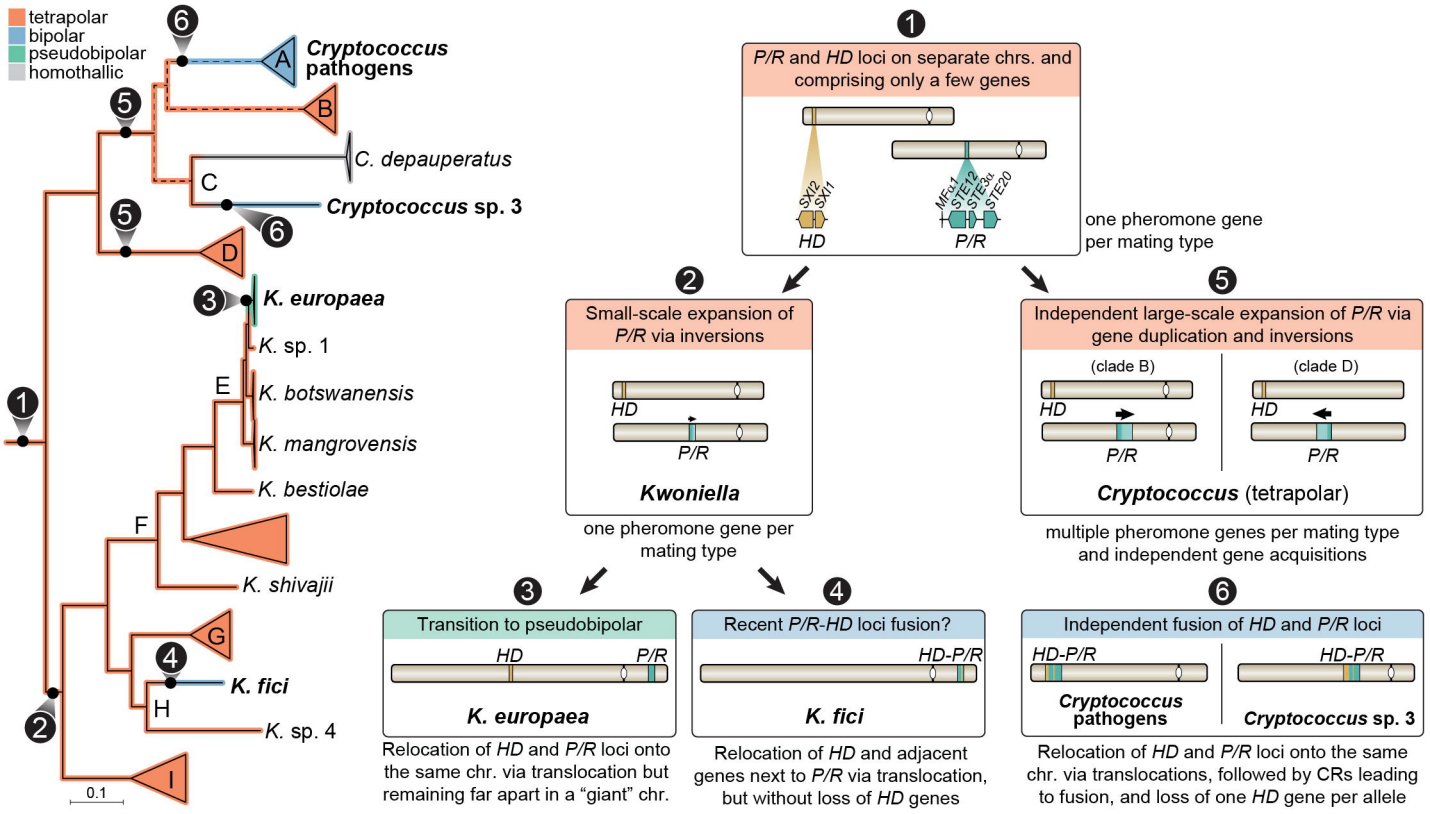
tetrapolar
bipolar
pseudobipolar
homothallic
Cryptococcus pathogens
C. depauperatus
Cryptococcus sp. 3
K. europaea
K. sp. 1
K. botswanensis
K. mangrovensis
K. bestiolae
K. shivajii
K. fici
K. sp. 4
0.1
1 P/R and HD loci on separate chrs. and comprising only a few genes
SXI2
SXI1
HD
MFα1
STE12
STE3α
STE20
P/R
one pheromone gene per mating type
2 Small-scale expansion of P/R via inversions
Kwoniella
one pheromone gene per mating type
5 Independent large-scale expansion of P/R via gene duplication and inversions
(clade B)
(clade D)
Cryptococcus (tetrapolar)
multiple pheromone genes per mating type and independent gene acquisitions
3 Transition to pseudobipolar
K. europaea
Relocation of HD and P/R loci onto the same chr. via translocation but remaining far apart in a "giant" chr.
4 Recent P/R-HD loci fusion?
HD-P/R
K. fici
Relocation of HD and adjacent genes next to P/R via translocation, but without loss of HD genes
6 Independent fusion of HD and P/R loci
Cryptococcus pathogens
Cryptococcus sp. 3
Relocation of HD and P/R loci onto the same chr. via translocations, followed by CRs leading to fusion, and loss of one HD gene per allele